Spring 2007

Synthesis and analysis of reactive nanocomposites prepared by arrested reactive milling

Swati M. Umbrajkar
New Jersey Institute of Technology

ABSTRACT

SYNTHESIS AND ANALYSIS OF REACTIVE NANOCOMPOSITES PREPARED BY ARRESTED REACTIVE MILLING

by
Swati M. Umbrajkar

Different types of reactive nanocomposites have been synthesized by Arrested Reactive Milling (ARM). The technical approach was to increase the interface area available for heterogeneous reaction between solid fuel and oxidizer components. Using aluminum as the main fuel and different metal oxides as oxidizers, highly energetic reactive nanocomposites with different degrees of structural refinement were synthesized. Specifically, stoichiometric Al-MoO_3, Al-CuO, and Al-$NaNO_3$ material systems were studied in detail.

The correlation of heterogeneous exothermic reactions occurring in the nanocomposite powders upon their heating at low rates and ignition events observed for the same powders heated rapidly was of interest. Differential scanning calorimetry (DSC), X-ray diffraction (XRD) and heated filament ignition experiments were used to quantify the ignition kinetics and related reaction mechanisms. Fuel rich Al-MoO_3 nanocomposites were also synthesized using ARM. Optimum composition and milling parameters were identified for fuel-rich compositions. Analysis of exothermic reactions in Al-MoO_3 system showed that kinetics of such reactions could not be determined by isoconversion processing and respective activation energies could not be meaningfully found as functions of reaction progress. Instead, detailed DSC measurements at different heating rates are required to enable one in developing a multi-step kinetic model to describe such reactions adequately.

SYNTHESIS AND ANALYSIS OF REACTIVE NANOCOMPOSITES PREPARED BY ARRESTED REACTIVE MILLING

by
Swati M. Umbrajkar

A Dissertation
Submitted to the Faculty of
New Jersey Institute of Technology
in Partial Fulfillment of the Requirements for the Degree of
Doctor of Philosophy in Mechanical Engineering

Department of Mechanical Engineering

May 2007

APPROVAL PAGE

SYNTHESIS AND ANALYSIS OF REACTIVE NANOCOMPOSITES PREPARED BY ARRESTED REACTIVE MILLING

Swati M. Umbrajkar

Dr. Edward L. Dreizin, Dissertation Advisor — Date
Professor of Chemical Engineering, NJIT

Dr. Mirko Schoenitz, Committee Member — Date
Assistant Research Professor of Mechanical Engineering, NJIT

Dr. Rao Surapaneni, Committee Member — Date
Chief, Explosives Research & Technology Branch,
Energetics & Warheads Division,
U.S. Army Armaments Research, Development & Engineering Center,
Picatinny, NJ

Dr. Boris Khusid, Committee Member — Date
Professor of Chemical Engineering, NJIT

Dr. Kwabena Narh, Committee Member — Date
Associate Professor of Mechanical Engineering, NJIT

BIOGRAPHICAL SKETCH

Author: Swati M. Umbrajkar

Degree: Doctor of Philosophy

Date: May 2007

Undergraduate and Graduate Education:

- Doctor of Philosophy in Mechanical Engineering,
  New Jersey Institute of Technology, Newark, NJ, 2007

- Master of Science in Mechanical Engineering,
  Wayne State University, Detroit, MI, 2002

- Bachelor of Science in Production Engineering,
  Walchand Institute of Technology, Solapur, India, 1997

Major: Mechanical Engineering

Presentations and Publications:

Swati Umbrajkar, Mirko Schoenitz and Edward L. Dreizin,
"Heterogeneous Processes Leading to Metal Ignition in Reactive Nanocomposite Materials,"
45th AIAA Aerospace Sciences Meeting and Exhibit, Reno, NV, Jan 8-11, 2007.

Swati Umbrajkar, Mirko Schoenitz and Edward L. Dreizin,
"Fuel-rich Thermite Based Nanocomposites Prepared by Arreseted Reactive Milling,"
45th AIAA Aerospace Sciences Meeting and Exhibit, Reno, NV, Jan 8-11, 2007.

Swati Umbrajkar, Mirko Schoenitz and Edward L. Dreizin,
"Kinetic Analysis of Thermite Reactions in Nanocomposites Prepared by Arrested Reactive Milling,"
YPSE AIAA-Baltimore section, Nov 10-11, 2006.

Mirko Schoenitz, Swati M. Umbrajkar and Edward L. Dreizin,
"Kinetic Analysis of Thermite Reactions in Al-MoO_3,"
42nd AIAA/ASME/SAE/ASEE Joint Propulsion Conference, Sacramento, CA July 10-12 2006.

Swati Umbrajkar, Mirko Schoenitz and Edward L. Dreizin,
"Control of Structural Refinement of the Al-MoO_3 Nanocomposites Produced by Arrested Reactive Milling,"
Proc. Ann. Meeting of Materials Research Society, Boston, MA Nov-Dec 05, Vol 0896- H02-04.

Mikhaylo Trunov, Swati Umbrajkar, Mirko Schoenitz, Joseph Mang and Edward L. Dreizin,
"Study of Melting and Oxidation of Nano-Aluminum Powders,"
Proc. Ann. Meeting of Materials Research Society, Boston, MA Nov-Dec 05, Vol 0896-H04-06.

Edward L. Dreizin, Mirko Schoenitz, Yuriy .L. Shoshin, Mikhaylo.A. Trunov, Swati Umbrajkar, Trent. S. Ward, Xiaoying Zhu
"Highly-Energetic Nanocomposite Powders Produced by Arrested Reactive Milling,"
36th International Annual Conference of ICT & 32nd International Pyrotechnics Seminar June 2005.

Swati Umbrajkar, Xiaoying Zhu, Mirko Schoenitz, and Edward Dreizin,
"Effect of Compositional and Structural Refinement on the Ignition and Combustion of Reactive Nanocomposite Powders,"
4th Joint meeting of the U.S sections of the Combustion Institute, Philadelphia March 23-25, 2005.

Swati M. Umbrajkar, Mirko Schoenitz and Edward L Dreizin,
"Synthesis and Characterization of Sodium-Nitrate based Reactive Composites produced by Arrested Reactive Milling,"
Propellants. Explos. Pyrotech, 32 (1), pp. 32-41, 2007.

Swati M. Umbrajkar, Mirko Schoenitz and Edward L. Dreizin,
"Exothermic reactions in Al-CuO nanocomposites,"
Thermochim Acta 451, pp. 34-43, 2006.

Swati M. Umbrajkar, Mirko Schoenitz and Edward L Dreizin,,
"Control of structural refinement and composition in Al-MoO_3 nanocomposites prepared by arrested reactive milling,"
Propellants. Explos. Pyrotech, 13 (5), pp. 382-389, 2006.

Mikhaylo A. Trunov, Swati M. Umbrajkar, Mirko Schoenitz, Joseph T.Mang and Edward L. Dreizin,

"Oxidation and melting of aluminum nanopowders,"
J. Phys. Chem. B, 110 (26), pp. 13094 -13099, 2006.

Swati M. Umbrajkar, Mirko Schoenitz, Steven R. Jones and Edward L. Dreizin,

"Effect of temperature on synthesis and properties of aluminum–magnesium mechanical alloys,"
J of Alloys and compounds 402, p. 70–77, 2005.

Swati M. Umbrajkar, Mirko Schoenitz and Edward L Dreizin,

"Kinetic analysis of thermite reactions in Al-MoO_3 nanocomposite,"
J. Prop Power, in Press 2007.

Swati M. Umbrajkar, Mirko Schoenitz and Edward L Dreizin,

"Kinetics of solid state reduction-oxidation reactions: Failure of isoconversion approach,"
Thermochim Acta, submitted 2007.

Swati M. Umbrajkar, Mirko Schoenitz and Edward L Dreizin,

"Aluminum rich Al-MoO_3 nanocomposite powders prepared by arrested reactive milling,"
J. Prop Power, in Press 2007.

To the memory of my loving **grandparents**

To my **mother**
for her countless sacrifices, the immense love she always surrounds me with ,
her continued support, her blessings.....

To my **father**
for the discipline, values and principles he imbibed in me,

and

To my beloved **husband** and **son** for their encouragement, love and belief in me

ACKNOWLEDGMENT

First of all I would like to express my deepest appreciation to Dr. Edward Dreizin, for not only being my research advisor, but also for his support, patience and encouragement throughout this process. I am grateful to him for the various learning opportunities I received as part of my research activities in the laboratory. I firmly believe that I could not have found a better advisor. Special thanks are given to Dr. Boris Khusid, Dr. Kwabena Narh and Dr. Rao Surapaneni for actively participating in my committee.

I would like to extend my heartfelt gratitude to Dr. Mirko Schoenitz, for guiding me with technical details at every nano-step of the way; towards the completion of my work. I owe him special thanks for every tip and trick he has taught me, to solve the various problems I faced during my work. His insight, which immensely contributed to the planning and execution of various experiments, deserves special recognition as well.

My fellow graduate and undergraduate students (Alexandre, Xiaoying, Salil Ervin, Demitrios and Soumitri,) in the Energetic Materials Laboratory are deserving of recognition for their support. I also wish to thank Dr. Mikhaylo Trunov and Mr Vern Hoffmann for their technical guidance and assistance over the years.

I would also like to thank my brother for being there for me, whenever I needed him the most. I wish to thank my uncles and aunts for their support and faith in me, ever since my childhood. Finally I would like to thank my in-laws for their encouragement and love.

TABLE OF CONTENTS

TABLE OF CONTENTS
(Continued)

TABLE OF CONTENTS
(Continued)

TABLE OF CONTENTS
(Continued)

Chapter **Page**

LIST OF FIGURES

Figure **LIST OF FIGURES (Continued)** **Page**

Figure **LIST OF FIGURES (Continued)** **Page**

Figure	LIST OF FIGURES (Continued)	Page
5.3	Backscattered electron SEM image of Al-MoO_3 nanocomposites with varying concentration of Al.....	89
5.4	XRD patterns of samples with varying concentrations of Al.....	91
5.5	Mass ratio of Mo/MoO_3 phases calculated using experimental XRD traces and whole pattern refinement software.....	92
5.6	Baseline corrected DSC traces of nanocomposite powders recorded a 2 K/min.....	94
5.7	Ignition temperatures of the nanocomposites at different heating rates.....	96
5.8	Calculated adiabatic flame temperatures for the N_2/O_2 gas mixtures with a fixed O_2 concentration of 22.5 % with Al and xAl+MoO_3 fuels.....	98
5.9	Pressure traces of the Al and Al-MoO_3 nanocomposites with varying Al concentration recorded during CVE.....	99
5.10	Equivalent heat of reaction normalized per mass of aluminum for different powder compositions.....	101
5.11	The maximum rates of pressure rise measured in CVE experiments, dp/dt_{max}, as a function of the powder composition.....	102
5.12	XRD patterns of CVE combustion products of different nanocomposite powders.....	103
5.13	Results of XRD analysis of combustion products collected in CVE experiments: intensity ratios for peaks of Al_2O_3 and Al.....	104
6.1	Backscattered electron image of the cross-section of an Al-MoO_3 nanocomposite.....	109
6.2	Baseline-corrected DSC traces collected for nanocomposite powder with bulk composition 4 Al + MoO_3 at heating rates ranging from 1 to 40 K/min.....	110
6.3	Data processed according to the Kissinger peak position method. Heating rates used were 1, 2, 5, 10, 20, and 40 K/min.....	112

Figure	LIST OF FIGURES (Continued)	Page

LIST OF TABLES

CHAPTER 1

INTRODUCTION

1.1 Problem Statement

Nanostructured materials are receiving significant attention in the fields ranging from electronics to metallurgy due to their novel and unique properties. Similarly, reactive nanocomposite powders exploiting the exothermic nature of thermite reactions [1-3] have attracted a great deal of interest for their use in ordnance applications. Different types of reactive nanocomposites have been synthesized, including mixed nanopowders (also called metastable intermolecular composites, or MIC) [4-9], porous nanocomposites produced by sol-gel synthesis [9-13], self assembled composites [14], multilayer nanofoils [15-17], and dense nanocomposite powders produced by Arrested Reactive Milling (ARM) [18-22]. Despite different synthesis techniques and material types, the common approach was to increase the interface area available for heterogeneous reaction between solid fuel and oxidizer components. Although different nanocomposites have been synthesized, the reaction mechanisms between the starting materials are not well understood. Hence this work focuses on exploring the benefits of nanofabrication and study of the reaction mechanisms of high energy density materials for their use in propellants, explosive and pyrotechnics. Specifically, synthesis, characterization and ignition-combustion performance of highly energetic nanocomposites prepared by ARM are included in this thesis. A quantitative model describing the reaction mechanism for energetic nanocomposites was developed. The proposed reaction model in conjunction with a detailed heat transfer model has been used to establish a relationship between the reaction mechanism and ignition kinetics.

Using aluminum as the main fuel and different metal oxides as oxidizers, highly energetic reactive nanocomposites with different degrees of structural refinement have been synthesized. Specifically Al-MoO_3 and Al-CuO material systems are studied in detail. The correlation of different processes occurring in the nanocomposite powders during heterogeneous exothermic reactions identified in low heating rate experiments and ignition of the same powders occurring at high heating rates was of interest. Differential scanning calorimetry (DSC), X-ray diffraction (XRD) and heated filament ignition experiments were used to quantify the ignition kinetics and related reaction mechanisms.

A brief study on the synthesis and characterization of nitrates based energetic composites is also included in this thesis. Three metallic powders, including aluminum, magnesium, and mechanically alloyed $Al_{0.5}Mg_{0.5}$ were used as fuels to prepare composites with $NaNO_3$ as an oxidizer using ARM.

1.2 Background

Traditional energetic materials such as trinitrotoluene or TNT($C_7H_5N_3O_6$), RDX($C_3H_6N_6O_6$), hexanitrobenzene, also known as HNB($C_6N_6O_{12}$) comprising an oxidizer and fuel in a single molecule are characterized by very high, but poorly controllable reaction rates. Generally, as illustrated in Figure 1.1, each molecule consists of a combination of "fuel" (C-H) and "oxidizer" (N-O) with the main reaction products including H_2O, CO_2 and CO. Therefore; the energy output is limited to the heat of C and H oxidation leading to a relatively low energy density.

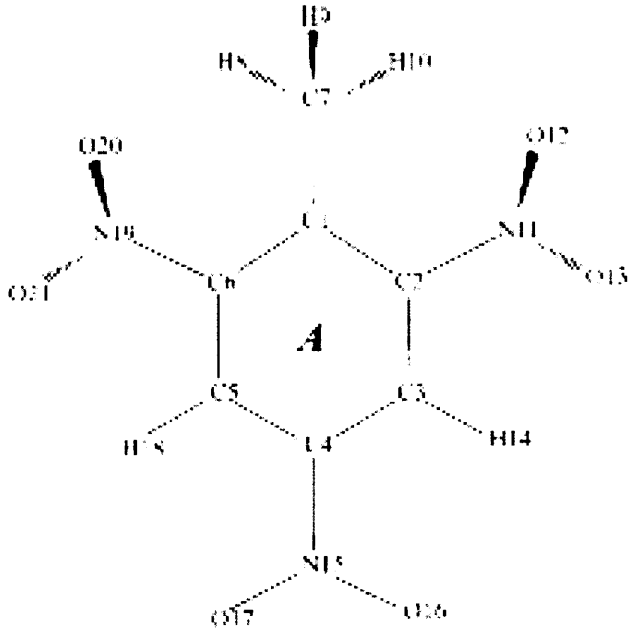

Figure 1.1 Structure of 2, 4, 6 trinitrotoluene (monomolecular energetic material) [23].

An alternative to monomolecular energetic materials is a class of energetic composites based on metal fuels. Such composites are characterized by increased reaction enthalpy, low cost and non-toxic combustion by-products [24-28]. Most popular metal fuels include Al, Mg, Zr and B. However, the primary drawback of metal-based energetic compositions is their relatively low reaction rate. Specifically, ignition for most metals is rate limited by relatively slow heterogeneous processes, which serve as a kinetic bottleneck for the bulk reaction rate.

Recently, this problem was addressed by development of metal-based nanomaterials, including nano-sized and nanostructured powders. The basic approach is to increase the specific surface area available for heterogeneous reaction and thus boost the overall reaction rate. Two types of novel reactive nanomaterials based on metal fuels were recently developed at NJIT. These enhanced metal-based fuels can be categorized into supersaturated solid solutions and composite nanomaterials. Supersaturated solid

solutions of metal based systems like Al-Mg, Al-Ti, Al-Li, Al-Zr, Al-MgH_2, B-Mg, etc have been studied in detail elsewhere [24-28]. Composite nanomaterials can be further categorized into metal-metalloid composites [17, 28-29] and metal-metal oxide composites [1-8, 10-12]. This study focuses on the metal - metal oxide nanocomposites using aluminum as a fuel. These include most popular formulations described in the literature dealing with energetic materials [3-16, 18-22 and 30] e.g, Al-Fe_2O_3, Al-CuO, Al-MoO_3, Al-$KMnO_4$ etc. For all of the above compositions; large negative heat of formation of Al_2O_3 [1-16, 18 - 22] results in highly exothermic thermite reaction.

1.3 Thermite Compositions

Based on the size of the fuel and oxidizer the thermites can be categorized into traditional thermites and nano-thermites. Micron sized reactants are used in traditional thermites [1-3, 31] whereas use of nano-sized fuel and oxidizer particles or domains are used to produce nanothermites in recent research [4-16, 18-22]. Traditional thermites are prepared by conventional mixing component powders such as ferric oxide and aluminum [1-3]. In conventional mixing, domains rich in either fuel or oxidizer can exist which limit the mass transport and therefore decrease the efficiency of reaction [10]. Novel mixing techniques have also been developed (discussed in Section 1.3.1). Based on their synthesis techniques, nanothermites can be broken down in two main categories; bottom up and top down techniques. 'Bottom up' techniques use atoms and molecules as nano material building blocks. In the 'top down' approach the nanomaterials are produced as a result of refinement of the initial component present as bulk domains or relatively coarse powders. Figure 1.2 shows a broad classification of nanothermite preparation techniques.

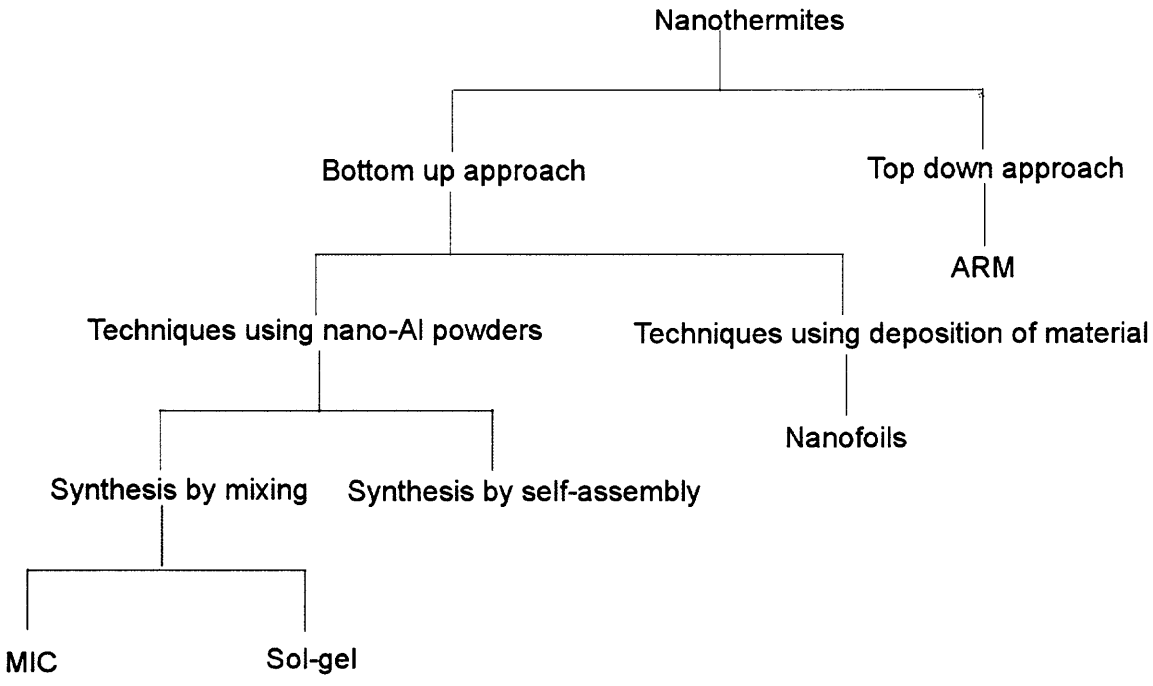

Figure 1.2 Classification of nanothermites based on their synthesis techniques.

1.3.1 Nanothermites Prepared by Bottom up Approach

These thermites involve the use of nanometer sized reactants [4-16, 18-22]. Both the nano-sized aluminum and the nano-sized metal oxides can be synthesized in situ or can be purchased from commercial supplier [8-14, 31-36]. Based on their synthesis techniques, nanothermites prepared by bottom up approach are categorized into:

1.3.1.1 Techniques using nano-Al powders.

A detailed study on the potential usage of energetic nano-sized powders for combustion and rocket propellants lists the suppliers of various nano-sized energetic materials [34]. The availability of nano-sized Al powders is critically important for these techniques. Therefore following are brief descriptions of two of the main nano aluminum particle-synthesis processes.

Generation of nano aluminum powder through wire explosion.

Earlier researchers have worked on synthesis and characterization of nanoaluminum powders via wire explosion [31-32]. A recent work based on the same process indicates that this is basically an inert gas evaporation technique, where the particles are produced by evaporating a thin metal conductor by passing high current through it in an inert atmosphere [33]. The nano aluminum particles were produced in nitrogen, argon and helium environments. A basic circuit used for exploding wires to produces nano powders is shown in Figure 1.3.

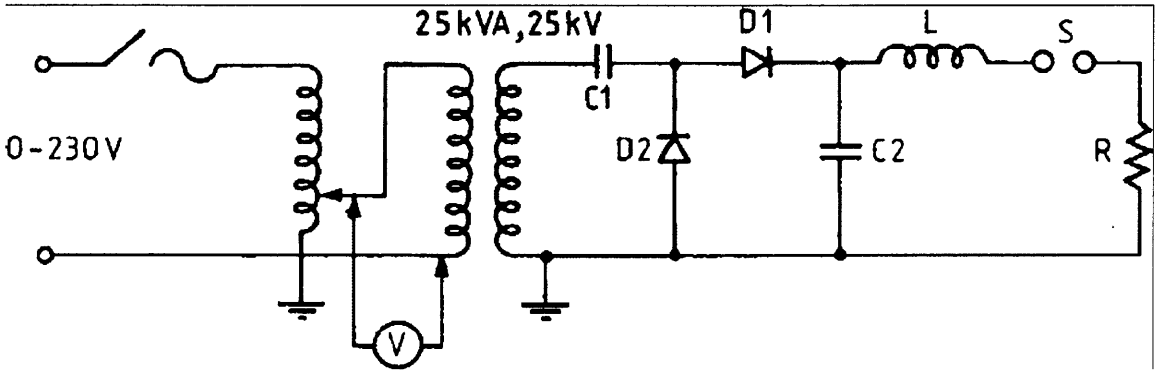

Figure 1.3 Experimental set up for production of nano aluminum particles by wire-explosion technique [33].

The major factor determining the particle size in the wire explosion process is superheating of evaporated material. The particle size produced by the wire explosion reduces substantially with increasing super heating of the metal. The nano particle formation process starts with closing of the switch S, when the voltage appears across the wire and the current rises. This causes Joule heating of the conductor, which eventually melts and boils. The switch is a high voltage trigatron gap, R is the exploding aluminum wire resistance and L is the contribution by the internal inductance of the capacitor and the lead inductance. Due to Joule heating, the temperature of the conductor followed by melting and eventually reaching the boiling point and superheating, before the liquid

phase changes to gas phase. After wire evaporation, the plasma begins to expand in the medium due to the significant difference in the temperature between the plasma and the ambient gas. The expanded plasma particles are gradually cooled during this process of collision with ambient gas molecules. Finally, the plasma loses its expansive driving force. Hence, a lower ambient pressure allows a larger expansion volume. This leads to lower concentration of aluminum during particle growth, resulting in small nano-particles.

Synthesis of aluminum nano particles with femtosecond laser pulses

Aluminum nano particles have been synthesized by irradiation of solid Al targets with femtosecond laser pulses [35]. Figure 1.4 shows schematics of the experimental setup and conditions of this process.

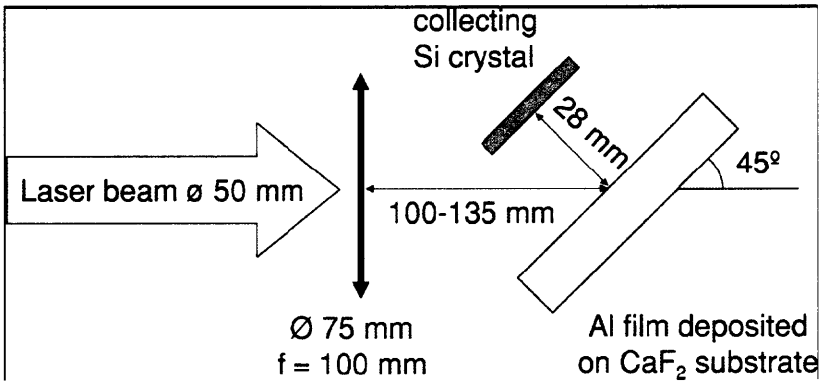

Figure 1.4 Schematics of the experimental setup and conditions [35].

This process involves a Ti:sapphire laser beam, with 50 fs pulse duration, 0.8 μm wavelength and a diameter of few millimeters which irradiates a target. The spatial laser intensity profile is Gaussian to a good approximation. The target is a 100 nm thick Al foil on a transparent heat-insulating Ca-F_2 glass substrate. The pressure in the vacuum chamber is 10^{-4} Torr. The laser irradiates the target at an angle of 45° and intensities varying between $3e^{12}$ W/cm^2 and $5e^{14}$ W/cm^2. The heated plasma expands into the

vacuum from the Al target, whereas the debris are collected on a silicon wafer. In general, both the size and shape of the deposited particles are observed to be widely distributed the former ranging from tens of nanometers to as high as approximately 500 nm. Extensive work has also been conducted on the production of nanoscale aluminum powders known as Ultra Fine Grain (UFG) aluminum. The dynamic gas condensation method was used to produce UFG aluminum as described elsewhere [36]. The average particle size of UFG aluminum was approximately 35 nanometers [36]. Nanothermites synthesized by using nano-Al powders can be further divided into the following categories:

1.3.1.1. a. Nanocomposites Prepared by Mixing (ultrasonication): Metastable Intermolecular Composites or MIC is a class of energetic materials composed of individual fuel and oxidizer particles that have nano-scale dimensions [4–9].

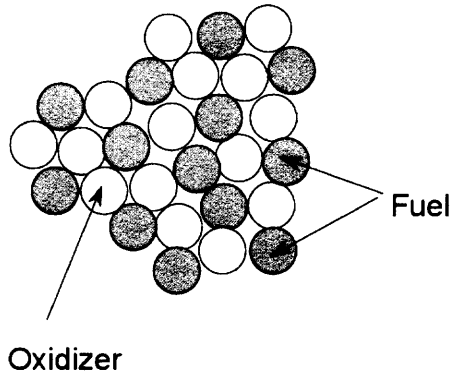

Figure 1.5 Structure of MIC [5].

A typical structure of MIC is shown in Figure 1.5. Arrays of composites have been prepared and studied by several researchers using aluminum and different metaloxides [4-9]. The powder mixture is typically suspended in hexane solution and mechanically mixed using sonic waves. The sonication process helps break up macro-scale

agglomerates and ensure better mixing of fuel and oxidizer. The mixture is poured in a pan and heated to a few degrees above ambient, allowing the solvent to evaporate [4-6].

Advantages: MIC exhibit reduced ignition temperatures and high bulk burn rate as compared to micron sized composites [4-9].

Disadvantages: The mechanical mixing renders a rather unstructured nature to the composites. This causes a large and almost uncontrollable variability in the combustion behavior [9]. MIC's are spark and friction sensitive, hence very small quantities of samples are synthesized and handled [5]. Nano-Al powders used are pyrophoric in air; hence handling of these powders is difficult. In order to passivate the pyrophoric aluminum, a thin aluminum oxide coating surrounds the Al core. However, even a few nanometer thick coating of oxide results in a significant volumetric fraction of inert aluminum oxide [5, 7].

1.3.1.1. b. Nanocomposites Prepared by Sol-Gel Processing: In a sol-gel derived nanocomposite, fuel commonly resides within the pores of a solid matrix made up of the oxidizer particles as shown in Figure 1.6 [10-12]. The preparation of such composites starts with dissolution of molecular precursors of oxidizer which undergo hydrolysis and condensation to form a stable sol (suspension of particles 1-1000 nm in diameter in solution) [9-12]. This process is initiated by changing pH, temperature, or ionic strength of the solution, or through addition of a catalyst or gelling agent. The sol can be further linked through condensation of surface groups on the particle surfaces to form a gel. The gel is a rigid three-dimensional structure that has nanostructured framework and pores with dimensions of 2-100 nm. The final step of removing the pore fluid from the wet gels

is accomplished by either evaporation to produce a xerogel or by supercritical extraction to yield an aerogel [4-5, 9].

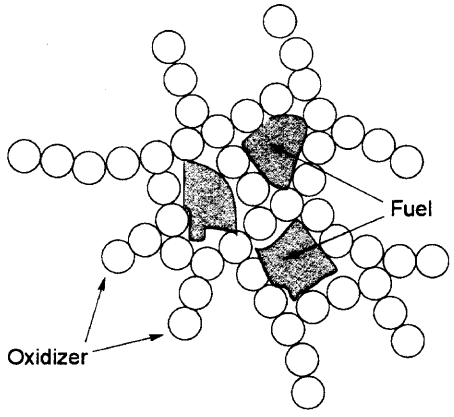

Figure 1.6 Structure of a sol-gel based thermite formulation [9].

Advantages:

Attractive features of the sol-gel approach for energetic material processing are that it produces composites with extremely well dispersed and intimately mixed component phases [4]. Laboratory equipment is inexpensive.

Disadvantages: The sol-gel prepared aerogel and xerogel oxidizers contain impurities that act as heat sinks during flame propagation and retard the combustion wave speed [9]. In order to remove impurities, the oxidizers need to be subjected to heat treatment, which increases the complexity of the process [9]. Compatibility of sol-gel processing with different materials is limited. Use of nano-sized reactants makes handling of these powders difficult. Nano-sized aluminum results in reduced active metal content as in the mixed nanocomposites.

1.3.1.1. c. Self Assembled Nanoenergetic Composite

In this category of composites, researchers have chosen oxidizer nanorods over spherical nanoparticles because of higher surface area available for arrangement of fuel nanoparticles around them [14].

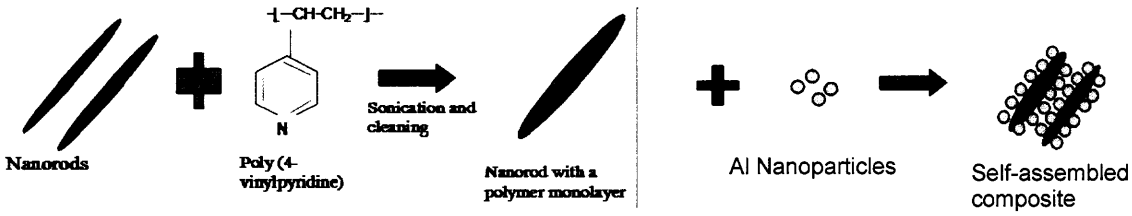

Figure 1.7 Schematic of synthesis and structure of a self-assembled energetic comoposite [14].

Polymer is used as a binder because each polymer molecule generally has numerous binding sites to bind the nanoparticles. A schematic of the synthesis process along with the structure of a self-assembled composite is shown in Figure 1.7. The self-assembly of nanoenergetic composites begins with the synthesis of nanorods. Copper oxide nanorods were synthesized by surfactant templating method. This is followed by sonication of the nanorods in a solution containing the polymer of choice for 4 hrs, followed by separation of the nanorods from the solution by a centrifuge. The nanorods are further washed to remove excess polymer. These nanorods are dried at 120 °C for 1.5 hrs to remove the solution. The polymer-coated nanorods are then mixed with nano-Al particles with 2-propanol as the dispersing medium. The particles are separated by centrifugation and dried to produce self-assembled nanocomposites [14].

Advantages: Oxidizer nanorods provide more surface area available for arrangement of fuels nanoparticles. The burn rate of self-assembled composite has been found to be higher than that of the similar nanocomposites prepared by simple mixing [14].

Disadvantages: Synthesis of nanorods is a lengthy and complicated process. Only small quantities of nanorods and hence self-assembled nanocomposites can be prepared in each batch [14].

1.3.1.2 Techniques using Deposition of Material.

Reactive Multilayer Nanofoils

Instead of combining the reactants in powder compacts, sputter deposited alternate layers of reacting materials were produced to form highly reactive nanofoils [15-17]. Self propagating exothermic formation reaction in nanofoils makes them an ideal candidate for various joining applications. Such materials are also well suited for applications requiring high density energetic components. Highly structured nanofoils are prepared in argon environment by deposition of reactants onto a substrate (silicon wafer) by rotating them above metal (Al) and oxidizer (CuO) targets respectively [15-16].

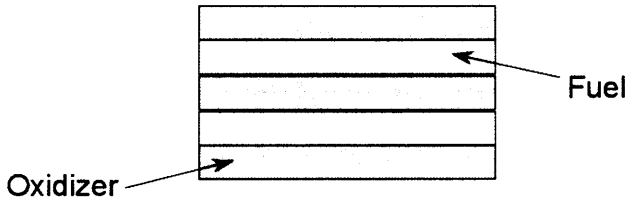

(a)

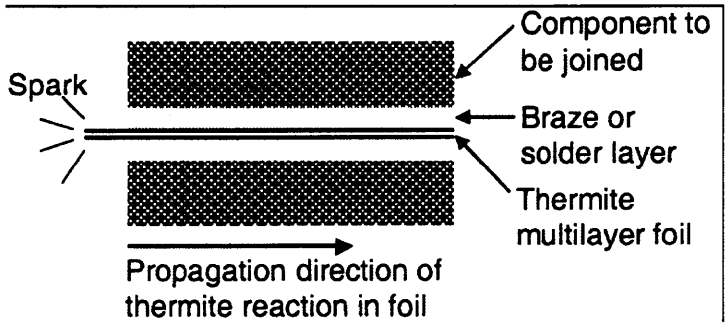

(b)

Figure 1.8 a.Structure of reactive nanofoils, b. Schematic diagram of reactive multilayer foils used for joining two components [15-17].

Magnetron gun sputtering is used to deposit alternate layers of fuel and oxidizer as shown in Figure 1.8a. The thickness of the deposited film can be controlled so that the amount and diffusion distance between reactants can be tailored to optimize the combustion process. Generally, thickness of each layer of thermite based nanofoils is approximately on the order of 1 μm or less and the total foil thickness is approximately 14 μm [15], while the reactive metal based nanofoils have thickness of each bilayer on the order of 25 – 90 nm with a total thickness of the foils ranging from 16 μm to 158 μm. Researchers have studied in detail the synthesis and reaction mechanism of multilayer nanofoils prepared by alternate layers of Al and CuO [15-16].

Advantages: Greater uniformity between reactants is achieved. Sputter deposition of starting materials allows highly dense structure of the foils possessing relatively low porosity. A high degree of control over the scale of individual layers is possible during the synthesis.

Disadvantages: The procedure can be time-consuming, expensive and only small amounts of material can be synthesized at a single time [9]. Material selection is also a challenge because sputter deposition of highly reactive materials is difficult [15-17]. Deposition of materials on the substrate occurs at elevated temperatures which results in a partial reaction of the starting materials; e.g. formation of Cu_4O_3 due to partial reduction of CuO by Al [15, 16].

1.3.2 Nanothermites Prepared by Top Down Approach

These thermites involve the use of micron sized constituens that are refined mechanically to achieve mixing on a nanoscale [18-22] e.g., nanocomposites prepared by ARM.

Arrested Reactive Milling

Arrested Reactive Milling or ARM is a technique based on high energy mechanical milling of starting components. This preparation technique enables fine mixing and produces highly developed reactive interfaces between the components, which result in enhanced reaction rates. ARM is a modification of reactive milling [37, 38], in which a blend of powders capable of an exothermic reaction is ball-milled. If the reaction enthalpy is sufficiently high, a self-sustained reaction is triggered mechanically after a certain milling time. The products are no longer reactive. In ARM, highly reactive nanocomposite powders are formed as a result of arresting (or stopping) the milling process prior to the initiation of the self-sustained reaction. A wide range of materials has been synthesized as shown in Table 1.1.

The materials shown in Table 1.1 were synthesized on a laboratory scale using a SPEX 8000 series shaker mill with a typical batch size ranging from 5 to 10 g, and a Retsch 400 planetary mill with a batch size of up to 100 g per milling vial. Industrial scale production using ARM is possible using mills with a higher capacity, such as attritor mills. Researchers have presented a detailed review of various types of mills used for mechanochemical synthesis as well as mechanical alloying [37, 38].

The ARM process can be readily scaled up using a process model formulated using a discrete element modeling (DEM) code [39]. The milling progress for a range of

parameters can be expressed by a quantity called milling dose, which is proportional to the product of the milling time and the charge ratio (or ball mass to powder mass ratio).

Table1.1 Various Combinations of Starting Materials used in ARM to Produce Reactive Nanocomposites

Nancocomposite Thermites							
Fuel	Oxidizer						
	Fe_2O_3	MoO_3	CuO	Bi_2O_3	WO_3	SrO_2	$NaNO_3$
Al	x	x*	x*	x	x	x	X
Mg		x	x				X
$Al_{0.5}Mg_{0.5}$							X
MgH_2		x	x				
Si		x	x	x			
Zr		x	x	x			X

Reactive Metal-Metalloid composites	
B	Reactive metals: Ti*, Zr

* indicates production of nanocomposite materials with varied stoichiometries.

The DEM numerical scheme (based on a soft sphere interaction model) was used to simulate the milling process in a SPEX Shaker Mill. A sharp temperature increase observed during reactive milling of powders capable of highly exothermic reactions was used in parallel experiments as an indicator of the milling progress. The time of this sharp increase thus determines the time when milling should be interrupted for actual nanocomposite synthesis. Correlating measurements and predictions of the DEM-based model for this time, projection to different milling conditions is possible.

Advantages: Fine mixing of reactants is achieved on a nanoscale. Each nanocomposite particle is of several dimensions on the scale of 1-100 μm, as a result handling of powders is simple. These materials can be compared to the nano-composites produced by mixing nanopowders of aluminum and metal oxides. Aluminum nanopowders used for those materials are produced by one of the vapor condensation techniques and require

passivation. The passivated aluminum nanoparticles have at least a 2 – 4 nm oxide layer [40, 41] resulting in dramatic decrease of the active fuel content. On the other hand, passivation of micron sized nanocomposite powders produced by ARM affects only their external surface. Therefore bulk of the reactive interface area existing between aluminum and another component within such particles remains intact. ARM is less expensive and can be easily scaled up for higher production demands. Wide array of material systems can be used to prepare reactive nanocomposites.

Disadvantages: Extended milling time results in a localized partial reaction. As a result complete heat of reaction between the constituents cannot be exploited. The milling media as well as products of partial reaction introduce impurities in the products [22-23]. Some of the ARM-prepared nanocomposites are sensitive to electrostatic discharge and require additional protective coatings for safe handling.

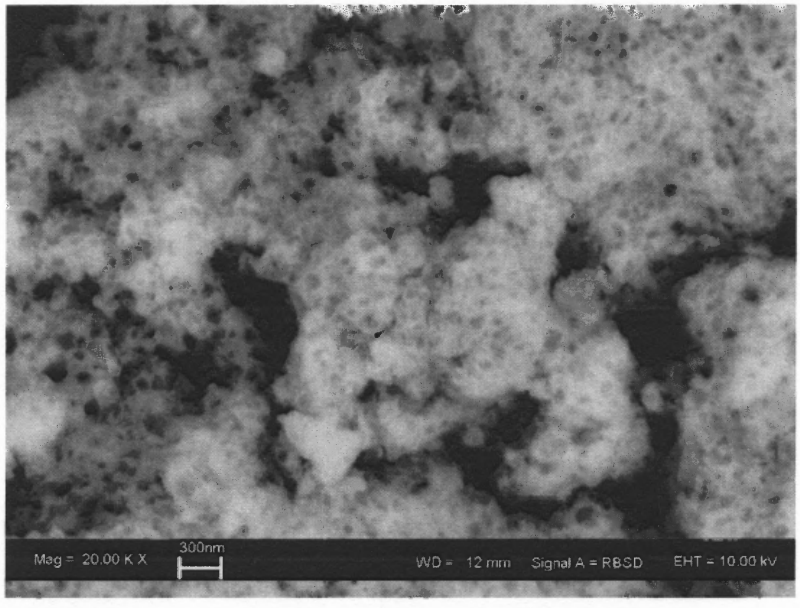

Figure 1.9 SEM image of B-Ti nanocomposite particle synthesized by ARM. Titanium matrix is light. Embedded dark nano-sized particles are boron.

CHAPTER 2

SYNTHESIS OF Al-MoO_3 NANOCOMPOSITES BY ARRESTED REACTIVE MILLING

2.1 Introduction

Thermite reactions that use aluminum as the reducing agent, also called aluminothermic reactions, are highly exothermic [2]. Once initiated these reactions become self-sustaining. Due to high reaction enthalpy of the Al+MoO_3 system, the combustion characteristics of this formulation have been studied previously [7, 8]. Both studies were conducted on composites formulated using nano-aluminum, which is usually passivated with an oxide layer. This layer is generally 2 to 3 nm thick, reducing the available energy. Further, those formulations could only be consolidated to 38 % of the theoretical maximum density (TMD). In order to overcome the disadvantages of using nano-aluminum and to achieve near TMD, in this work, Al-MoO_3 nanocomposites were synthesized using ARM [18-22], a technique derived from reactive milling [37, 38]. As explained in Chapter 1, the reactants are ball-milled, and the milling is interrupted before a spontaneous reaction is mechanically triggered. Extended milling results in the synthesis of composite particles with a highly refined structure. The milling time at which the reaction is mechanically triggered effectively sets a limit to the achievable degree of refinement. However, the refinement can be influenced by the specific milling parameters chosen, such as mass of powder, mass of the milling media, ratio of sample to milling media and the use of process control agents. This work focuses on finding optimized milling conditions for manufacturing Al-MoO_3 powders by ARM. The scientific goal of

this work is to establish a correlation between the milling parameters and structure, properties, and performance of the nanocomposites.

2.2 Experimental

A shaker mill (8000 series by Spex CertiPrep) was employed in this research. Flat-ended steel vials were used along with milling media of 5 mm diameter. Milling balls made of alumina (Al_2O_3), zirconia (ZrO_2), steel, and tungsten carbide (WC) were used. Figure 2.1 shows an image of the different milling balls. Alumina and tungsten carbide balls had broad equatorial bands. The number of milling balls was selected to be 55 pcs, to achieve the ball to powder mass ratio (BPR) of 5 for steel balls. This BPR was selected based on earlier experiments [39]. In experiments with other milling media, the number of milling balls remained constant, so that the ball to powder mass ratio (BPR) varied from 3 to 9 as a function of the density of milling media as listed in Table 2.1. Starting blends were prepared in the stoichiometric proportion ($2Al + MoO_3$) from powders of elemental aluminum (99% pure, -325 mesh by Atlantic Equipment Engineers) and molybdenum trioxide MoO_3 (99.95% pure, by Alfa Aesar). Figure 2.2 shows a backscattered electron SEM image of a cross-section of blended particles embedded into epoxy.

Table 2.1 Milling Parameters used for the Synthesis of Al-MoO_3 Nanocomposites

Milling Media	Density [g/cm^3]	BPR	Milling Time [min]		
			Dry milled	1ml of hexane	8ml of hexane
Alumina	4.0	3.0	1.5	90*	60*
Zirconia	5.8	4.5	0.5	24	60*
Steel	7.8	5.0	2.0	19	60*
Tungsten Carbide	15.7	9.3	1.5	7.5	60*

* No reaction

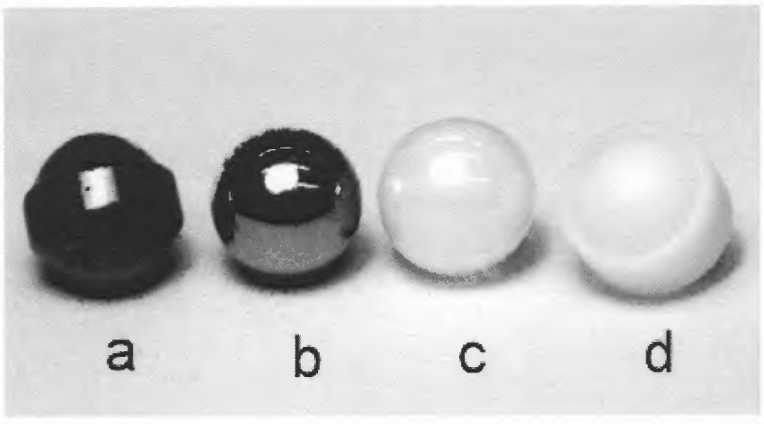

Figure 2.1 Milling media used in the synthesis of the Al-MoO3 nanocomposites; a. tungsten carbide, b. Steel, c. Zirconia and d.Alumina.

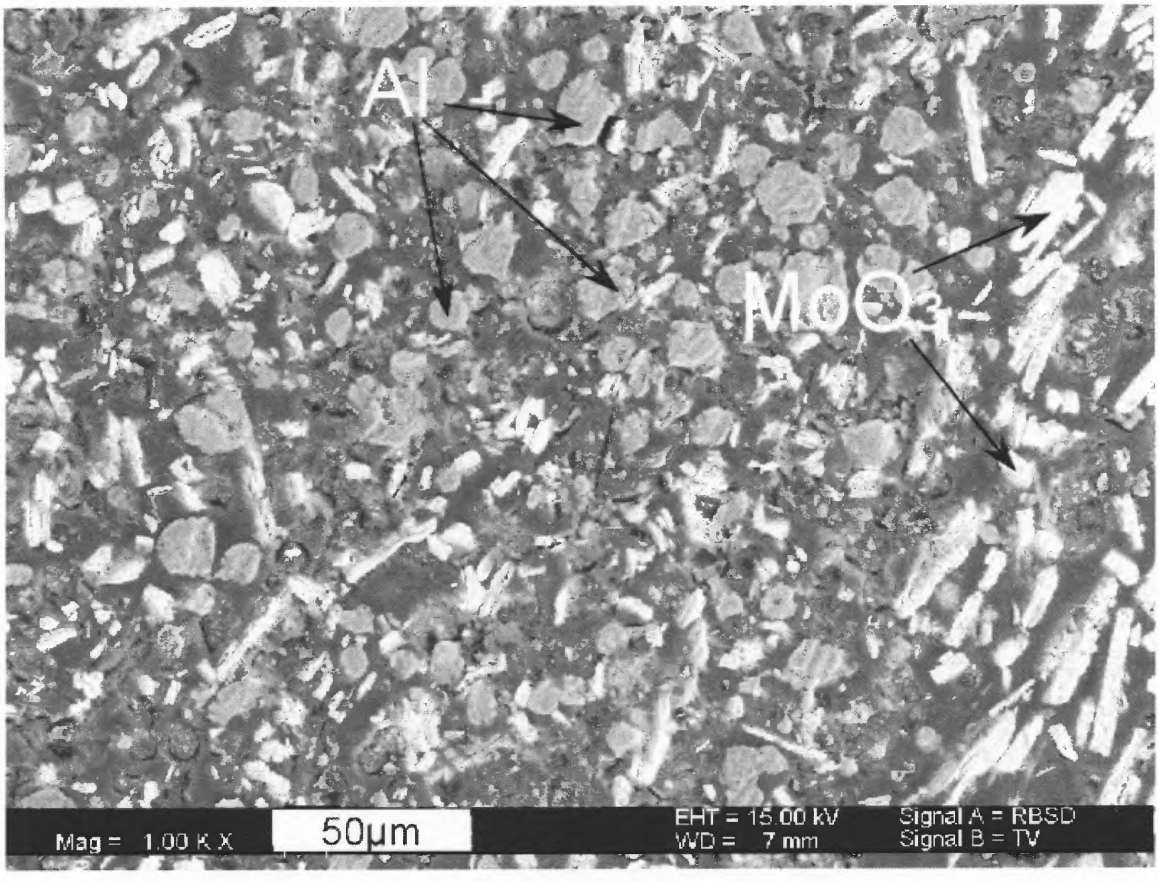

Figure 2.2 Backscattered electron SEM image of the initial blend of materials. The dark background represents epoxy, the bright particles are MoO_3 and gray particles are aluminum.

Synthesis of the Al-MoO_3 nanocomposites was carried out in argon. A specific amount of hexane (C_6H_{14}) was added as process control agent (PCA) to inhibit cold-welding and partial reaction during milling (see Table 2.1). The process temperature was monitored using a thermistor attached to the side of the milling vial and connected to a digital data logger. The instant of reaction was marked by a sharp rise in the vial temperature [18-22]. Reactive nanocomposites were prepared by arresting the milling before the reaction was triggered. The milling times required to initiate the reaction varied with the milling media and the amount of PCA used. For certain conditions the reaction was never triggered, therefore the milling was stopped after specific durations of 90 and 60 min (see Table 2.1 for details). Each batch was prepared with a powder mass of 5 g.

2.3 Sample Characterization

Morphology and composition of the nanocomposites were examined on a LEO 1530 Field Emission Scanning Electron Microscope (SEM) operated at 10 kV. The samples were embedded in epoxy and cross-sectioned. The phase composition was determined for each sample by x-ray diffraction (XRD). The XRD was performed on a Phillips X'pert MRD powder diffractometer operated at 45 kV and 40 mA using Cu Kα radiation (λ = 1.5438 Å). Temperature-dependent structural transformations were determined by differential scanning calorimetry (DSC) using a Netzsch Simultaneous Thermal Analyzer STA409 PC. Alumina pans were used and the furnace was flushed with argon at approximately 10 ml/min. DSC traces were recorded between room temperature and 1013 K with heating rates varying from 5 to 20 K/min. The temperature is accurate

within ±1 K. The DSC measurements were performed in Ar in order to observe the effect of thermite reactions on powder ignition. The effect of ambient oxidizer (air) for the ignition experiments was negligible as discussed below.

2.3.1 Ignition Set Up

Preliminary ignition experiments with thermite powders were performed in both argon and room air environments [21]. No effect of gas environments on the ignition kinetics was detected. Therefore, in the research presented in this chapter, the powders were ignited in air only on the surface of an electrically heated metal filament. A simplified diagram of the experimental setup is shown in Figure 2.3. Further experimental details have been described elsewhere [24, 27]. A 0.5 mm diameter Nichrome wire mounted in a controlled environment chamber was used as a filament. The total length of the heated filament was 4.5 cm; however the length of the powder coated portion was approximately 1 cm. A small amount of powder was mixed with hexane and a thin layer of the slurry was deposited on the filament surface using a soft paintbrush. The coating was completely dried before the filament was electrically heated. To observe ignition, a silicon photodiode (DET110 by Thorlabs, Inc.) was focused on the powder coating. The temperature history of the heated filament was measured using a high-speed infrared pyrometer (DP1581 by Omega Engineering, Inc.). The pyrometer was focused on the uncoated surface of the filament adjacent to the powder coating. Thus, the temperature of the heated powder was not measured directly, but inferred from the measured filament temperature [42]. A constant value of the filament emissivity, ε=0.75, which is the average emissivity for Nichrome in the temperature range of 770 -1270 K [43], was used

consistently. The filament heating rate was controlled by varying the DC voltage and using a set of resistors to adjust the current. The heating rates used in these experiments were on the order of $10^3 - 10^4$ K/s. The specific heating rates achieved in individual runs were determined from the recorded filament temperature histories. Both the photodiode and pyrometer outputs were recorded using a PCI-MIO-16E-4 DAQ board by National Instruments, and a LabView-based digital oscilloscope.

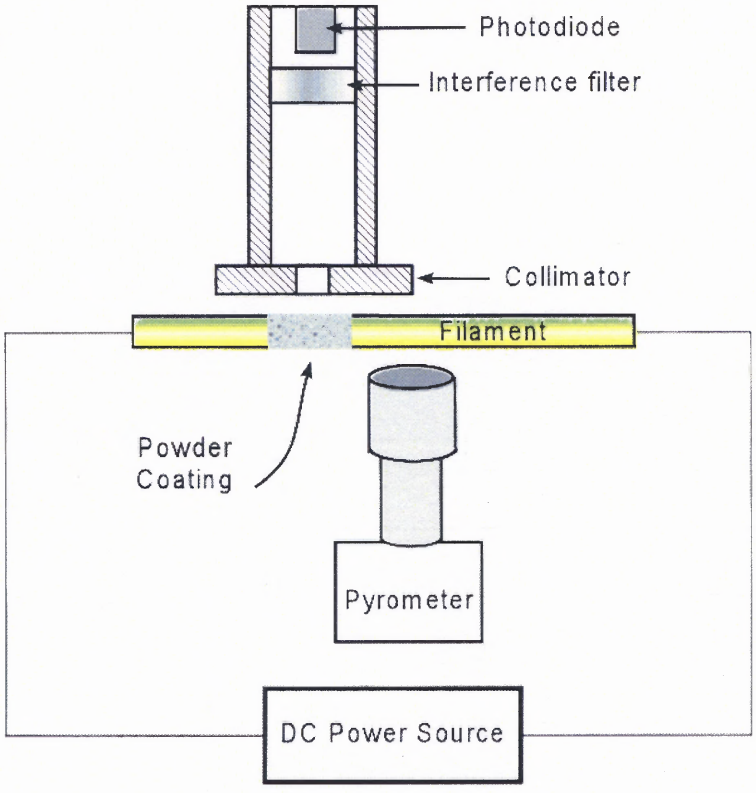

Figure 2.3 Experimental setup used for measurements of ignition temperatures.

Figure 2.4 shows a temperature trace corresponding to a specific setting of the electric circuit and two photodiode signatures recorded at this setting for two different powder samples undergoing ignition. The shaded portion of the plot shows the range of temperatures for which the pyrometer was calibrated. For the diode trace labeled as 1 ml, the ignition resulting in a sharp spike in the photodiode signal is observed at about 2350

ms. At that time, the pyrometer output is within the calibrated temperature range and thus, the ignition temperature is measured directly. For the other sample, the trace labeled 8 ml, the ignition is observed at about 1250 ms and at a temperature that is too low to measure directly from the pyrometer trace. Therefore, for such experiments the ignition temperature was evaluated using a numerical transient model of the filament heating. The model considered the temperature-dependent resistance of the filament, convective heat losses, electric voltage applied, and constant temperature boundary conditions for the filament ends clamped to the massive electrodes. The predicted temperature history of the filament essentially coincided with the experimental data for the range where the temperature measurements were calibrated. Thus, the calculated temperatures corresponding to the lower-temperature portion of the filament heating history could be used to evaluate the ignition temperature as illustrated in Figure 2.4.

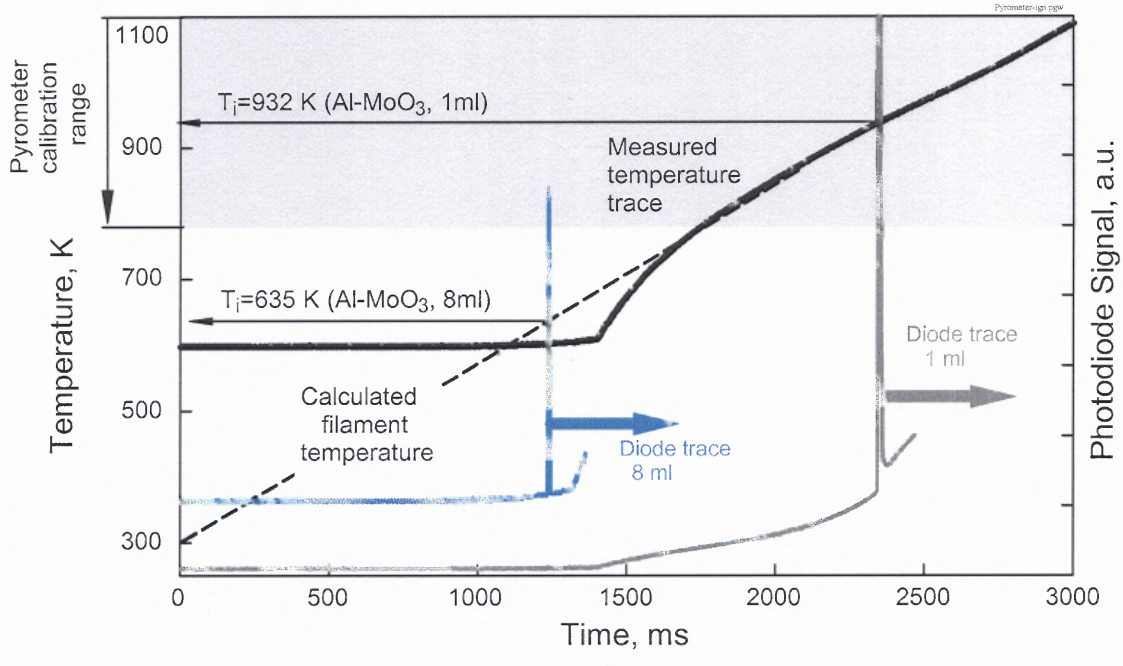

Figure 2.4 Photodiode and temperature traces recorded during ignition experiments of different Al-MoO_3 nanocomposite.

2.4 Results And Discussion

2.4.1 SEM Analysis

Overviews of cross-sectioned samples of the materials prepared under different conditions are shown in Figure 2.5. The sample arrested after 1.5 min and milled with the lowest density milling balls (Al_2O_3) appears to be very similar to the starting powder with little difference in the size, shape, or morphology of the aluminum and molybdenum oxide powders. On the contrary, the sample milled for the same time using the highest density milling balls (WC) consists of very large composite particles, in which Al and MoO_3 layers are sandwiched together. In every case, the reaction was initiated mechanically well before the components were intimately mixed together. Adding PCA allows one to extend the milling time in both cases, resulting in reduced particle sizes and formation of nanocomposites. The mixing appears to be more uniform for both Al_2O_3 and WC milling media. A self-sustaining reaction was never initiated for samples milled with the low-density balls and the milling was therefore interrupted after an extended period of time (90 min). The sample contains a large number of fine particles of individual components. Such particles are not observed in the sample produced with the high-density balls and arrested before the reaction initiation (~ 7.5 min). The level of refinement in the composite particles produced with WC balls varies widely from particle to particle. A better comparison of the powders produced with different milling media can be made from the high-magnification images in Figure 2.6 showing cross-sectioned samples milled for 60 minutes and with 8 ml of PCA using all four types of milling balls. For all cases, the mixing of reactive components is achieved on a scale of about 100 nm. The overall scale of mixing seems to be coarsest for the sample prepared with Al_2O_3

milling balls. The difference in the scale of mixing between other samples is hard to assess from the images. The bright particles identified by energy-dispersive x-ray spectroscopy as Mo and appropriately labeled in the image of a sample prepared with the WC balls indicate that undesirable reaction between the components producing Mo and Al_2O_3 started, but was not self-sustained during milling.

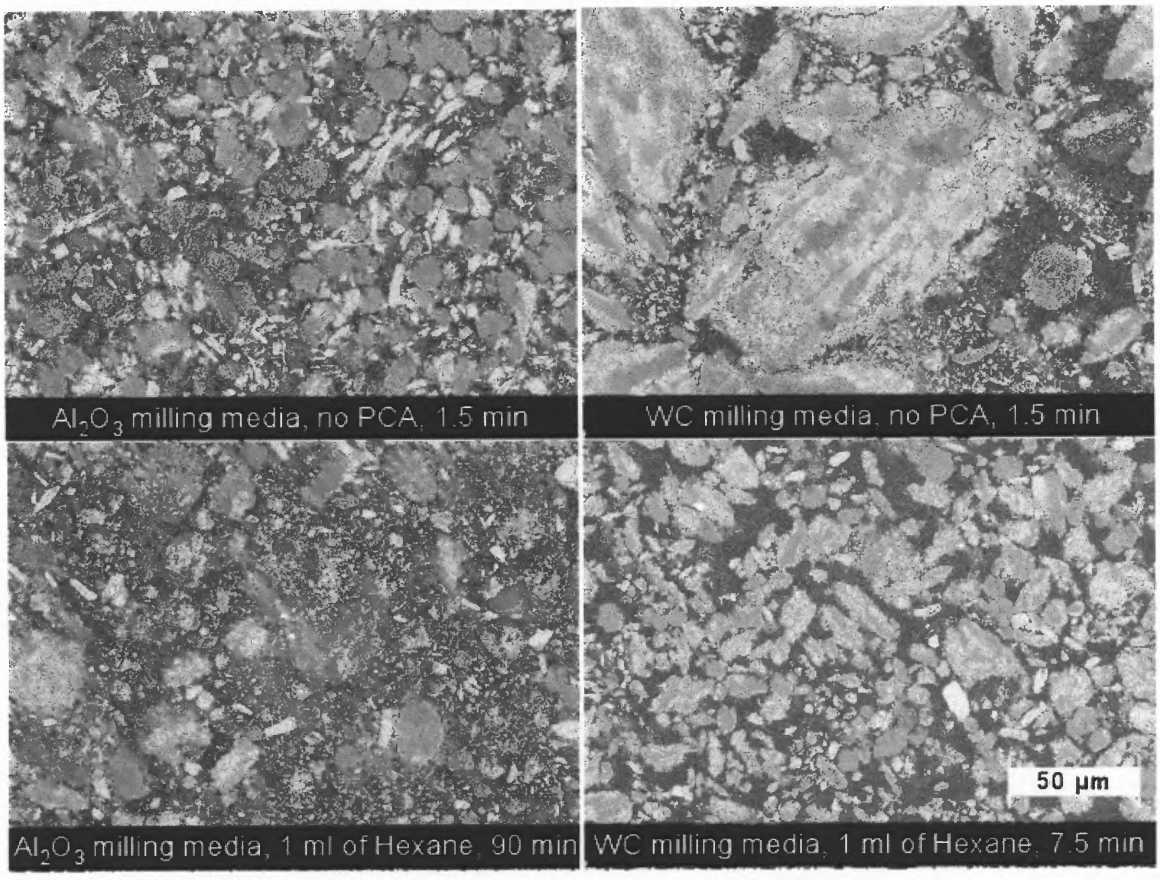

Figure 2.5 Backscattered electron SEM images of the cross-sectioned $2Al+MoO_3$ composites prepared under different milling conditions.

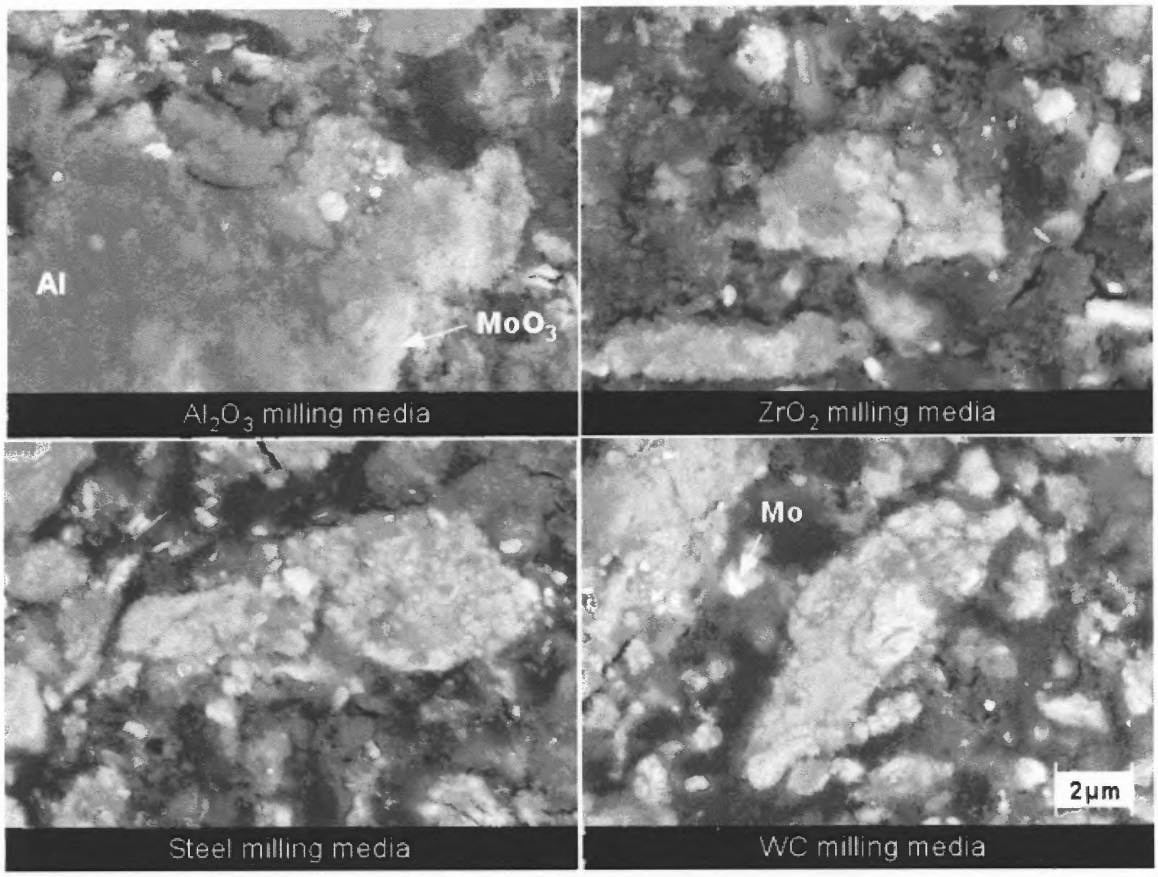

Figure 2.6 High magnification backscattered electron SEM images of the cross-sectioned samples milled for 60 min with 8ml of hexane using different milling media.

2.4.2 XRD Analysis

XRD patterns of nanocomposites synthesized using different milling media are shown in Figure 2.7. In addition to Al and MoO_3 peaks, the peaks of $MoO_3H_{0.5}$ were observed for samples milled with alumina and zirconia. With increased milling times, peaks corresponding to Mo, MoO_2, and Al_2O_3 appear, indicating the beginning of decomposition of MoO_3 and oxidation of Al. Some XRD patterns show an abnormal intensity distribution of the MoO_3 peaks due to preferred orientation [44]. Strong peaks corresponding to tungsten carbide, iron and alumina were observed for samples milled with the respective milling media. Contamination from the milling media was especially

high in the cases of alumina and tungsten carbide, likely because they were not entirely spherical, as shown in Figure 2.1.

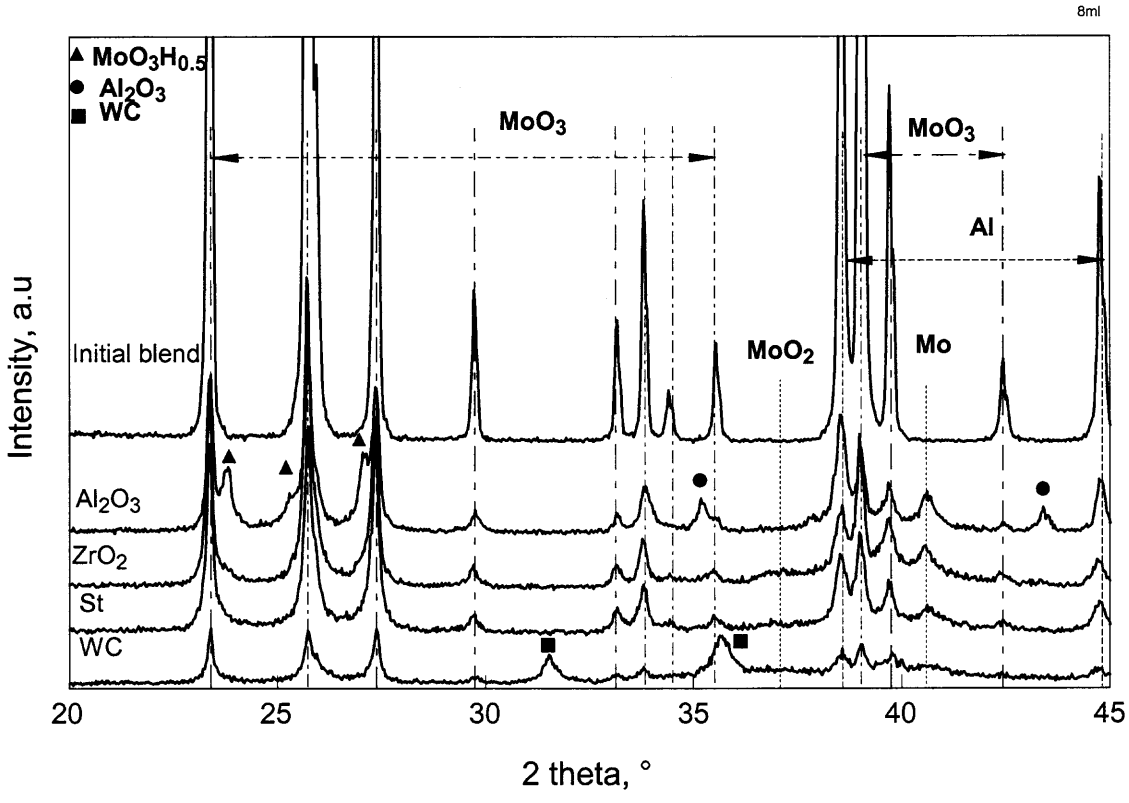

Figure 2.7 XRD patterns of the initial blend and the samples milled with different milling media for a milling time of 60 min.

The average crystallite size of each sample was estimated by whole pattern refinement of the XRD patterns using the GSAS software (Generalized Structural Analysis System) [45]. The parameter describing the Lorentzian peak width was used to estimate the crystallite size. Figure 2.8 shows the change in the crystallite size for both Al and MoO_3 as a function of density of the milling media for the samples milled for 60 min using 8 ml of hexane as PCA. The error bars shown in Figure 2.8 represent the standard deviation resulting from the least squares fitting procedure. Specifically, they

do not relate in any way to the true size distribution of crystallites with realistic shapes. It is estimated that the actual variance of the average crystallite size is on the order of 10 %.

Consistent decrease in the crystallite sizes with increase in the milling time was observed for all samples. It appears that the variation of the crystallite size of MoO_3 is greater than that of Al. For both, the observed crystallite size levels out at higher ball densities.

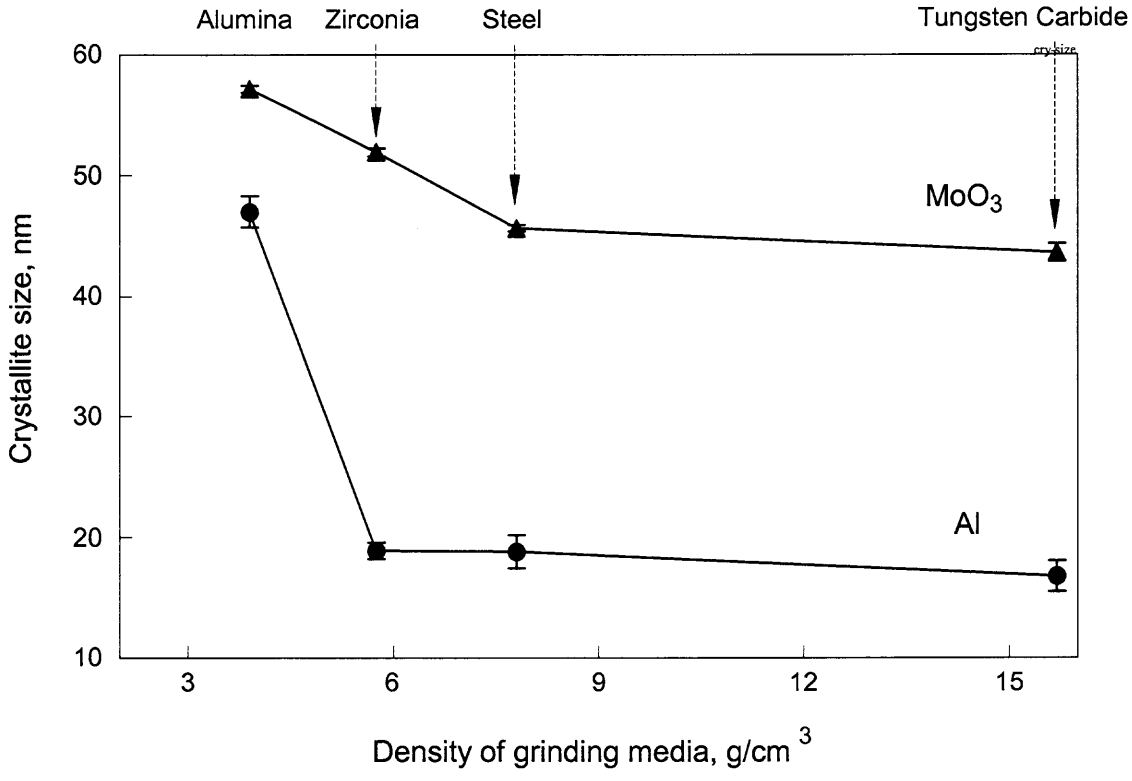

Figure 2.8 Change in the crystallite size of the Al and MoO_3 as a function of the density of the milling media for the samples milled for 60 min.

XRD patterns were also compared to evaluate the degree to which MoO_3 was reduced as a function of the milling media density. The average oxidation state of Mo was calculated based on the overall material composition obtained from the XRD pattern refinement. The change of that oxidation state, compared to the fully oxidized state of

MoO_3 as 0% and metallic Mo as 100%, is shown in Figure 2.9 as a function of the milling media density. This is discussed in further detail in the following section.

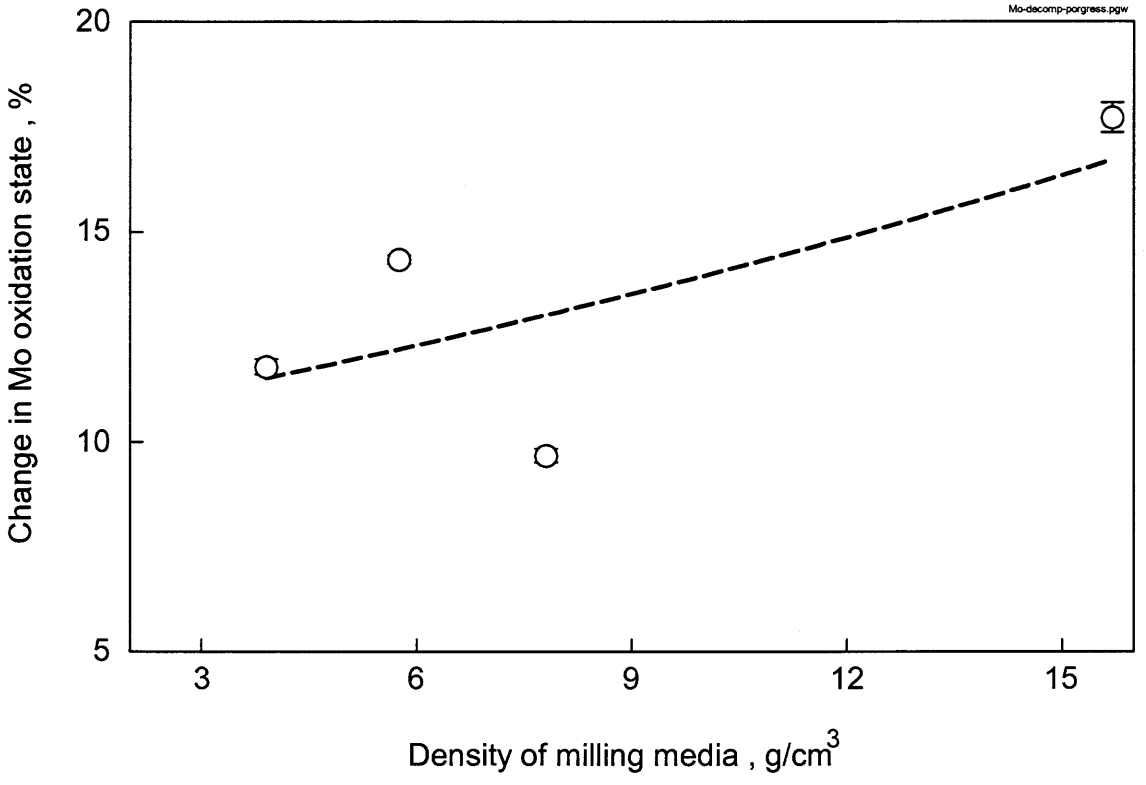

Figure 2.9 Change in the average oxidation state of Mo as a function of density of the milling media for the samples milled for 60 min.

The error bars in Figure 2.9 reflect the uncertainty of the least squares refinement procedure. The results show that some partial reaction occurs at any milling condition. The extent of the MoO_3 reduction occurring during milling is affected by the milling media density. Milling with higher density media at otherwise constant milling parameters reduces MoO_3 more strongly. This conclusion is consistent with the SEM observations (see Figures. 2.5 and 2.6) showing noticeable presence of metallic Mo in the samples milled with WC balls.

2.4.3 Thermal Analysis

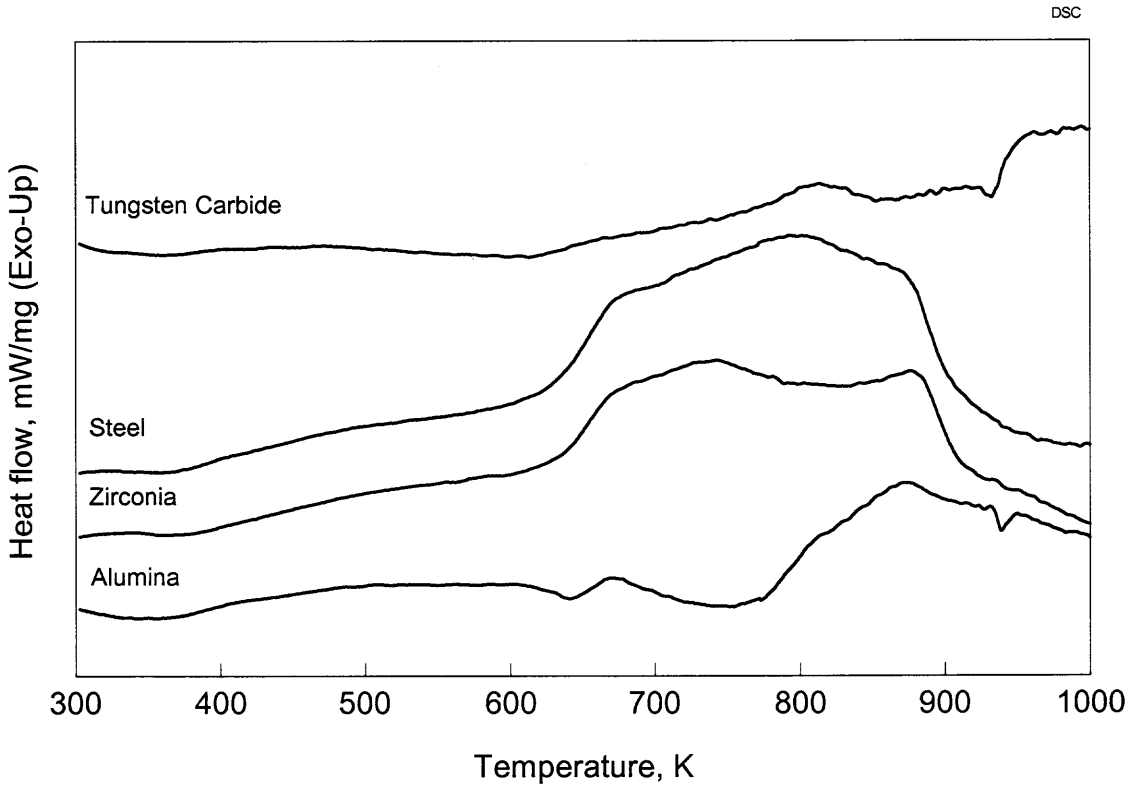

Figure 2.10 DSC traces of the samples milled with 8ml of hexane (60 min) using different milling media.

A set of baseline corrected DSC traces recorded at a heating rate of 10 K/min for the samples milled with 8 ml of hexane for 60 min is shown in Figure 2.10. The strongest exothermic events are observed to occur for all samples between 600 and 900 K. In general, the intensity of exothermic events is higher for the samples milled with steel and zirconia balls. Aluminum melting (endothermic peak) is observed around 935 K. The magnitude of the melting peak can not be usefully measured, however. As the estimate of the crystallite size above indicates, milling results in nanometer-sized Al crystallites which may melt over a wide temperature range, and below the bulk melting temperature [46]. This range overlaps with the exothermic effects and is difficult to delimit. The

lower intensity of exothermic peaks of the sample milled with WC balls, for which the crystallite sizes of both Al and MoO_3 are the smallest (see Figure 2.8) can be explained by a more significant MoO_3 reduction during the milling. Mo, and layers of MoO_2 and Al_2O_3 formed during milling, separate the remaining finely divided Al and MoO_3 slowing down the reaction.

As noted above, the XRD patterns of the samples after the entire heating cycle in the DSC show the presence of MoO_2 along with Al_2O_3. This suggests that over the heating cycle only partial reduction occurred. For comparison purposes, the DSC results were therefore evaluated in terms of the following reaction:

$$MoO_3 + 2\ Al = MoO_2 + 1/3(Al_2O_3) + 4/3\ Al + 2027.5\ J/g \quad [47] \tag{2.1}$$

The DSC traces were integrated, and the results were compared to the theoretical energy release of Reaction (2.1). This gave an estimate for the progress of the reaction:

$$\xi_{DSC}(T) = \Delta H(T) / \Delta H_{reference} \tag{2.2}$$

where $\Delta H(T)$ is the exothermic heat release from the DSC curves integrated up to the temperature T and $\Delta H_{reference}$ is 2027.5 J/g [47] (see Reaction 2.1). At the same time, the progress of Reaction (2.1) was estimated from the quantitative XRD phase analysis based on the average oxidation state ν of Mo in the sample.

$$\bar{\nu} = \frac{\sum \nu_i \cdot x_i}{\sum x_i} \tag{2.3}$$

where ν denotes the oxidation state, and x the molar fraction of Mo-bearing phase i. The average oxidation state of Mo in the unreacted material is 6, while Mo in the completely reacted material has an average oxidation state of 0. In the products of Reaction (2.1),

Mo has an average oxidation state of 4. Considering only Reaction (2.1), the reaction progress can be expressed as

$$\xi_{XRD} = (6 - \bar{\nu})/2 \tag{2.4}$$

The value calculated from Eq. (2.4) should be directly comparable to the value calculated from Eq. (2.2). If ξ_{XRD} is the degree to which the material has converted to the products of Reaction (2.1), then $1-\xi_{XRD}$ measures the extent to which Reaction (2.1) can still proceed. Thus, a comparison can be made between $1-\xi_{XRD}(T_0)$ for as-milled samples (or the samples at room temperature T_0=293 K) and $\xi_{DSC}(T_{max})$ determined by heating these samples in the DSC to the maximum experimental temperature T_{max} = 1013 K. Table 2.2 and Figure 2.11 show the results as a function of density of the milling media. The correlation between the values of the reaction progress determined from two independent sources is reasonable, especially considering the uncertainty of integrating the DSC over a wide temperature interval, where the assessment of a reliable baseline is problematic.

Table 2.2 Comparison of Reaction Progress by DSC and by Quantitative Phase Analysis of as-milled Material

Media	DSC		XRD	
ρ [g/cm^3]	ΔH [J/g]	$\xi_{DSC}(T_{max}=1013\ K)$	$\bar{\nu}$	$1-\xi_{XRD}(T_0)$
4.0	1197	0.590	5.29	0.646
5.8	1450	0.715	5.14	0.570
7.8	1839	0.907	5.42	0.710
15.7	745	0.368	4.94	0.469

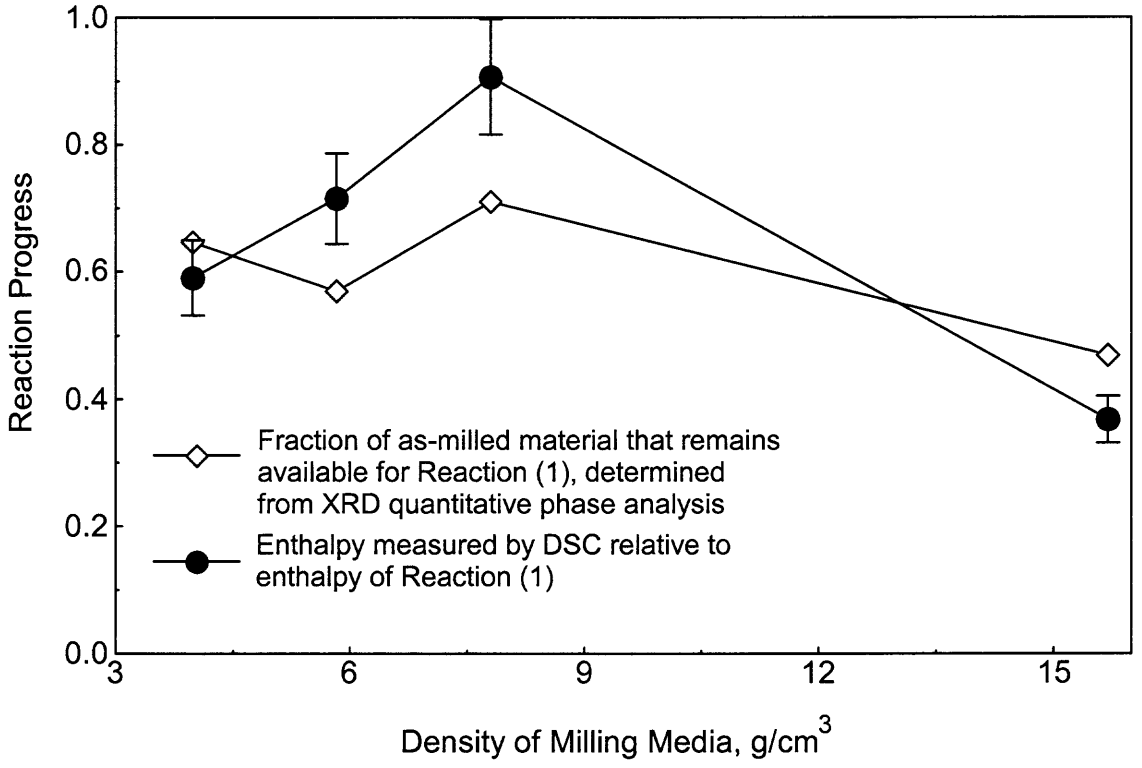

Figure 2.11 Comparison of enthalpy values determined by DSC and degree of reaction estimated from quantitative phase analysis.

For the material milled with steel media, samples were recovered from the DSC runs at intermediate temperatures. Therefore, it was now possible to compare reaction progress determined from the quantitative phase analysis of these samples, to partial integrals of the corresponding DSC trace at the same temperatures that the samples were recovered from. Since the results of the quantitative phase analysis show that the as-milled material is already partially reacted (see Table 2.2), the reaction progress $\xi_{DSC}(T)$ (Eq. 2.2) was corrected by the fraction of reactive material in the as-milled sample

$$\xi'_{DSC}(T) = \Delta H(T) / \Delta H_{reference} .(1- \xi_{XRD}(T_0)) \qquad (2.5)$$

where the subscript 0 refers to the as-milled material. Similarly, the reaction progress at intermediate temperatures as determined from quantitative XRD phase analysis was scaled to account for the fraction of the as-milled material that had already reacted:

$$\xi'_{XRD}(T) = \frac{\xi_{XRD}(T) - \xi_{XRD}(T_0)}{1 - \xi_{XRD}(T_0)} \tag{2.6}$$

The values for $\xi'_{DSC}(T)$ and $\xi'_{XRD}(T)$ are shown in Table 2.3 and Figure 2.12. An obvious contradiction is the apparent increase of the reaction progress above 100 % as determined by Eq. (2.5). Aside from the fact that the DSC integration is tentative, this likely indicates that the reaction may have progressed further than suggested by Reaction (2.1). This may not be reflected accurately in the quantitative phase analysis. The average oxidation state of Mo in the sample (Eq. 2.3) is strongly influenced by the presence of metallic Mo. As only 2 XRD reflections of Mo are observed in the XRD patterns, and overlap with other peaks is strong, small errors in the quantification of this phase will have strong effects on the apparent reaction progress. In summary, both values of the reaction progress as derived from XRD and DSC up to 753 K agree reasonably well with each other.

Table 2.3 Relative Reaction Progress by of Samples Recovered from Intermediate Temperatures.

	DSC		XRD		
T [K]	$\Delta H_T/\Delta H_{Tmax=1013\ K}$	$\xi'_{DSC}(T)$	$\bar{\nu}(T)$	$\xi_{XRD}(T)$	$\xi'_{XRD}(T)$
293	-0-	0.000	5.42	0.290	-0-
593	0.126	0.160	5.30	0.352	0.086
753	0.479	0.607	4.55	0.724	0.611
1013	-1-	1.267	4.33	0.835	0.768

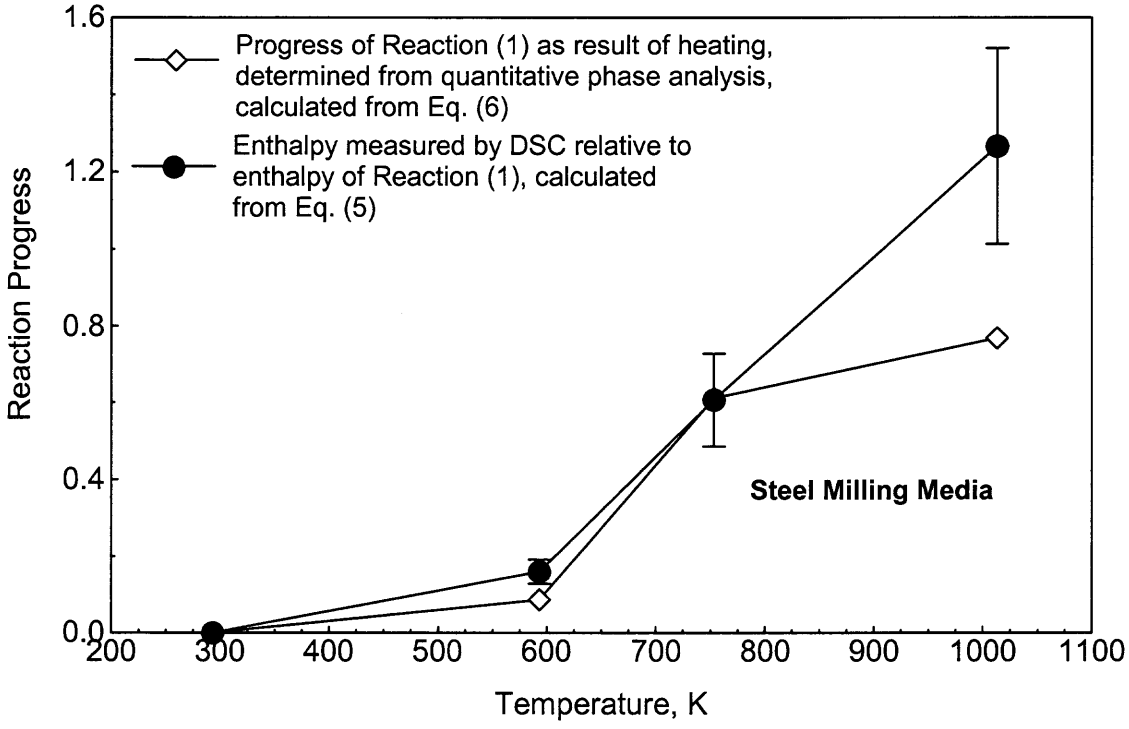

Figure 2.12 Comparison of relative reaction progress in partially heated samples as determined by quantitative phase analysis and DSC.

2.4.4 Ignition

Figure 2.13 shows the results of the ignition experiments performed in air for the Al-MoO_3 nanocomposites synthesized using different milling media. The filled symbols indicate the ignition data of the samples milled with 8 ml of hexane, the open symbols represent the samples milled with 1 ml of hexane and the shaded symbols indicate dry milled samples. Ignition was not observed for the sample milled with tungsten carbide balls and 8 ml of hexane, at medium and low heating rates, and for dry milled samples using alumina and tungsten carbide balls at all heating rates. Figure 2.13 shows that softer milling with larger amounts of hexane and respectively extended milling time generally results in higher degree of structural refinement, and hence in a decrease of the ignition temperature. At the same time, despite longer milling time (90 min vs 60 min) the

ignition temperature of the sample milled with alumina and 1 ml of hexane is higher as compared to all samples milled with 8 ml of hexane.

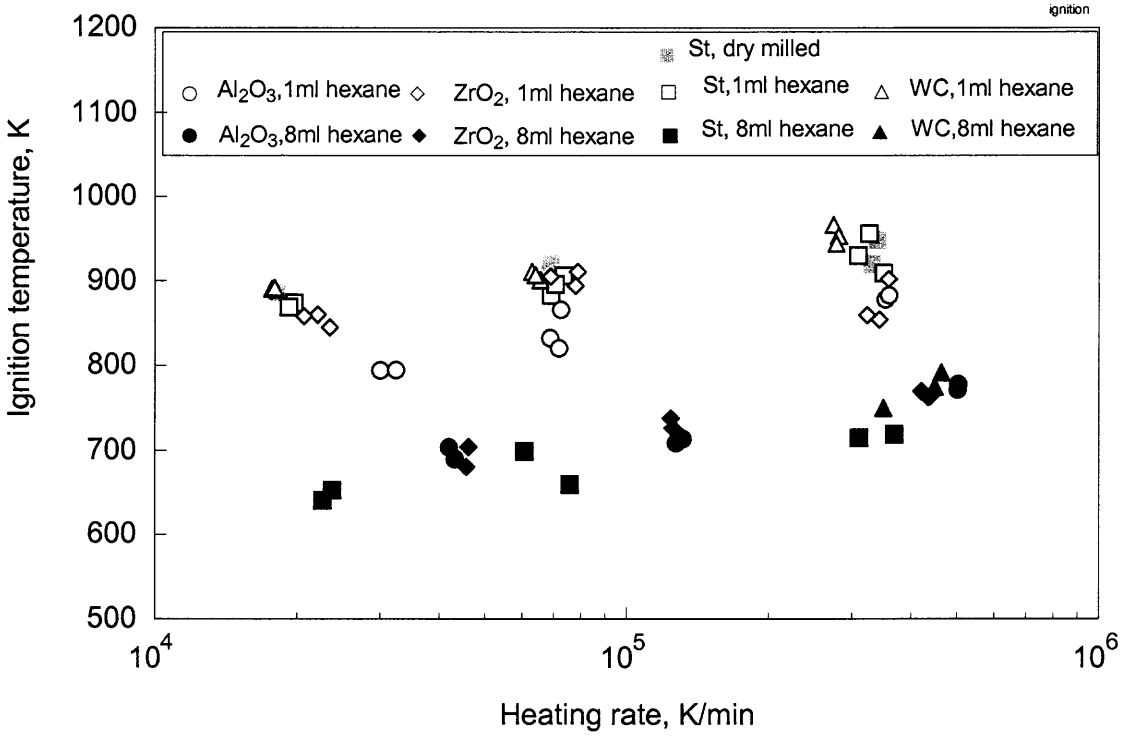

Figure 2.13 Ignition temperatures of different Al-MoO_3 nanocomposites as a function of heating rate.

Of all samples milled with 8 ml of hexane, ignition temperatures are the lowest for the materials prepared using steel milling media. This effect of density of milling media is consistent with the results of the thermal analysis for these samples. Powders with optimum degrees of structural refinement result in higher intensities of exothermic events coupled with lower ignition temperatures, whereas higher ignition temperatures can be attributed to either lower degrees of structural refinement coupled with lower intensities of exothermic events during thermal analysis, or to a higher degree of Mo reduction during the milling process. The products of partial reaction further participate in the milling process thereby increasing the diffusion distance between the starting

materials. In both cases the reaction rate in DSC as well as in ignition experiments is impeded.

2.5 Conclusions

Stoichiometric 2Al + MoO_3 powders with increasing degrees of structural refinement were synthesized by increasing the milling intensity using milling media with consistently increased densities and by varying the amounts of the liquid PCA. An increase in the milling intensity also results in an increased rate of undesired partial reaction between the starting materials. Milling media with densities in the range of 5 to 8 g/cm^3 result in the highest structural refinement accompanied by the lowest degree of partial reaction. Powders produced with such milling media are most reactive as indicated by the lowest amounts of unoxidized aluminum remaining upon their slow heating to 935 K. The highest reactivity of these powders is also supported by the observed strongest exothermic feature in the DSC traces. Filament ignition tests showed that the same sample powders have the lowest ignition temperatures as compared to other powders with the same bulk compositions. Steel milling media are recommended for the optimized milling conditions required for manufacturing of reactive Al-MoO_3 nanocomposite powders by ARM.

CHAPTER 3

KINETIC ANALYSIS OF THERMITE REACTIONS IN Al-MoO_3 NANOCOMPOSITE

3.1 Introduction

Nanometer-scaled metallic energetic materials have gained relevance in recent years due to their potentially very high reaction rates [4-18]. In order to use these materials in propellants, explosives or pyrotechnics, their reaction behavior must be known at the operating conditions of a specific application. Combustion applications are generally characterized by high heating rates in the range 10^3–10^6 K/s. Reactions at low temperatures under static conditions are relevant for storage and aging of these materials. Experimental investigations of reaction mechanisms in nanometer-scaled thermites are generally conducted by thermal analysis, and are therefore limited to low heating rates in the relatively narrow range of 0.01 – 1 K/s. The phenomena observed by thermal analysis frequently indicate several concurrent exothermic and endothermic processes that are difficult to separate, and therefore difficult to project to slower or faster heating regimes [48]. While separate experiments in fast heating regimes, as relevant for ignition and combustion processes result in descriptive parameters useful for applications in the range of heating rates covered, the data are difficult to reduce to obtain conclusive evidence for specific reaction mechanisms [49]. The present study uses both thermal analysis and high heating rate ignition experiments to quantify the ignition kinetics and identify the related reaction mechanism. Stoichiometric Al-MoO_3 nanocomposite powders are selected for this initial investigation.

3.2 Experimental

Nanocomposite thermite powders with balanced $2Al+MoO_3$ composition were prepared by arrested reactive milling as described in Chapter 2 [22]. The synthesis of reactive nanocomposites by mechanical milling has been documented for a number of thermite systems as well as materials with highly exothermic formation of intermetallic phases [18]. The specific material for this study was prepared by milling of the component powders in 50-ml steel vials using a SPEX 8000D shaker mill. Steel balls of 5 mm diameter were used as milling media, the charge ratio was 5. Milling for 60 minutes was carried out with 8 mL of hexane as process control agent. The resulting nanocomposite powders were characterized by X-ray diffraction (XRD) and scanning electron microscopy [22]. Figure 3.1 shows a representative backscattered electron image of an $Al\text{-}MoO_3$ nanothermite. The sample was embedded into epoxy and cross-sectioned. The phase contrast within the particles shows the formation of fully dense composites of Al and MoO_3 mixed on the scale of under 100 nm.

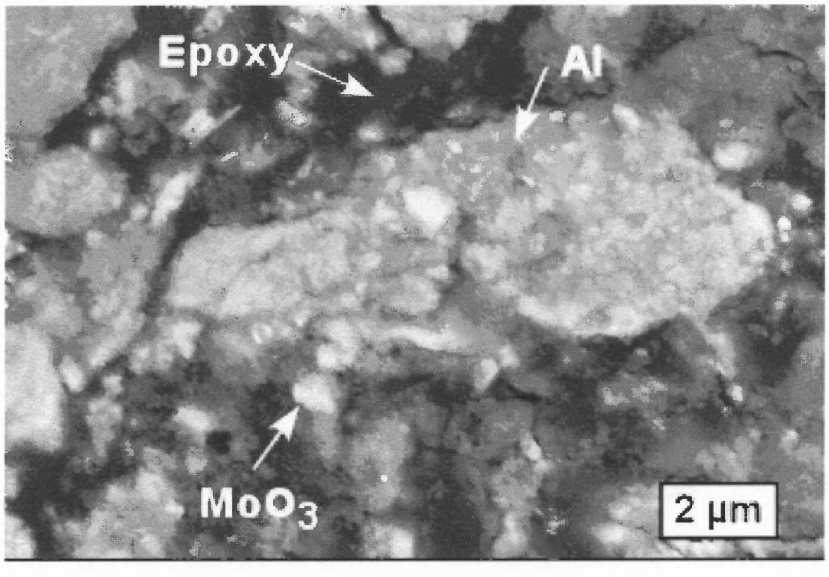

Figure 3.1 Backscattered electron image of an $Al\text{-}MoO_3$ nanothermite prepared by arrested reactive milling.

Reactions occurring in the nanothermites during slow heating were characterized by Differential Scanning Calorimetry (DSC) using a Netzsch STA409PC thermal analyzer. Platinum sample pans covered with lids were used, and the furnace was flushed with argon at approximately 10 ml/min. DSC traces were recorded with heating rates varying from 1 to 5 K/min. The temperature range was limited to a maximum of 1013 K (740 °C) in order to avoid melting and decomposition of MoO_3 above 1068 K (795 °C). After the initial heating cycle, the same sample was held at 1013 K for 30 min, and then heated again at the same heating rate in order to obtain a baseline for the measurement. It was assumed that the bulk heat capacity of the sample did not change dramatically between first and second heating.

Samples were analyzed by XRD to determine the phase makeup after the heating cycle. To gain insight into the reaction process, some material was recovered after heating to intermediate temperatures, and subsequently subjected to the same phase analysis procedure. The XRD patterns were processed using the GSAS whole pattern fitting software package [45].

In addition to thermal analysis, a preliminary investigation of ignition at high heating rates in the range 10^2-10^4 K/s was conducted. The reactive powder was coated on an electrically heated Nichrome filament. The temperature of the filament was monitored with an infrared pyrometer. Light emission from the powder coating was detected by a photodiode. A sharp onset of the light emission was taken as evidence of ignition. The setup is illustrated in Figure 2.3; in Chapter 2 (Section 2.4.4). The relation of thermal analysis and filament ignition experiments will be discussed further below.

3.3 Results

The result of the thermal analysis is shown in Figure 3.2 for several heating rates. The traces shown were baseline-corrected by subtracting the DSC signal recorded for the second heating of the same sample. The thermite reaction proceeds over an extended temperature interval, between 400 and 1000 K. The DSC traces show a broad exothermic hump starting at low temperatures overlapped with at least three distinguishable peaks, as labeled in Figure 3.2 Qualitatively, these measurements are generally consistent with the reported DSC traces for mixed Al and MoO_3 nanopowders [50]. Note however that the broad exothermic hump was not observed for mixed nanopowders. Figure 3.2 shows that the shape of the signal and therefore the relative significance of individual component reactions changes as a function of the heating rate. As expected, the onset of the broad exothermic hump and apparent peaks shift to higher temperatures as the heating rate increases. XRD measurements for the samples heated to different temperatures show that as the temperature increases, the amounts of MoO_3 and Al decrease while increased amounts of MoO_2 and, at higher temperatures, Al_2MoO_6 form. Formation of amorphous or poorly crystalline Al_2O_3 polymorphs cannot be reliably identified directly from the XRD patterns. Evolution of the phases directly identified from the XRD whole pattern processing is illustrated in Figure 3.3. In general, there is reasonable correlation for the reaction progress between MoO_3 and Al determined independently from DSC and XRD measurements. However, the XRD results do not provide enough details to identify the reactions causing the exothermic peaks in the DSC traces. Additional details regarding the comparison of the XRD and DSC measurements for the Al-MoO_3 nanocomposite thermites are reported elsewhere [22].

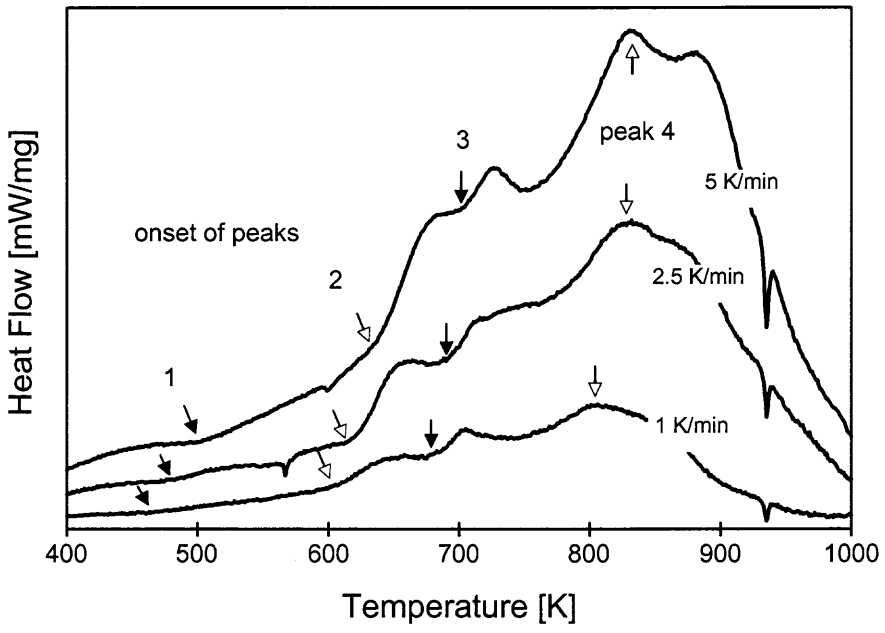

Figure 3.2 Observed DSC signal for the reaction of Al-MoO_3 nanothermite at various heating rates. The endothermic peak near 930 K indicates melting of residual aluminum.

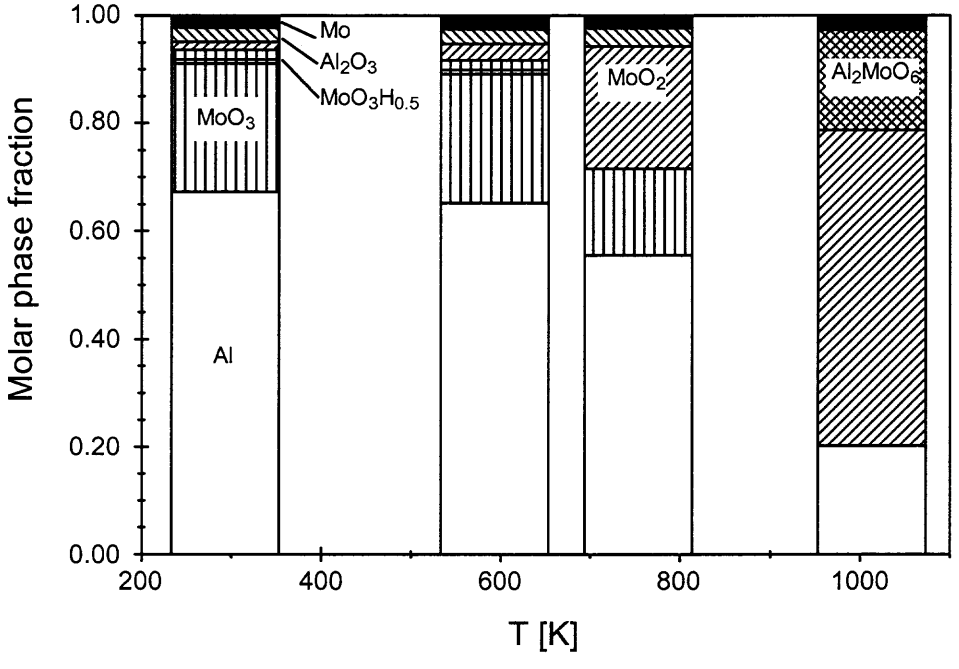

Figure 3.3 Concentrations of MoO_2, MoO_3, Al, Mo, and Al_2MoO_6 determined from the whole pattern processing of the XRD measurements for the stoichiometric nanocomposite powders of 2Al+MoO_3 heated to different temperatures.

Example results of the ignition experiments performed at different heating rates are shown in Figure 3.4. The photodiode signals are plotted versus the filament temperatures measured simultaneously. The heating rates were adjusted by varying the voltage applied to the filament and measured from the recorded pyrometer traces. The records of light emission from the igniting samples show very sharp onsets at the respective ignition temperatures. Like in the thermal analysis experiments, the ignition temperature increases with increasing heating rate.

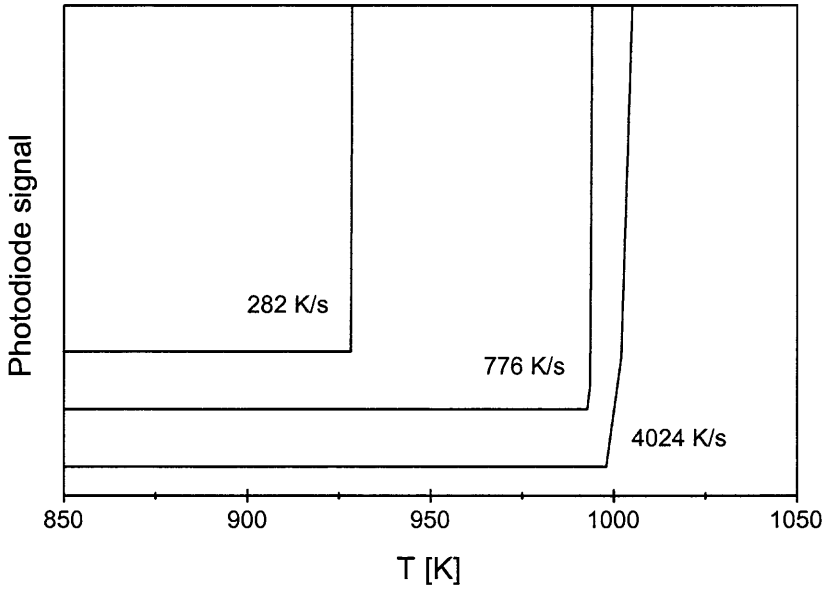

Figure 3.4 Results of the ignition experiments performed at different heating rates.

For initial evaluation, thermal analysis as well as ignition results were processed according to an isoconversion method after Kissinger [51]. Figure 3.5 shows the corresponding plot of $\ln(T^2/\beta)$ vs. the reciprocal temperature for ignition temperature as well as for traceable DSC peaks. In this formalism, β is the heating rate in K/s and the temperatures T are derived from thermal analysis at the onsets of exothermic peaks, and from the ignition experiments at the onset of the photodiode signal jump. The slopes of

these curves give an approximation of the respective activation energies of the underlying processes. Figure 3.5 shows that the ignition results do not line up directly with the thermal analysis. Therefore, a more detailed data processing is needed to establish the correlation between these two experiments and to identify the exothermic process (or processes) driving ignition in these materials.

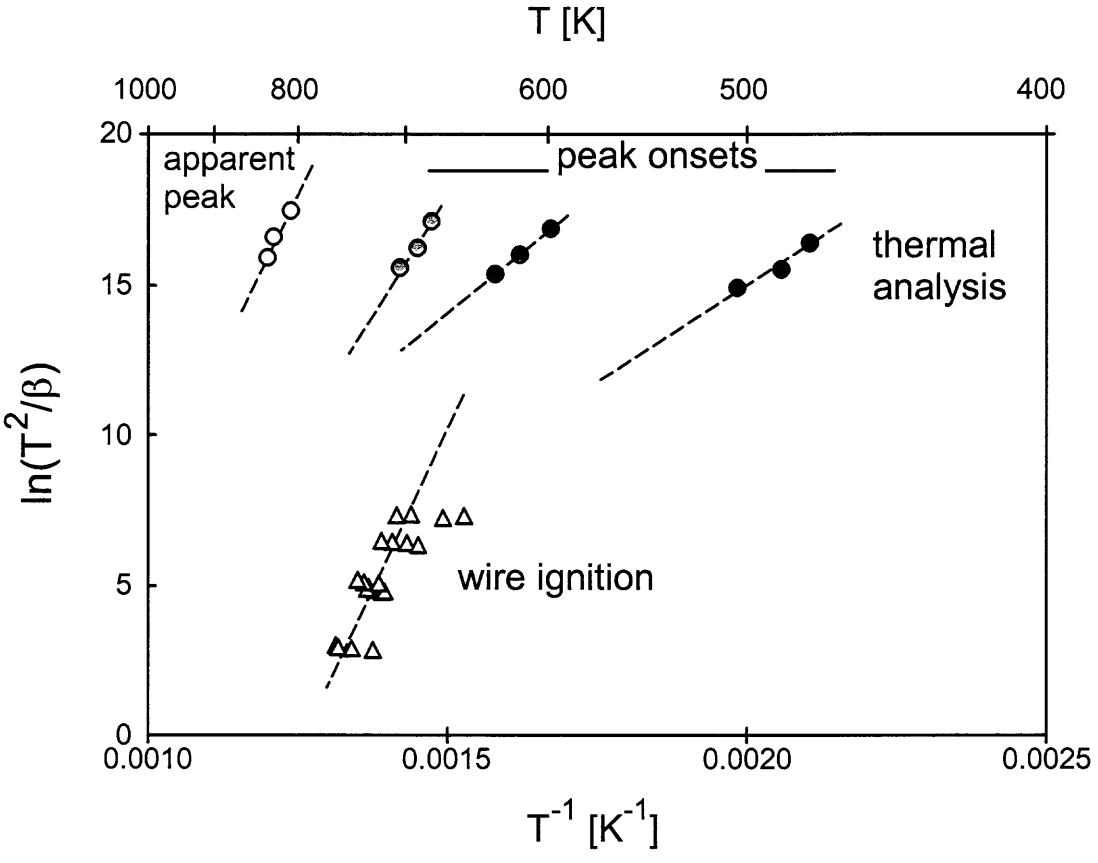

Figure 3.5 Isoconversion analysis of DCS and ignition data.

3.4 Data Processing

Since simple isoconversion processing did not lead to a meaningful relation between ignition and thermal analysis measurements, it was attempted to reconstruct the whole heat flow signal for the DSC measurement with the best resolution. Because activation

energy and frequency factor for each individual DSC peak are relatively strongly correlated, the results of this determination were used as initial estimates only; comparison with measurements at higher heating rates allowed tuning these values.

Before more detailed data processing can be applied, the following considerations should be taken into account. From concurrent and previous work [22] it was known that the nanocomposite is relatively inhomogeneous. That is, the as-milled material contains minor contaminants aside from the major constituents. Specifically, small but noticeable amounts of $MoO_{2.5}(OH)_{0.5}$ form as a result of milling. While its formation mechanism has not yet been unambiguously determined, it is possible that the strong mechanical activation of the milled Al causes the process control agent hexane to break down, forming poorly crystalline aluminum carbide phases while releasing hydrogen. This suggests the possibility that amorphous Al-C phases are also present in the as-milled material, although they have not been detected by either XRD or SEM investigations. Further, small amounts of MoO_3 have been reduced to form MoO_2 as well as some metallic Mo. Continued milling caused these phases to come in contact with all other phases, and as a result, a large variety of different interfaces were formed. Therefore, it was expected that the actual reactions can not usefully be modeled with traditional reaction mechanisms that were developed for reactions in homogeneous media [52]. Such mechanisms are based on the assumption that the reaction proceeds to a certain degree of completion (that is, by depletion of the reacting components). In the present case, the reaction may actually cease to proceed as a result of growing layers of reaction products, which represent significant diffusion barriers for further reaction although the

bulk composition of the sample may still have significant amounts of reactive components.

As a compromise, the observed peaks were modeled as follows: without detailed a-priori information about the reaction mechanism, the system was treated as undifferentiated. The entire range of the DSC measurement at 1 K/min (see Figure 3.2) was divided according to the apparent individual peaks. As the simplest assumption, the observed exothermic peaks were assumed to be independent of one another. All reactions were modeled according to the equation

$$\Phi(T) = Q/\beta \cdot Ae^{-\frac{E_A}{RT}} \cdot f(\alpha) \tag{3.1}$$

where Φ is the heat flow measured by the DSC, $\Phi=dQ/dt$, Q is the heat of the reaction, β the heating rate dT/dt, A is the frequency factor, E_A is the activation energy, R is the universal gas constant and T is the temperature. The reaction coordinate (nominal concentration of a reacting species) is given with α. The function $f(\alpha)$ refers to the specific kinetic law describing the reaction. The heat of reaction Q was partitioned between the four individual peaks so that

$$\sum_{i=1}^{4} Q_i = Q_{total} \tag{3.2}$$

Q_{total} was determined from the integral over the whole DSC trace between initial and final baselines. The requirement for a useful estimate of the reaction heat dictated the choice of the measurement at 1 K/min because measurements at other heating rates did not result in a final baseline. Integration of these measurements was therefore ambiguous.

The selection of the kinetic law defining the function $f(\alpha)$ is difficult and implies prescribing a specific reaction mechanism. In the most simplified approach, a first order

reactions, $f(\alpha) = \alpha$ can be assumed. More complicated reaction kinetics could be evaluated when the first order reaction does not describe the experiments satisfactorily. Thus, the following descriptions were selected for different exothermic peaks. The broad exothermic hump could not be described by the simple power order reaction and was modeled instead as a reaction controlled by three-dimensional diffusion as described by the Jander equation [52]

$$f_1(\alpha) = 1.5\alpha^{1/3}\left(\alpha^{-1/3} - 1\right)^{-1} \tag{3.3}$$

The remaining sharper peaks were successfully modeled as first-order reactions:

$$f_i(\alpha) = \alpha \quad \text{where } i = 2,3,4 \tag{3.4}$$

To obtain the kinetic parameters A and E_A, the model was fit to the measurement at 1 K/min using the Netzsch Thermokinetics software package [53]. The restriction to the measurement at 1 K was necessary as the measurements at higher heating rates did not result in unambiguous final baselines, and could therefore not be used for strict data fitting. Since, however, fitting a single measurement may lead to ambiguous results [54], the activation energies and frequency factors for the three sharper peaks were estimated based on the observed shift in the measurements at 2.5 and 5 K/min. Figure 3.6 shows the experimental data together with the individually modeled peaks as well as the sum of the modeled peaks.

While this approach is obviously a simplification, it does allow evaluating the reactions at heating rates outside the range covered by thermal analysis. Therefore, once a reasonable description of the DSC traces at different heating rates is achieved, the same model can be used to describe ignition. Furthermore, because kinetics for each exothermic peak is determined it becomes possible to compare the respective activation

energies to those of the known processes occurring in the specific materials system. For the Al-MoO_3 nanocomposite, related processes are the decomposition of MoO_3 and MoO_2 and diffusion of ions of O and Al through the MoO_2 and Al_2O_3 layers. Finally, it can be possible to identify one or more processes that directly control the ignition kinetics.

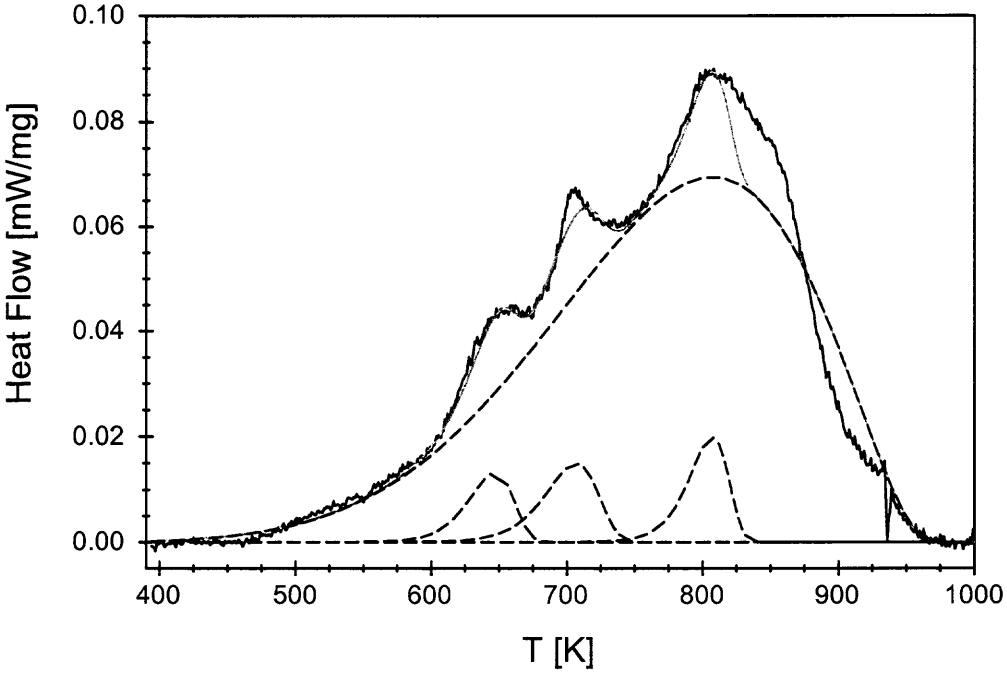

Figure 3.6 Comparison of experimental data with model curves for heating rate of 1 K/min. The dotted lines indicate individual modeled peaks whereas the light and dark solid lines represent modeled and experimental DSC trace.

3.5 Reaction Kinetics

To validate the calculations, the kinetic parameters were used to calculate peak positions at the highest heating rate used in thermal analysis experiments. This comparison is shown in Figure 3.7. The model does not reproduce the details of the measurement; however the peak positions coincide approximately. The kinetic parameters (frequency

factors and activation energies) are shown in Table 3.1. Projection of the model calculations to much higher heating rates is shown in Figure 3.8.

Table 3.1 Activation Energies and Frequency Factors for Individual Exothermic Peaks Observed in the DSC Traces for the Stoichiometric $2Al+MoO_3$ Nanocomposite Powder

Peak number and description	Temperature range of onset	Reaction type	E_A [kJ/mol]	log(A [s^{-1}])
1: Broad exothermic hump	470 - 510 K	3D diffusion, Jander type	90	1.2
2: Exothermic peak	590 - 640 K	1st order	209	13.9
3: Exothermic peak	670 - 710 K	1st order	211	12.5
4: Exothermic peak	800 - 840 K	1st order	373	21.2

These calculations were compared with results of filament ignition experiments. The calculated heat flow curves were processed according to the isoconversion method after Ozawa, Flynn and Wall [55], where the temperature at a constant reaction progress, $T=f(\alpha)$, is evaluated at varying heating rates β. The slope of $\ln(\beta)$ vs. 1/T gives the activation energy of the rate controlling process at temperature T and heating rate β.

$$\ln(\beta) = const. - E_A/RT \tag{3.5}$$

Analogous to the experimental curves, α was determined by integrating the calculated heat flow curves according to Eq. (3.2). Temperatures were determined for values of α in the range of 0.001 %, to 0.1 %. Figure 3.9 shows the results of this calculation in relation to both, experimental ignition temperatures as well as the onset of the DSC signal. The slope of the curves is similar to the ignition data points at high

heating rate, while it resembles the onset of the initial reaction in the thermal analysis experiments with a low activation energy.

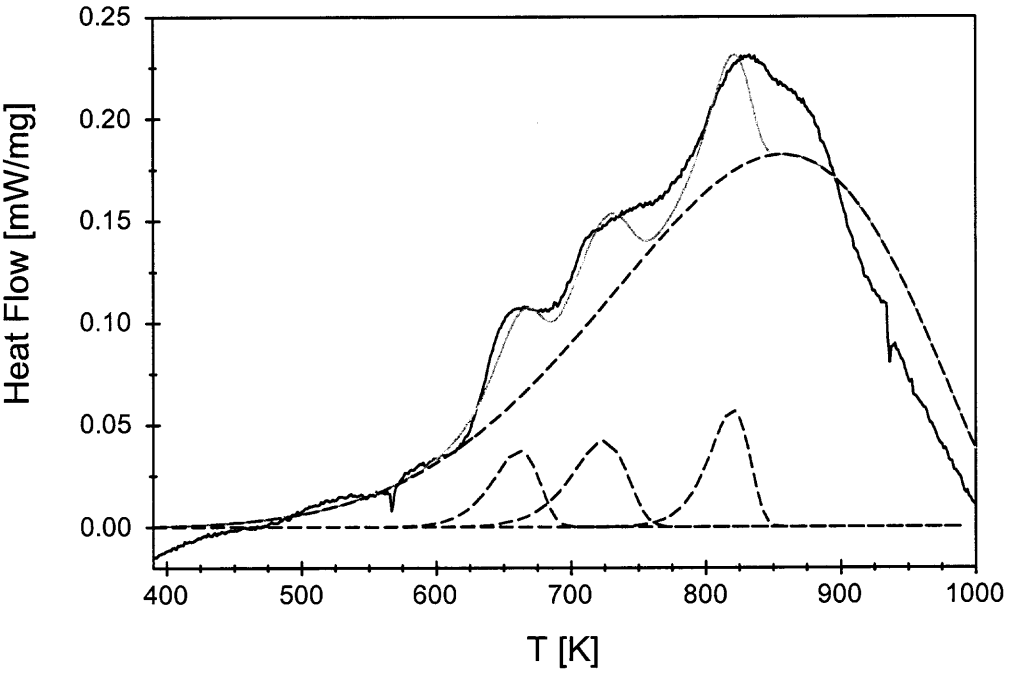

Figure 3.7 Comparison of experimental data with model curves projected to heating rate of 2.5 K/min. The dotted lines indicate individual modeled peaks whereas the light and dark solid lines represent modeled and experimental DSC trace.

An exact match was not obtained, but it was also not expected given the approximate nature of the presented analysis. Based on Figures 3.8 and 3.9, it can be concluded that the ignition of the stoichiometric $2Al+MoO_3$ nanocomposite powders is primarily driven by the low-activation energy process responsible for the onset of the broad exothermic hump in the DSC signal starting at low temperatures. At the same time, the processes causing sharper second and third exothermic peaks observed at higher temperatures play only a secondary role when the samples are heated rapidly. Finally, the high activation energy process causing the fourth and strongest exothermic peak

observed in the DSC traces almost does not affect ignition occurring at higher heating rates.

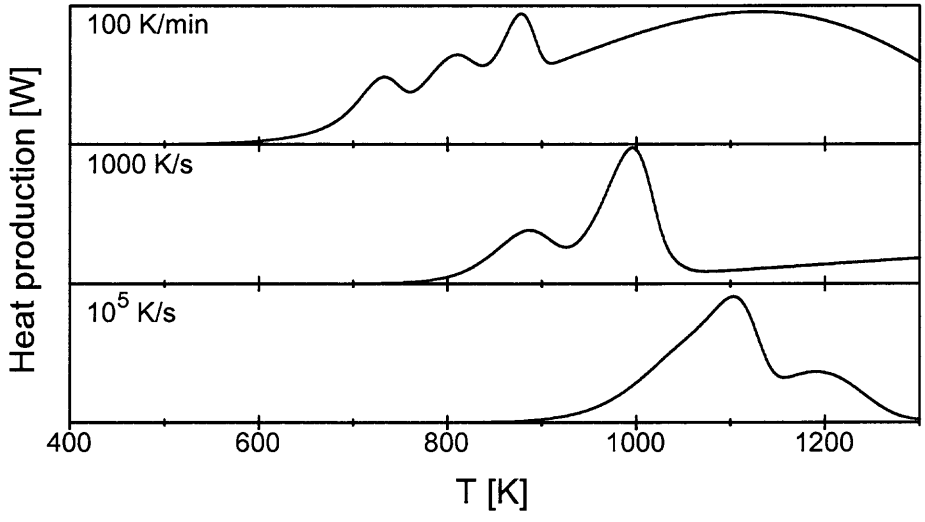

Figure 3.8 Model curves projected outside the range of heating rates of thermal analysis.

A more detailed analysis of the ignition is now possible in which the reaction model comprising the superposition of the four processes described in Table 3.1 can be used for the quantitative heat transfer analysis of the heated powder. Different experimental configurations can be readily described. For the present ignition experiments using a heated filament, it will be taken into account that the temperatures recorded are not the temperature of the reactive composite, but the temperature of the filament substrate. Recently, a numerical scheme has been developed to describe the ignition of powder coated on a heated filament [49]. Application of the reaction model developed here to this ignition simulation will be subject of future work.

3.6 Discussion

The activation energies shown in Table 3.1 can be discussed in the context of elementary reactions in the Al-MoO_3 system. The activation energy of reduction of MoO_3 to form MoO_2 in a hydrogen atmosphere was determined as 34 kJ/mol (40 vol-% H_2), or 103 kJ/mol (5 vol-% H_2) [56]. The observed activation energy of the broad underlying exothermic hump is within this range, suggesting that MoO_3 reduction is the rate limiting step, at least at low temperatures. This explanation suggests that in nanothermites prepared as mixed powders the oxygen released as a result of such decomposition can readily escape. However, in dense composites as used in this study the released oxygen is contained within the condensed material and is therefore more likely to react with aluminum. This difference in the reaction process explains why the broad exothermic process observed here for the fully dense nanocomposite powders was not noticeable in the DSC traces presented in Ref [50], for the mixed nanopowders of Al and MoO_3.

The sharper and smaller peaks at higher temperatures are characterized by substantially higher activation energies, which are comparable to activation energies determined for aluminum oxidation [57]. The rates of Al oxidation depend on the surface coverage by various polymorphs of Al_2O_3 and are controlled by diffusion of ions of O and/or Al. Diffusion of oxygen through a surface layer of γ-alumina was characterized by an activation energy of 220 kJ/mol [57]. Similarly, a recent experimental study of Al oxidation by Sun et al. determined an apparent activation energy of 240 ± 20 kJ/mol for Al oxidation [50]. Activation energies as high as 418 kJ/mol were also reported for Al oxidation, without identifying the specific alumina polymorph being formed [58]. Thus, the second, third, and fourth exothermic peaks (see Table 3.1) could reasonably be

assigned to reactions where rates are limited by diffusion through the growing alumina layer. The activation energies for the second and third peak are nearly the same, suggesting that both peaks could be caused by the diffusion through the same or similar polymorphs of Al_2O_3, most likely γ-alumina. The presence of two separate peaks could be explained by the existence of different interface morphologies where the γ-alumina (or related transition alumina) layers are being formed. The fourth peak with high activation energy is observed at higher temperatures, at which formation of the α-Al_2O_3 polymorph is likely, and formation of the ternary phase Al_2MoO_6 is observed from XRD.

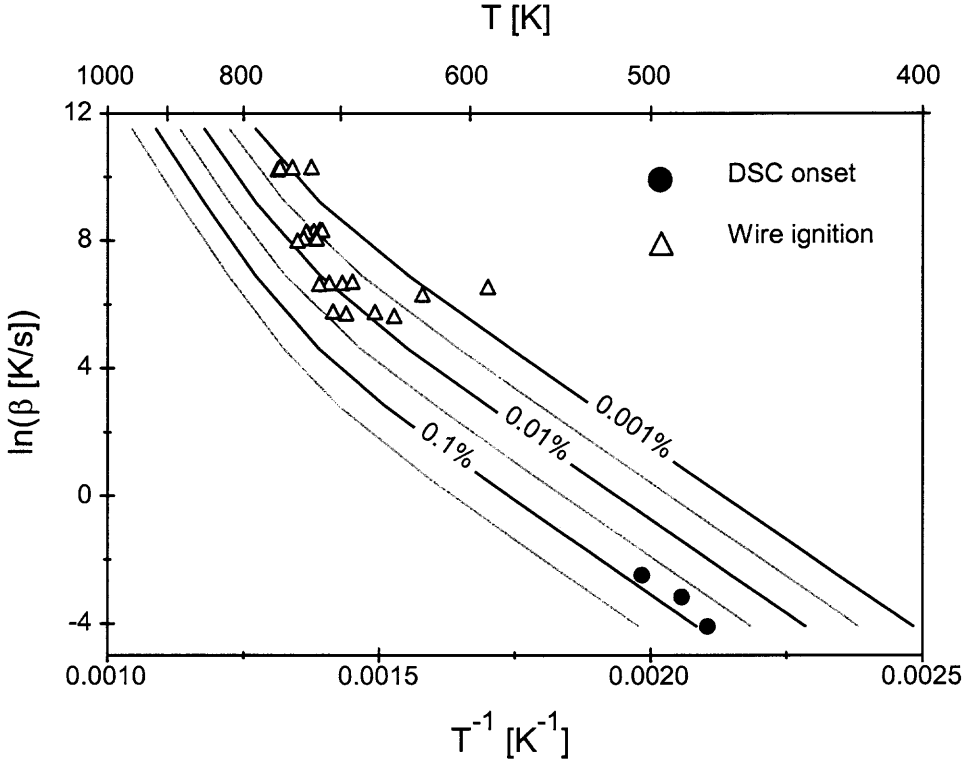

Figure 3.9 Preliminary comparison of ignition experiments at high heating rates and the onset of DSC curves at low heating rates with lines of constant reaction progress calculated according to the model calculations.

3.7 Summary And Conclusions

Reactions in stoichiometric $2Al+MoO_3$ nanocomposite thermite powders have been investigated using thermal analysis and heated filament ignition experiments. A preliminary reaction model was fit to the experimental data. The reaction model is the superposition of four reaction steps assumed to be independent. The comparison of the activation energies determined for the reaction steps observed in this study with activation energies reported earlier for elementary reactions in the $Al-MoO_3$ system suggests that the first, low-activation energy reaction is associated with decomposition of MoO_3 while following reaction steps are controlled by the diffusion through growing layers of Al_2O_3. Preliminary comparison with ignition experiments suggest that a relatively small heat release at the onset of the exothermic reaction causes ignition at high heating rates. The proposed reaction model can be combined with a detailed heat transfer analysis for a specific experimental situation. Therefore, quantitative description of the ignition kinetics and identification of the specific reaction mechanism driving ignition for each specific experiment will become possible.

CHAPTER 4

EXOTHERMIC REACTIONS IN Al-CuO NANOCOMPOSITES

4.1 Introduction

Among several types of reactive nanocomposites synthesized by ARM [18-22], Al-CuO thermites are of particular interest. The reaction is highly exothermic and its temperature can be adjusted to produce either molten or vapor-phase copper. Thus, a broad range of potential applications is possible including joining compounds and energetic compositions enabling transient gas generation. Recently, Al-CuO_x multilayer nanofoils were produced and characterized [15, 16]. Differential thermal analysis traces of these nanofoils when heated from ambient conditions to 1673 K indicated that the reaction proceeded via two separate exotherms occurring around 850-950 K and 975-1275 K. These events were interpreted as reactions controlled by lateral growth of Al_2O_3 nuclei and then by diffusion of oxygen through growing Al_2O_3 layers, respectively. It was suggested that the oxygen diffusion through CuO_x layers was not a rate-limiting process for the observed reactions [16]. However, in our initial experiments with Al-CuO dense nanocomposite powders produced by ARM, exothermic events were observed to occur at much lower temperatures, starting from about 400 K [21]. Thus, the reaction mechanisms proposed in refs. [15, 16] need to be expanded and verified in order to be applied to a broader range of Al-CuO nanocomposites. The present work is aimed to develop a more adequate description of Al-CuO thermite reactions. Furthermore, the correlation of different processes occurring during such reactions and ignition of Al-CuO nanocomposites occurring at high heating rates was of interest. Differential scanning

calorimetry (DSC), X-ray diffraction (XRD) and heated filament ignition experiments [24] were used to quantify the ignition kinetics and related reaction mechanisms.

4.2 Experimental

4.2.1 Preparation of Nanocomposite Powders

A shaker mill (8000 series by Spex CertiPrep) was employed in this research. Flat-ended steel vials were used along with 5 mm steel balls. Starting blends were prepared in stoichiometric proportions from powders of elemental aluminum (99% pure, -325 mesh by Atlantic Equipment Engineers) and cupric oxide CuO (99% pure, 1-5 micron, by Atlantic Equipment Engineers). Synthesis was carried out in argon environment. A small amount of hexane (C_6H_{14}) was added as a process control agent (PCA) to hinder the cold welding during milling. The process temperature was monitored using thermistors attached to the sides of the milling vials and connected to a digital data logger. The instant of reaction was marked by a sharp rise in the vial temperature. Highly metastable energetic nano-composites were prepared by arresting the milling before the spontaneous exothermic reaction. When the amount of PCA added to the mixture was varied, the milling times required to initiate the reaction changed. Three different samples were prepared by varying both the amount of PCA and the milling times, as shown in Table 4.1. When the materials were milled without any PCA, the reaction occurred within 2 min. When 1 ml of hexane was added, the reaction was triggered after 16 minutes of milling. When 8 ml of hexane was added, the reaction did not initiate even after an hour of milling and the metastable samples were prepared by stopping milling after 60 minutes.

Table 4.1 Nanocomposite Powder Samples Prepared and Used in this Research

Sample ID	Hexane, ml	Milling time, min
1	0	2
2	1	16
3	8	60

* batch mass 3 g; ball to powder mass ratio 5, 5 mm steel balls

4.2.2 Sample Characterization

Morphology and composition of the composites were examined on a LEO 1530 Field Emission Scanning Electron Microscope (SEM) operated at 10 kV. The samples were embedded in epoxy and cross-sectioned for examination. The phase composition was determined for each sample by x-ray diffraction (XRD). The XRD was performed on a Phillips X'pert MRD powder diffractometer operated at 45 kV and 40 mA using Cu Kα radiation (λ = 1.5438 Å). Temperature-dependent structural transformations were determined by differential scanning calorimetry (DSC) using a Netzsch Simultaneous Thermal Analyzer STA409 PC. Alumina pans were used and the furnace was flushed with argon at approximately 10 ml/min. DSC traces were recorded between room temperature and 1013 K with heating rates varying from 5 to 40 K/min. The temperature is accurate within ±1 K.

4.2.3 Ignition Experiment

In addition to thermal analysis, a preliminary investigation of ignition at high heating rates in the range 10^2-10^4 K/s was conducted. The reactive powder was coated on an electrically heated Nichrome filament. The temperature of the filament was monitored with an infrared pyrometer. Light emission from the powder coating was detected by a

photodiode. A sharp onset of the light emission was taken as evidence of ignition. The setup is illustrated in Figure 2.3; in Chapter 2 (Section 2.4.4).

4.3 Results

4.3.1 SEM Analysis

Figure 4.1 shows SEM images of the cross-sections of the starting powder mixture and Al-CuO composites synthesized after ~ 2, 16 and 60 min of milling. These images are produced using backscattered electrons and show phase contrast between Al and CuO-rich phases. It can be observed that the particle size decreases and morphology of the powder changes with increasing milling times. For the starting mixture, (Figure 4.1A) the bright CuO particles are well distinguished from gray Al and the dark epoxy background. After 2 min of dry milling (sample 1), the Al particles are flattened as shown in Figure 4.1 B. The CuO particles are reduced in size and embedded in aluminum. Very large, dense agglomerates are formed. Most of the CuO particles are close to the surface of aluminum and located on or between the ductile aluminum layers. After 16 min of milling with 1 ml of hexane added (Figure 4.1 C, sample 2), the particle sizes of Al and CuO reduce drastically and some of the CuO particles become embedded in the Al matrix. However, unmixed particles of Al and CuO are still present. The particle sizes vary widely. The mixing appears to be non-homogeneous throughout the sample. Groups of relatively coarse particles of Al and CuO representing loose agglomerates are visible in Figure 4.1 C. At the same time, some particles with a much finer mixing of components are also present. Figure 4.1 D shows that the increase in the milling time to 60 min, possible when 8 ml of hexane was added, resulted in further reduction of the

particle sizes and in a more homogeneous mixing. Figure 4 shows an image of the same sample as shown in Figure 4.1 D but at a higher magnification. Most of the particles are nanocomposites of CuO inclusions in the aluminum matrix. Fine mixing of Al and CuO particles has been achieved. At the same time, several very bright and homogeneous particles are visible. A close inspection shows presence of small spherical voids inside such bright particles, which are identified as copper. Therefore, at the extended milling time and large amounts of the PCA used, the thermite reaction occurred locally, but did not propagate through the entire sample. This suggestion is further confirmed by XRD as described below.

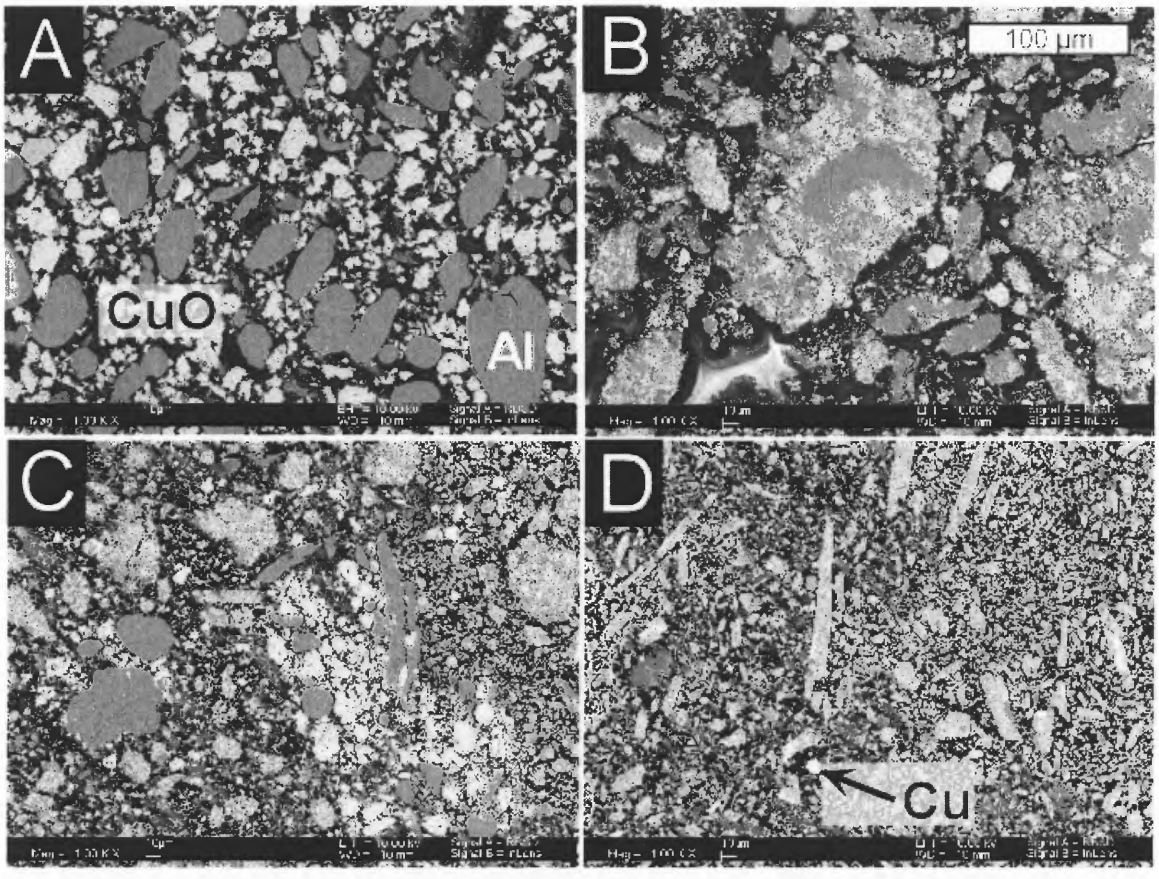

Figure 4.1 Backscattered electron SEM images of the cross-sectioned Al-CuO samples embedded in epoxy: A. Starting material; B. Sample 1; C. Sample 2; D. Sample 3. The magnification is the same for all the images and is illustrated by the scale bar in the image B.

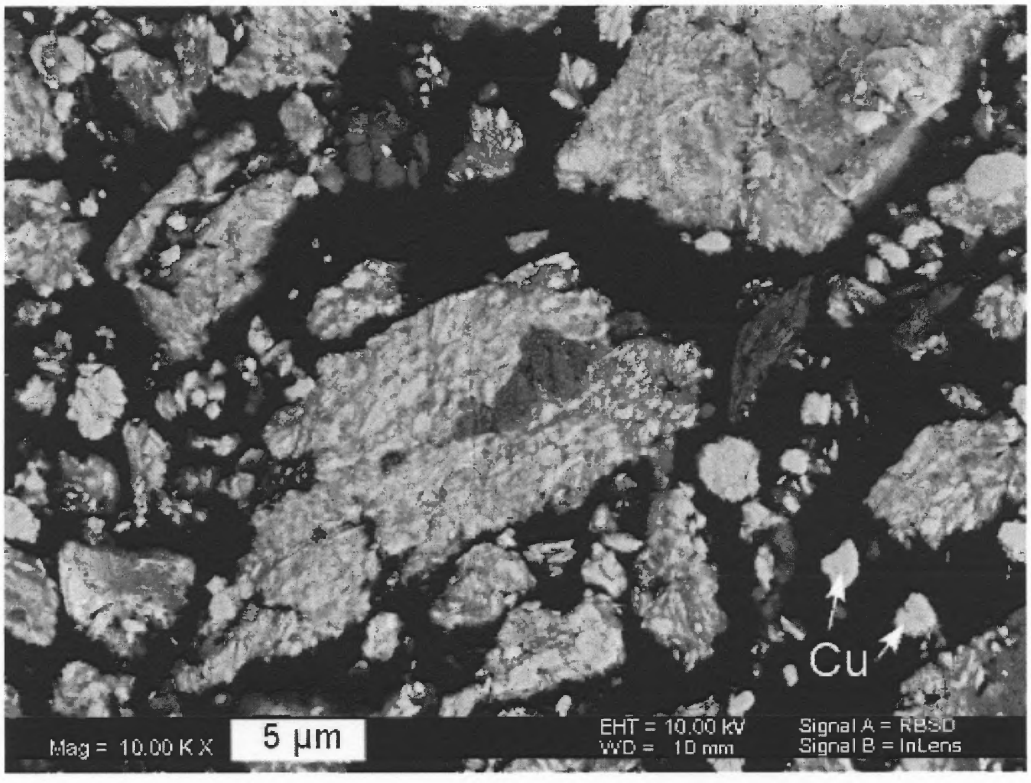

Figure 4.2 High magnification SEM image of cross-sectioned sample 3 embedded in epoxy.

4.3.2 X-ray Analysis

Figure 4.3.a shows the X-ray diffraction patterns for the samples 1, 2, and 3. Figure 4.3.b shows the crystallite size of aluminum as a function of milling time. As seen earlier in Table 4.1, addition of hexane enables increased milling time. As an overall trend, the increased milling times result in the decreased intensity of Al and CuO peaks. The XRD pattern of sample 1 shows only peaks of starting materials, Al and CuO. The XRD pattern of sample 2 indicates additional presence of Cu and small amounts of Cu_2O. These peaks arise due to the localized partial reaction that occurs during milling.

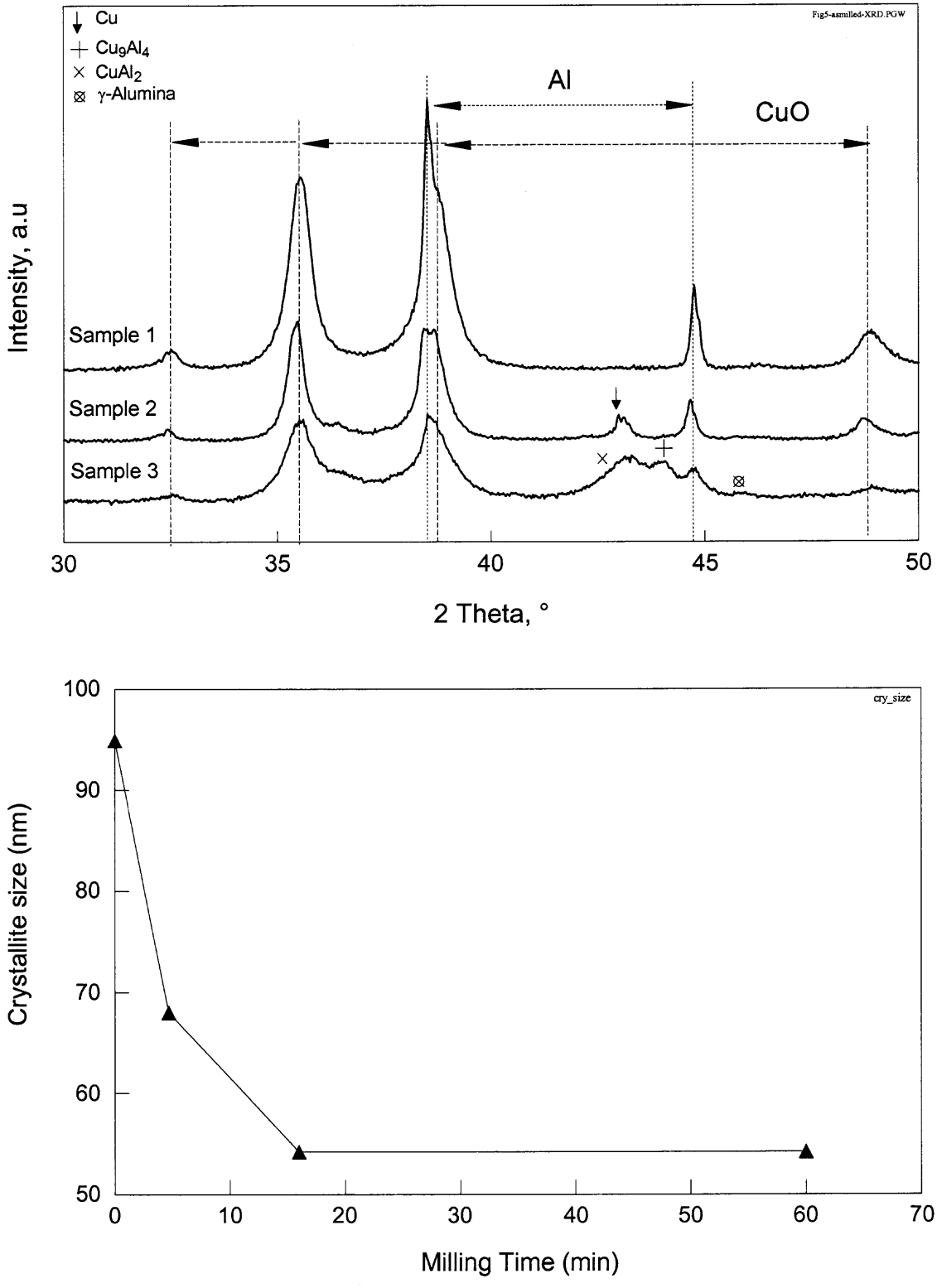

Figure 4.3 a). X-ray diffraction patterns of composite samples 1, 2, and 3 prepared at different milling times (cf. Table 4.1). b). Crystallite size of aluminum as a function of milling time.

Amorphous or poorly crystalline Al_2O_3 polymorphs are also likely to be produced in this reaction, but are not detected from XRD. Extended milling time (60 min) for sample 3 gives rise to $CuAl_2$, γ-alumina and Cu_9Al_4 in addition to Al, CuO, Cu and Cu_2O peaks.

Increase in the milling time also leads to broadening of peaks as a result of decrease in the crystallite size of both Al and CuO. SEM and XRD results indicated that sample 1 consisted of unmixed particles of the starting material. Hence the ignition experiments and thermal analysis measurements were limited to samples 2 and 3 in which nanocomposite structures were formed. The average crystallite size of each sample was estimated by whole pattern refinement of the XRD patterns using the GSAS software (Generalized Structural Analysis System) [45]. It was observed that increase in milling time results in the decrease in the crystallite size of aluminum.

4.3.3 Ignition

Figure 4.4 shows the ignition temperatures of the Al-CuO nanocomposites as a function of heating rate. The filament ignition experiments were performed in air at three different heating rates varying in the range of 10^4- 10^6 K/min (10^3 – 10^4 K/s). In general it is observed that the ignition temperatures of the Al-CuO nanocomposites increase with increasing heating rates as is expected for a thermally activated ignition mechanism. It is also clear that ignition temperatures measured for sample 2 are higher than for sample 3. A decrease in the ignition temperature for sample 3 can be attributed to a higher degree of structural refinement achieved at a longer milling time with a greater quantity of liquid process control agent.

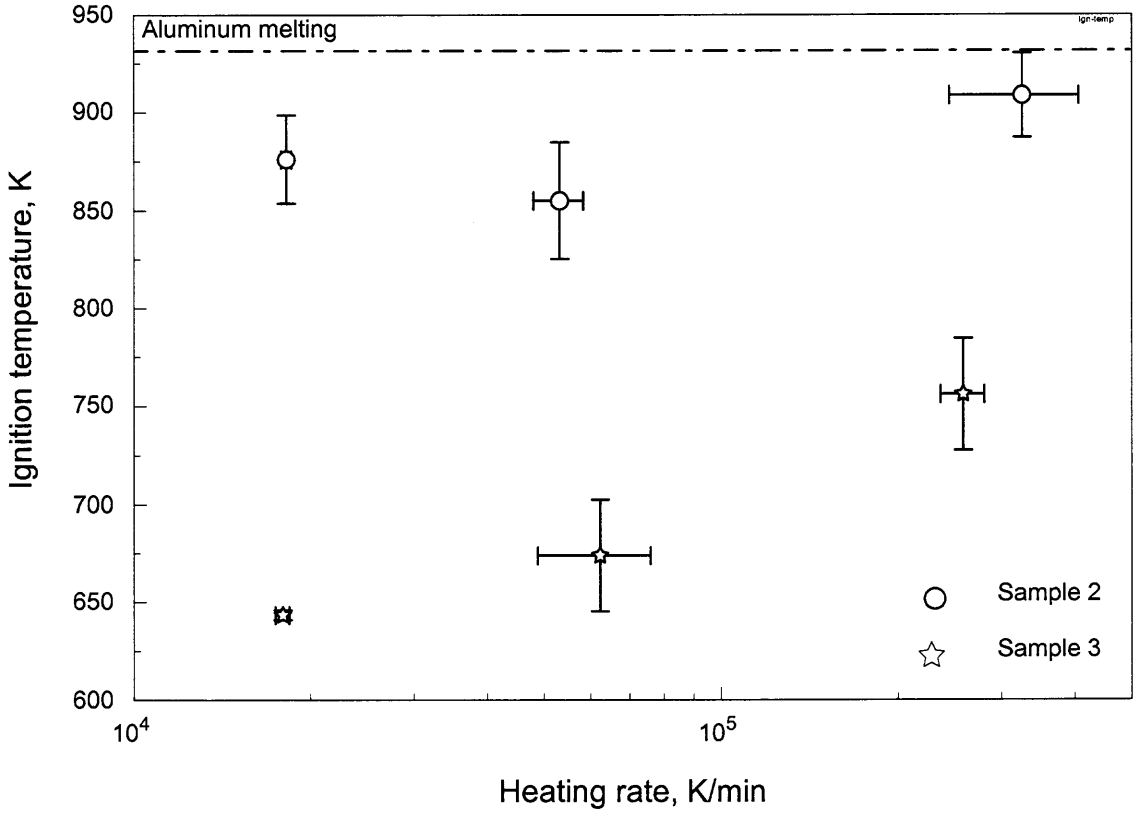

Figure 4.4 Ignition temperatures measured for samples 2 and 3 at different heating rates. The error bars represent the standard deviations from multiple measurements.

4.4 Thermal Analysis

Thermal analysis was performed in both argon and oxygen environments for several heating rates. Figure 4.5 shows the DSC traces of samples 2 and 3 collected at 5, 20 and 40 K/min in argon. The traces shown were baseline-corrected by subtracting the signal recorded during the second heating of the same sample. Heating of sample 2 from room temperature to 1013 K was accompanied by a broad and very weak exothermic event between 350 and 800 K. In addition, a strong exothermic peak was observed between 825 and 930 K. A weak endothermic peak corresponding to aluminum melting was observed around 933 K.

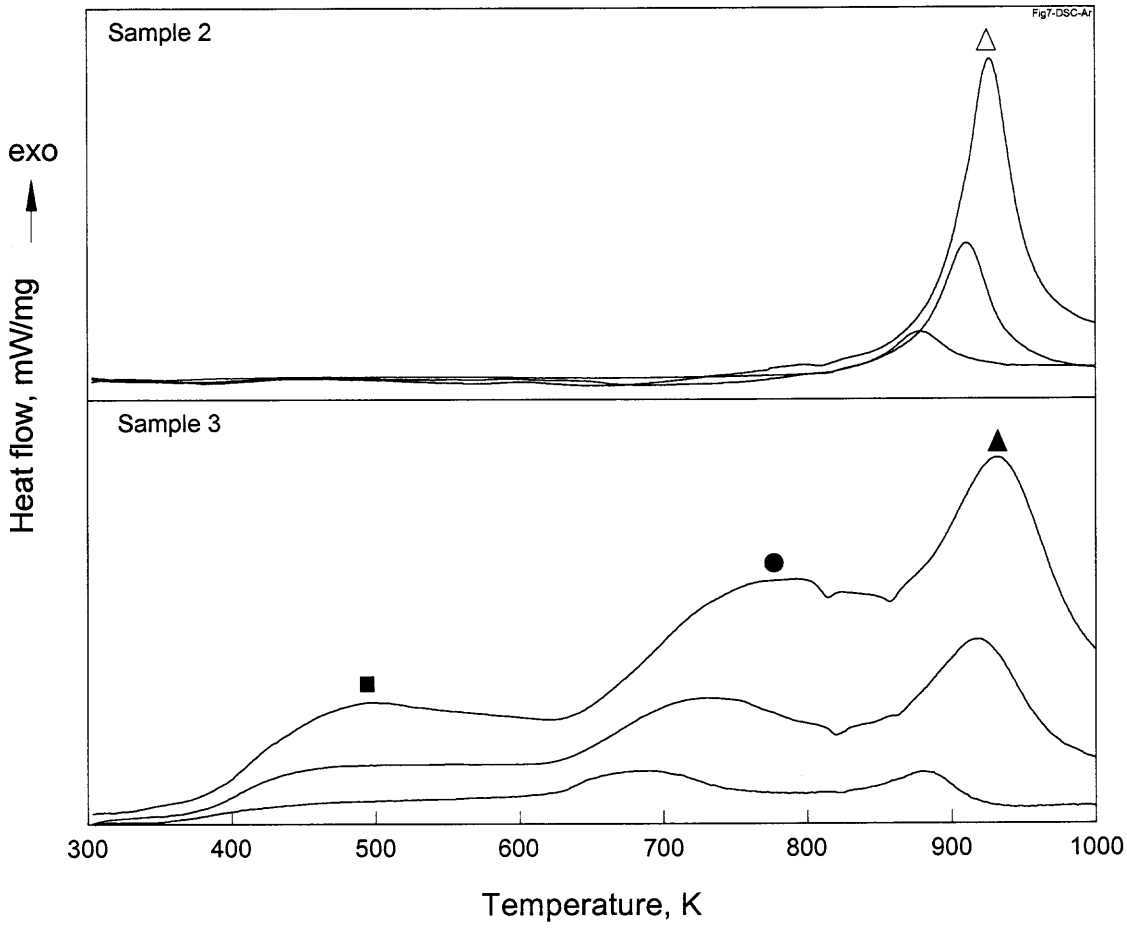

Figure 4.5 DSC traces of samples 2 and 3, recorded in argon at the heating rates of 5, 20 and 40 K/min respectively. Symbols are used to identify the exothermic peaks.

The DSC trace of sample 3 is characterized by a series of at least three overlapping exothermic events, including the low temperature events that were not observed for sample 2. The first, broad exothermic event was observed between 350 and 600 K. It was followed by a strong exothermic event between 600 and 800 K. The third exothermic event occurred between 825 and 930 K and was similar to the exothermic peak observed for sample 2 in the same temperature range. In addition to the aluminum-

melting peak, endothermic peaks were observed around 820 and 860 K, corresponding to the melting of $CuAl_2$ and Cu_9Al_4, respectively [59].

To identify processes occurring during the exothermic events, XRD patterns were collected from powders obtained by quenching sample 3 heated to intermediate temperatures bracketing each event. The sample was quenched by interrupting the power to the DSC furnace, achieving effective cooling of 300-500 K over a period of 10-15 minutes. Figure 4.6 shows the respective XRD patterns.

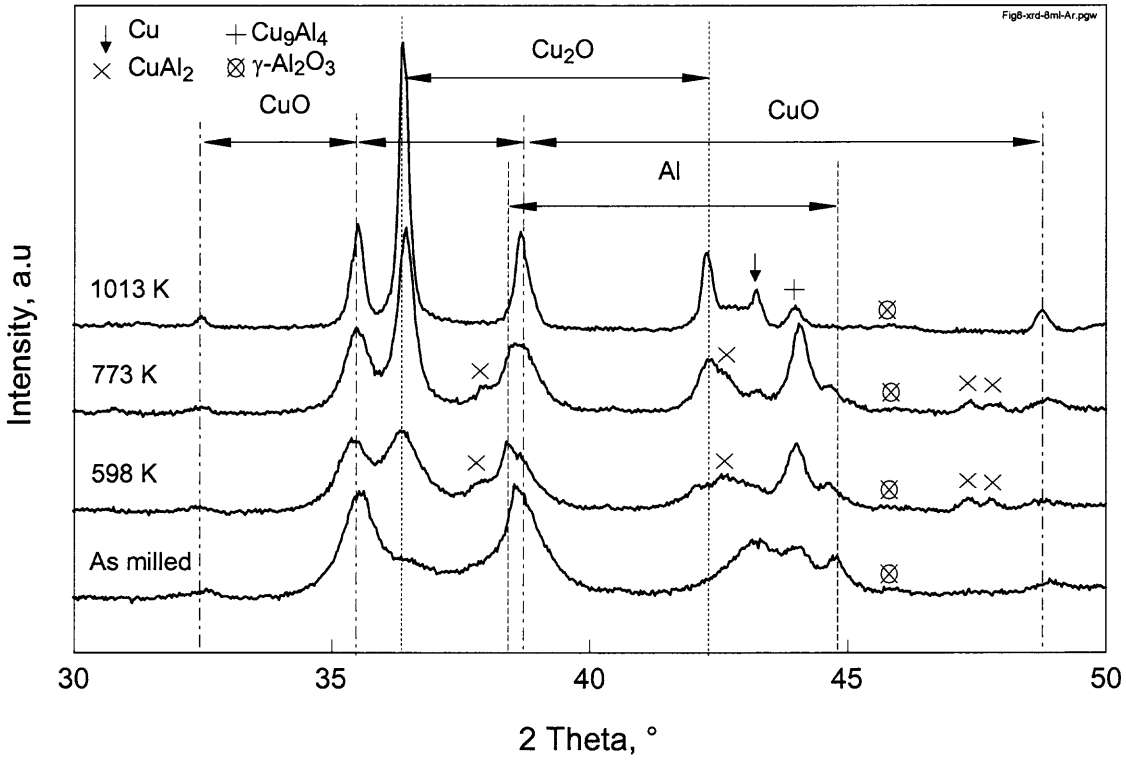

Figure 4.6 XRD patterns of the powders produced by heating sample 3 in argon to and quenching at the temperatures bracketing exothermic events observed in DSC traces (Figure 4.5).

The XRD pattern of the as-milled material is shown in Figure 4.6 for reference as well, and it is identical to that shown in Figure 4.3 for sample 3. As a general trend, the peak intensities for starting materials Al and CuO, decrease, whereas the peak intensities

of the reaction products, e.g., Cu_2O, $CuAl_2$, Cu_9Al_4 and γ-Al_2O_3 increase at higher temperatures.

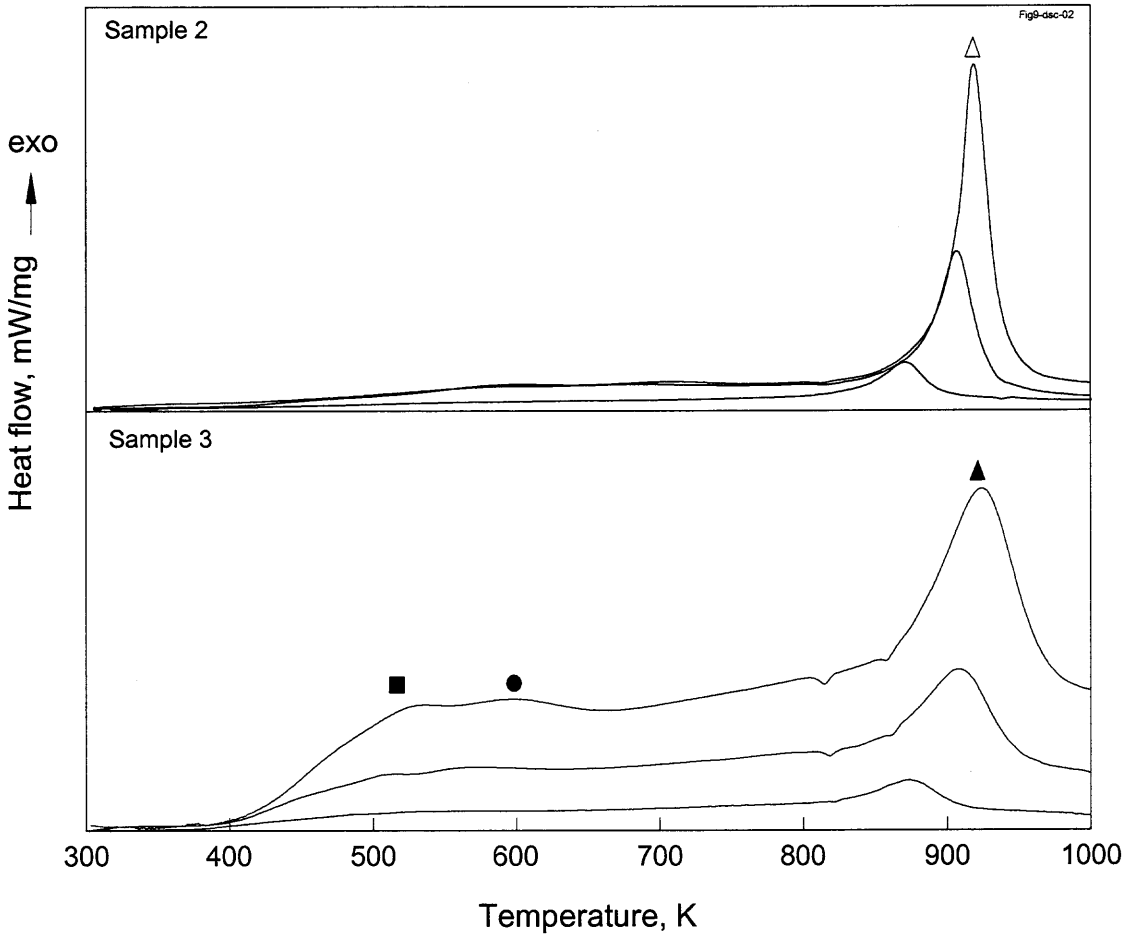

Figure 4.7 DSC traces of samples 2 and 3, recorded in oxygen at the heating rates of 5, 20 and 40 K/min respectively. Symbols are used to identify the exothermic peaks.

The main effect observed for the sample heated to 598 K, is a substantial increase in intensity of the Cu_2O peaks. This increase continues throughout the heating. The peaks of intermetallic phases, $CuAl_2$, Cu_9Al_4 become fairly strong at 598 and 773 K, but almost disappear at a higher temperature. The intensity of peaks corresponding to both Cu_2O and Cu increases considerably at 1013 K. It was also observed that the peaks

become narrow as the temperature increases, which implies that crystallite sizes of the materials increase.

Figure 4.7 shows the DSC traces of samples 2 and 3 heated at 5, 20 and 40 K/min in oxygen. The traces shown were baseline-corrected by subtracting the signals recorded during the second heating of the same sample. DSC traces generally similar to those recorded for the same samples heated in argon, as shown in Figure 4.5. However, the positions of the low-temperature exothermic events observed for sample 3 in oxygen are slightly shifted compared to those in argon.

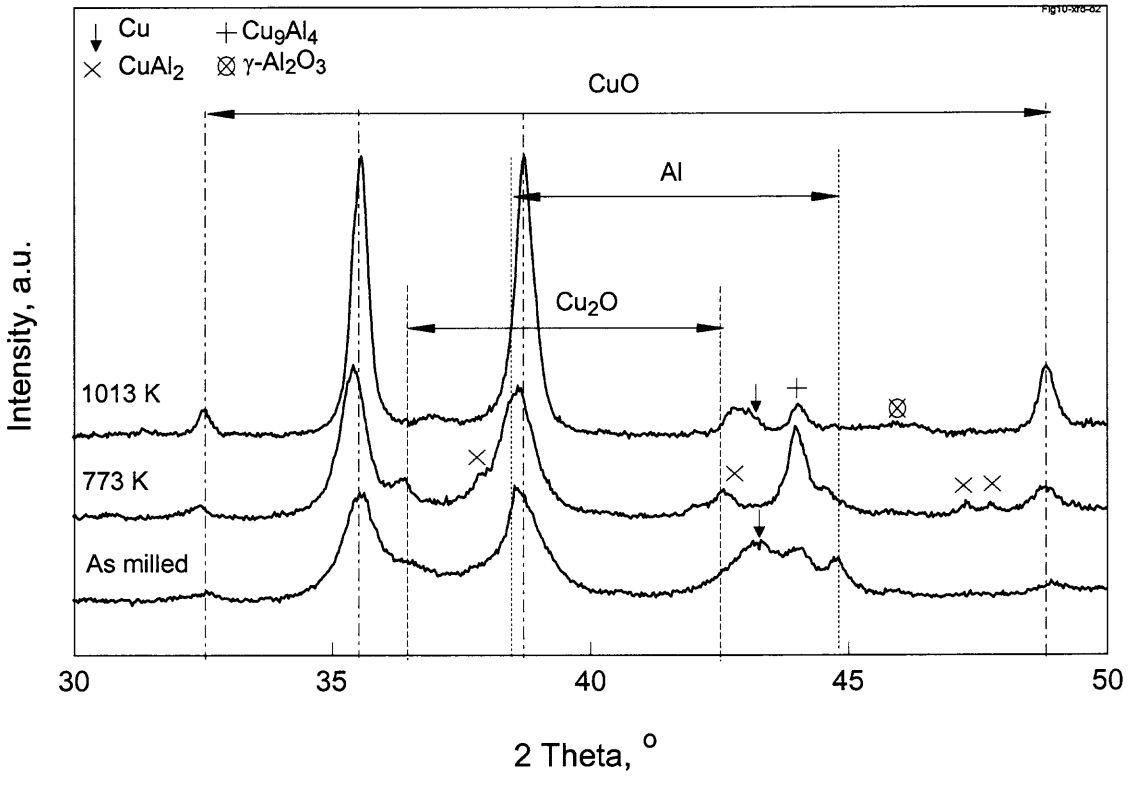

Figure 4.8 XRD patterns of the powders produced by heating sample 3 in oxygen to and quenching at the temperatures bracketing exothermic events observed in DSC traces (Figure 4.7).

Similar to the treatment described above for the samples heated in argon, the powders produced by heating sample 3 in oxygen and quenching at several intermediate temperatures were collected and analyzed by XRD. Figure 4.8 shows the respective XRD patterns. Unlike results shown in Figure 4.6, the peak intensity of CuO increases at increased temperatures, while the peak intensity of Al decreases as in Figure 4.6. Only a small increase in the peak intensity for Cu_2O at 773 K is observed followed by a decrease at 1013 K. Similar to results shown in Figure 4.6, the intensity of the peaks of intermetallic phases is at a maximum at the intermediate temperature of 773 K. Also similar to Figure 4.6, the peak intensity of Cu increases considerably at 1013 K and all the peaks become narrow at increased temperatures indicating an increase in the crystallite sizes.

4.4 Reaction Kinetics

The thermal analysis data were initially processed using an isoconversion method by Kissinger [51]. A plot of $\ln(\beta/T^2)$ vs. the reciprocal temperatures 1/T of the DSC peaks, where β is the heating rate in K/min, is shown in Figure 4.9. In addition, the results of the ignition temperature measurements are presented in the same coordinates, corresponding to a much higher range of heating rates. The slopes of the straight lines corresponding to each group of data points represent the values for the respective activation energies. Results of DSC experiments obtained for samples 2 and 3 in argon are shown in Figure 4.9. Table 4.2 summarizes the activation energies obtained by the Kissinger method for the exothermic peaks observed for both samples 2 and 3 heated in both argon and oxygen environments. Figure 4.9 shows that when the heating rates

approach the range of those used in ignition experiments, the stronger exothermic events (labeled as ▲ and ● in Figures 4.5 and 4.9) are expected to occur at much higher temperatures, as compared to the observed ignition temperatures. Note that the points representing the strong peak labeled as Δ, for sample 2, nearly coincide with the points representing the strong peak labeled as ▲ for sample 3. Note also that ignition of sample 2 occurs at temperatures that are weakly dependent on the heating rate and are very close to the melting point of Al (cf. Figure 4.4). The kinetics of the low-temperature, relatively weak and broad exothermic event labeled as ■, seems to project to a temperature range close to, but slightly lower than that observed for ignition of sample 3 (cf. Figure 4.9).

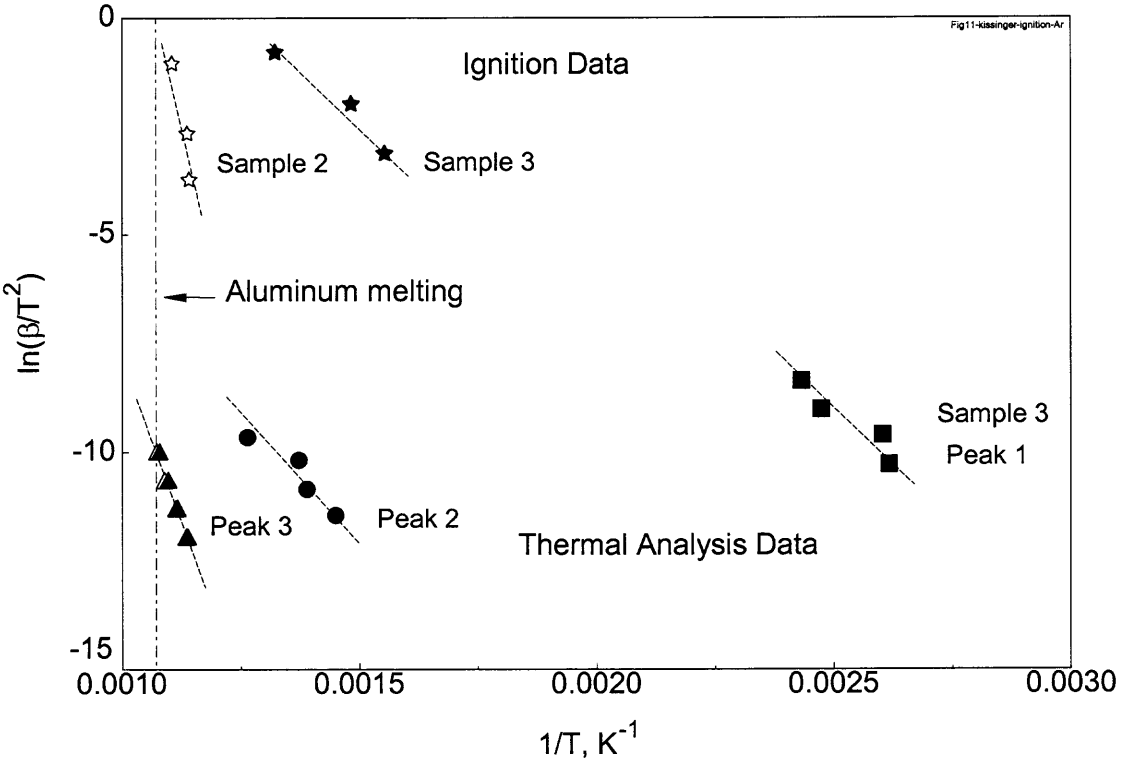

Figure 4.9 Comparison of ignition temperatures measured at different heating rates in air and exothermic peak positions observed in the DSC traces for sample 2 and 3 heated in argon. The hollow and solid symbols represent data for samples 2 and 3, respectively. The aluminum melting point is shown for reference.

Table 4.2 Activation Energies of Exothermic Peaks Observed in Argon and Oxygen for Sample 3 Calculated using Kissinger Method [51].

Sample ID	Exothermic peak description/ respective symbol in Figs. 7, & 9		E_A (KJ/mol) DSC Environment Argon	Oxygen
Sample 2	Strong peak	△	277	268
Sample 3	Broad peak	■	70	119
	Strong peak	●	80	91
	Strong peak	▲	260	259

The following discussion will be only related to sample 3, for which ignition occurred at lower temperatures and appeared to be most directly affected by low-temperature Al-CuO reactions of interest in this paper. Because of the higher level of refinement (cf. Figures. 4.1- 4.3), sample 3 best represented nanocomposite Al-CuO materials of interest to practical applications.

A useful correlation between the thermal analysis results and ignition experiments can only be established if the reaction kinetics representing the exothermic events observed in DSC are described quantitatively. As a first step to obtaining such a description, the DSC traces for sample 3 were processed to determine the activation energy as a function of reaction progress, α, according to the method after Ozawa [60], and Flynn and Wall [59]. This processing was based on evaluation of temperatures corresponding to a constant reaction progress observed at different heating rates. Calculations of the reaction progress involved measurements of partial areas under the DSC curves, which required detailed reconstruction of the temperature-dependent baselines. Because the temperature ranges used in the experiments were broad, the baselines were neither well-constrained, nor expected to be linear. This was confirmed

by initial estimates using straight-line baselines between start and end points of the DSC signal, which resulted in substantially different reaction progress corresponding to the positions of the same exothermic peaks at different heating rates. To reconstruct a more accurate temperature dependent baseline, it was assumed that the degree of conversion was the same for all heating rates when the 3rd, strongest peak occurred in the DSC signals. The initial and final slopes of the DSC curve recorded at 5 K/min were used to construct a smooth initial baseline for this measurement and determine the respective degree of conversion corresponding to the position of the 3rd peak. This degree of conversion corresponded to 90%, and it was used consistently to adjust the baseline representing the weighted averages of the initial and final slopes for other used heating rates.

Using the reconstructed baselines, the activation energy was calculated as a function of reaction progress as shown in Figure 4.10. The temperatures corresponding to the reaction progress of 20, 40, 60, and 90% for the heating rate of 5 K/min are also shown in Figure 4.10 for reference.

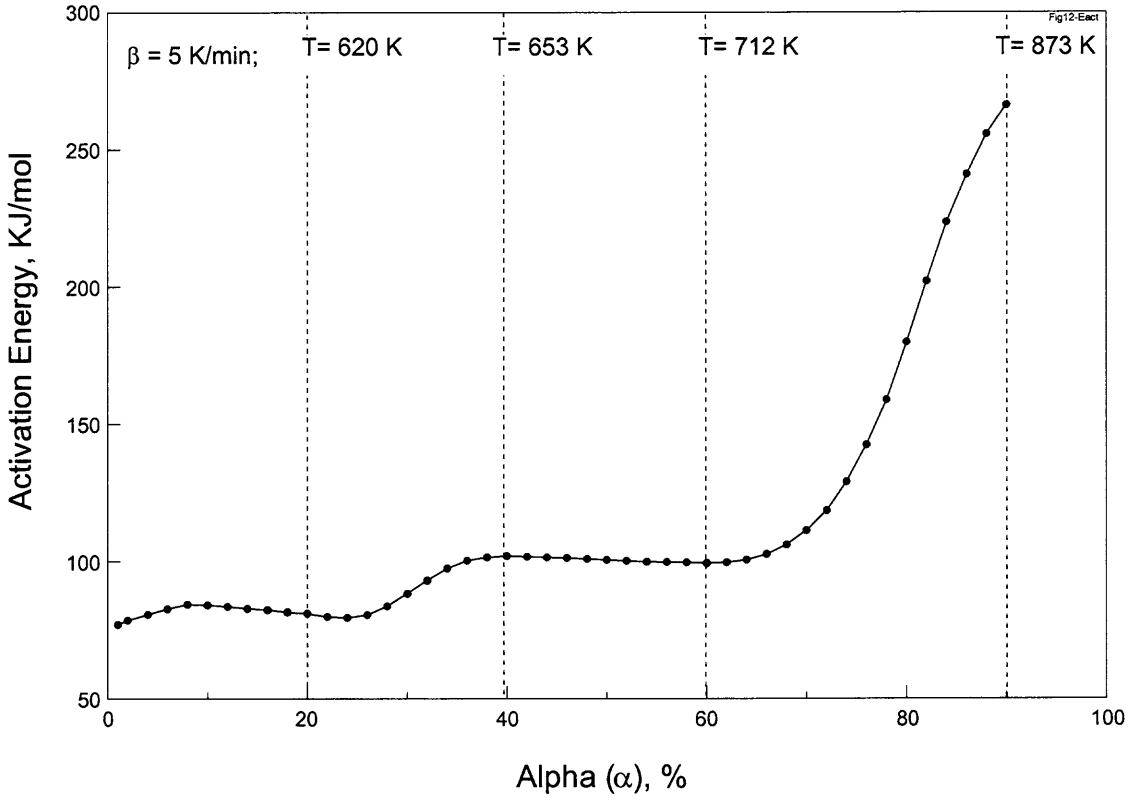

Figure 4.10 Activation energy as a function of reaction progress, α. The dotted lines indicate the reaction temperatures corresponding to the respective values of α at the heating rate of 5 K/min.

The initial value of the activation energy remains close to 80 kJ/mol until a reaction progress of about 30%. This is followed by a segment with an activation energy close to 100 kJ/mol. After about 70% of the overall reaction is completed, the activation energy increases to about 265 kJ/mol. The dependency of activation energy on the reaction progress indicates that at least three different reaction steps need to be considered. This is consistent with the overall DSC signal shape indicating at least three overlapping exothermic events as discussed above. The values of activation energies are also roughly consistent with those shown in Table 4.2, found from the peak position processing using the Kissinger method. Following this initial assessment, the reaction was assumed to comprise three separate steps with the respective activation energies

defined from the flat portions of the curve shown in Figure 4.10. This initial assumption was explored using Netzsch Thermokinetics software [53]. A sequence of calculations was performed in which the activation energies of the three steps remained fixed but the reaction mechanisms and frequency factors were allowed to change to match the experimental results at different heating rates. In addition, the reaction scheme was varied starting with three independent parallel reactions and including different combinations of interdependent reactions occurring in series or in parallel. After a number of calculations, it was found that a close match of the shape of the low-temperature portion of the DSC trace could not be achieved. Thus, it was further assumed that the broad, low-temperature exothermic event corresponding to α up to about 30% consists of two overlapping reaction steps with close activation energies, but different frequency factors and, possibly, reaction mechanisms. A second set of calculations with four reaction steps was therefore performed in which, as described earlier, various combinations of reaction mechanisms and reaction models were considered. As before, the activation energies remained restricted in the three narrow ranges, as implied by the three levels observed in Figure 4.10. While the results were quite sensitive to the selection of individual reaction mechanisms and frequency factors, no significant improvement could be achieved assuming complex interdependent reaction schemes as opposed to the simplest assumption of four independent, parallel reactions. Thus, it was finally found that a reaction mechanism including four independent parallel reactions as described in Table 4.3 provides an adequate match of the experimental DSC traces at different heating rates. The first, low temperature step was modeled as an Avrami-Erofeev n-dimensional nucleation/growth controlled reaction [52] with n=0.6.

The second and third steps were modeled as n^{th} order reactions with n=3.9 and n=2.6, respectively. The fourth step was modeled with an Avrami-Erofeev n-dimensional nucleation/growth controlled reaction with n= 0.75.

Table 4.3 Kinetic Parameters for the Reaction Steps used to Describe DSC Traces for sample 3.

#	Approximate Temperature range (K)	Reaction type	Kinetic Expression $f(\alpha)$	n	E_a (kJ/mol)	Log (A) s^{-1}
1.	350-550	Avrami-Erofeev n-dimensional nucl./growth	$n(\alpha-1)\ln(1-\alpha)^{(n-1)/n}$	0.6	78	6.68
2	450-650	n^{th} order	$(1-\alpha)^n$	3.9	79	5.15
3	600-800	n^{th} order	$(1-\alpha)^n$	2.6	102	5.03
4	850-1000	Avrami-Erofeev n-dimensional nucl./growth	$n(\alpha-1)\ln(1-\alpha)^{(n-1)/n}$	0.75	266	13.3

Figure 4.11 shows a comparison of experimental and calculated DSC traces for different heating rates. Curves illustrating individual reaction steps, as described in Table 4.3 are also shown. In addition, the predicted DSC signal, or the calculated rates of heat release are presented for the higher heating rates approaching those realized in the ignition experiments. Because of different activation energies, the shapes of the traces change and it becomes increasingly difficult to distinguish between contributions from individual reaction steps.

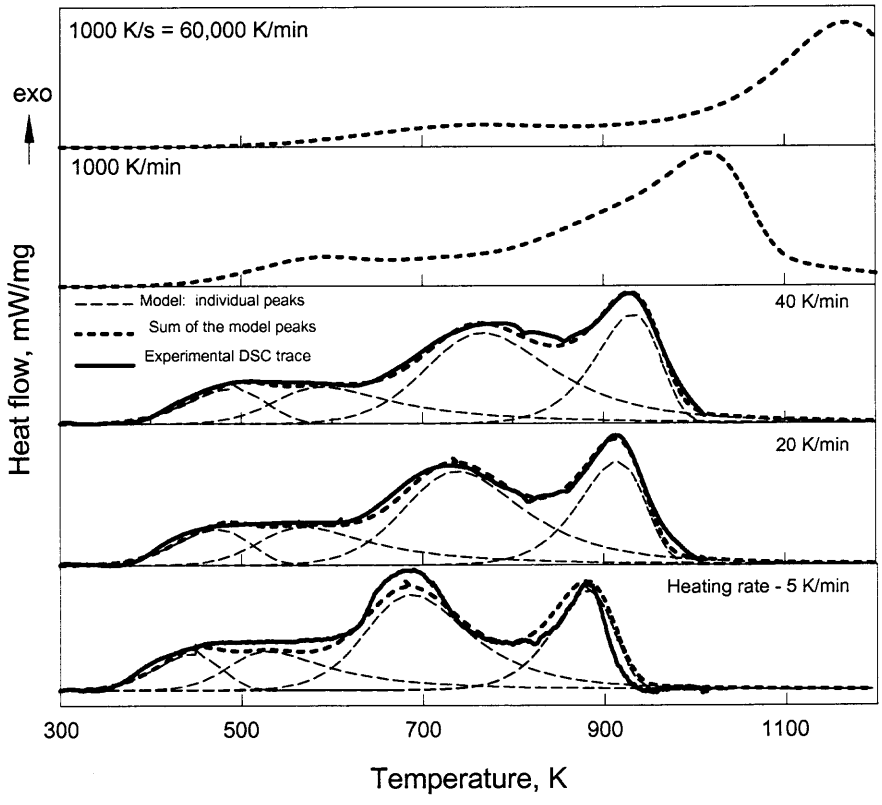

Figure 4.11 Comparison of experimental (solid lines) and calculated DSC traces (dashed lines) for different heating rates. Thin dashed lines show individual reaction steps. Predicted heat flows are also shown for high heating rates approaching the experimental conditions for ignition tests.

4.5 Discussion

The experimental DSC data for different samples were observed to be somewhat different. The results for sample 2, for which the level of structural refinement was relatively low, were similar to the earlier results [15, 16] presented for multilayer Al-CuO_x nanofoils. The first well resolved exothermic peak occurred in the vicinity of 900 K. The activation energy for this peak was estimated to be around 270 kJ/mol (Table 4.2), which compares well with the value of about 280 kJ/mol reported in ref. [16]. The low-temperature processes resulted in a small, low-temperature exotherm that was clearly

detected but poorly resolved for sample 2. On the other hand, these low-temperature events were well resolved for sample 3, which had the same chemical composition as sample 2, but was prepared with a better refinement and a more uniform nanomixing between Al and CuO. Thus, the analysis of the reaction kinetics presented above for sample 3 describes the generic thermite reaction 2Al+3CuO, with a higher reaction rate due to the very high reactive interface area. In terms of thermally activated reaction models, the description obtained by processing specific DSC signals for sample 3 will have values of pre-exponents (or frequency factors) specific for that sample, while the rest of the model should be applicable to any Al-CuO thermites. The quantitative correlation of the frequency factors with the specific sample morphology was beyond the scope of this project but is planned in the future.

The differences observed between the DSC signals recorded for both samples 2 and 3 in oxygen and argon are insignificant. The analysis of intermediate reaction products shows that the reactions in argon start from decomposition of CuO to Cu_2O. The bulk of the released oxygen must have oxidized aluminum in order to explain the observed significant exothermic effect. Thus, it is suggested that amorphous or poorly crystalline aluminum oxide polymorphs were produced even though they were not well visible from the XRD patterns.

For both samples, the initial exothermic effect was nearly the same in oxygen, as it was in argon while the formation of Cu_2O was not detected from XRD for the samples heated in oxygen. This can be interpreted suggesting that the produced Cu_2O quickly re-oxidized interacting with the ambient oxygen. This difference in the reaction products explains the small differences in the reaction kinetics (cf. Table 4.2). Thus, the reaction

kinetics measured for experiments in oxygen represents an additional process of re-oxidation of the produced Cu_2O that is unlikely for the rapid processes occurring in practical applications and in the performed here ignition experiments. Therefore, the heterogeneous reaction kinetics applicable for use in ignition models needs only to describe the reactions in the Al-CuO system, without adding reactions with external oxygen. Such a kinetic model was developed above (cf. Table 4.3) considering the DSC results produced by heating sample 3 in argon.

The proposed model involving four independent parallel reaction steps describes consistently the experimental thermal analysis data. It is interesting to consider which specific reactions could be tentatively assigned to the four steps that were introduced. The comparison can be now made between the kinetic parameters identified in Table 4.3 and those reported in the literature for related reactions in the Al-CuO systems.

Relatively low activation energies were reported for the processes involving decomposition of CuO. The activation energy of reduction of CuO in the presence of hydrogen was found to be 60 kJ/mol [62]. In another report, the reaction $4CuO \rightarrow 2Cu_2O+O_2$ taking place via a moving phase boundary and rate limited by oxygen diffusion along the Cu_2O grain boundaries, was found to have an activation energy of 106 kJ/mol [63]. On the other hand, activation energies in a broad range have been reported for the aluminum oxidation that is rate-limited by diffusion through growing Al_2O_3 scales. A sequence of Al_2O_3 polymorphs including $amorphous \rightarrow \gamma \rightarrow \theta \rightarrow \alpha$ phases was reported to be produced upon aluminum heating in oxygenated gases [64]. This sequence is expected to be modified by the presence of other condensed phases, such as CuO_x, but the overall scheme of aluminum oxidation including a sequence of transition alumina

phases leading to the formation of the stable α–Al_2O_3 should remain. The related activation energies for the consequent oxidation steps of aluminum powders in oxygen were identified in ref. [57] as 120, 227, and 306 kJ/mol for the growth of amorphous, γ- and α-alumina polymorphs, respectively.

Interestingly, the initial process of growth of the amorphous alumina has the activation energy comparable to that of CuO decomposition. However, the activation energy increases significantly upon formation of crystalline alumina polymorphs at higher temperatures.

Comparing the activation energies reported in the literature for CuO decomposition and alumina growth with the values presented in Table 4.3, it can be suggested that the initial steps of the Al-CuO reaction are controlled by CuO decomposition. This suggestion is supported by the XRD patterns analyzed for the samples quenched from intermediate temperatures. At higher temperatures, the rates of these decomposition processes are supplemented by the growth of amorphous alumina that could not be detected by XRD. The above processes can be assigned for the introduced steps 1-3 which all have relatively low activation energies. An increase in the activation energy in step 4 signals that the growth of crystalline Al_2O_3 polymorphs becomes the rate-limiting reaction step.

Because the four events were assumed to be independent of one another, the total heat release of thermite reaction can be found simply as a sum of the heats released in each event:

$$\dot{Q}_{total} = \sum_{i=1}^{4} \dot{Q}_i \tag{4.1}$$

Considering specific expressions and parameters of individual terms, $\dot{Q}_i$, described in Table 4.3, the heat release as a function of temperature and heating rate for the overall Al-CuO thermite reaction can now be described. As noted above, the frequency factors are specific for the particular sample morphology used in this research and one needs to re-determine their values for different nanocomposite materials. The overall reaction mechanism, however, is expected to remain valid for any Al-CuO composites.

In order to use the proposed reaction mechanism for quantitative description of ignition experiments, a detailed heat transfer model needs to be developed describing the ignition experiment and including the term given by Eq. (4.1), using the specific kinetic parameters presented in Table 4.3. Such a model was outside the scope of this project. Instead, the validity of the proposed mechanism was assessed by relating thermal analysis to ignition experiments via an isoconversion approach. This assumes that ignition occurs at a constant degree of reaction progress α (see Figure 4.10). Figure 4.12 shows an Arrhenius diagram where a group of curves representing constant reaction progress are superimposed on the experimentally observed ignition temperatures. The plot suggests that ignition occurs when approximately 4 % of the total reaction enthalpy is released. The temperatures where 4 % reaction progress is observed in the thermal analysis experiments have been determined and are also shown for reference. These experimental points correlate well with the calculated lines of constant reaction progress, which is to be expected considering the good match between the experimental and calculated DSC curves shown in Figure 4.11. This indicates that ignition indeed can be described adequately by the overall reaction kinetics model reported here.

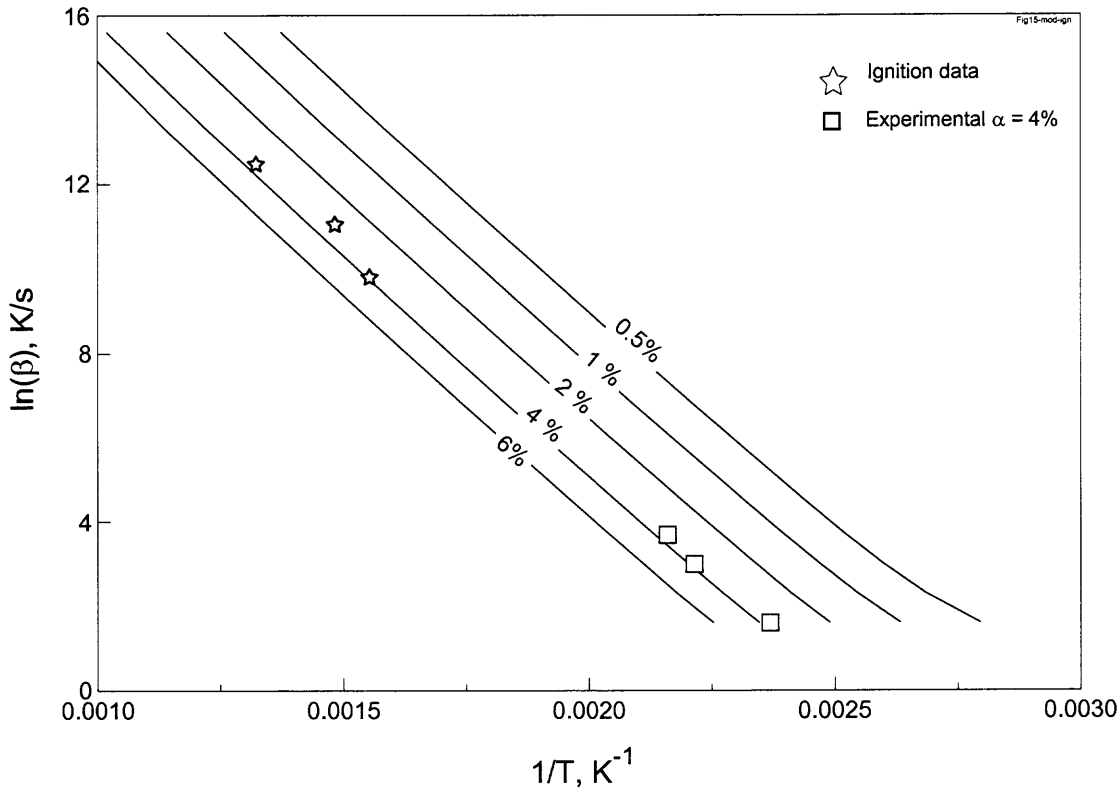

Figure 4.12 Comparison of ignition experiments and thermal analysis data at selected levels of reaction progress with the lines of constant reaction progress calculated according to the introduced kinetic model.

4.6 Conclusions

The highly exothermic heterogeneous reaction between Al and CuO was found to start at relatively low temperatures (~ 400 K) and is well described by four parallel reaction steps. Earlier measurements did not resolve the low-temperature exothermic events and focused on the strongest, fourth reaction step. However, ignition of the nanocomposite Al-CuO materials was shown to be driven primarily by the lower-temperature oxidation processes.

Specific mechanisms and kinetic parameters were determined to describe the individual reaction steps for the prepared nanocomposite powders. These mechanisms include the frequency factors specific for the powders used in this study and activation energies that should remain valid for any Al-CuO composite materials. The identified reaction steps were tentatively assigned to specific processes of CuO decomposition followed by diffusion of reacting species through amorphous and then crystalline Al_2O_3 polymorphs. It was shown that ignition of Al-CuO nanocomposite powders can be described reasonably well using the proposed kinetics of Al-CuO heterogeneous reactions. Future work will focus on development of a complete, quantitative ignition model.

CHAPTER 5

ALUMINUM RICH Al-MoO_3 NANOCOMPOSITE POWDERS PREPARED BY ARRESTED REACTIVE MILLING

5.1 Problem Statement

Previous results have shown that micron-sized nanocomposite powders prepared by ARM have a high reactivity comparable to that of chemically similar mixed nanopowder compositions, while offering potential advantages in handling, maximum packing density, and cost [18-22]. For many applications of energetic formulations, an external oxidizer, e.g., oxygen from air or from a propellant formulation will be utilized and thus the stoichiometric thermite compositions are of limited interest. For such applications, it is proposed to develop off-stoichiometric, metal rich reactive nanocomposites. This project deals with the corresponding Al-MoO_3 compositions. One objective of this work is to determine the maximum aluminum concentration that can be used in order for the nanocomposite to remain sufficiently reactive to warrant its practical applications. The project includes synthesis of several nanocomposite powders and characterization of their morphologies and reactivities. X-ray diffraction, electron microscopy, and thermal analysis were used to characterize the prepared materials. In addition, ignition tests using an electrically heated filament and constant volume explosion experiments were also conducted.

5.2 Material Synthesis

A shaker mill (8000 series by Spex CertiPrep) was employed in this research. Flat-ended steel vials were used along with steel milling media of 5 mm diameter. Starting blends were prepared in off-stoichiometric proportions from powders of elemental aluminum (99% pure, -325 mesh by Alfa Aesar) and molybdenum trioxide MoO_3 (99.95% pure, by Alfa Aesar). Synthesis was carried out in argon environment using 5 g powder batches with different Al/MoO_3 ratios. 4 ml of hexane (C_6H_{14}) was added as a process control agent (PCA) to inhibit both cold welding and partial reaction during milling. The process temperature was monitored using a thermistor attached to the side of the milling vial and connected to a digital data logger. The instant of reaction was marked by a sharp rise in the vial temperature. The stoichiometric composition requires 2 moles of Al corresponding to each mole of MoO_3. Preliminary experiments in which the samples were milled dry established that the self-sustaining reaction was mechanically triggered during milling for the blends with up to 10 moles of Al per mole of MoO_3. Typically, the reaction would occur within the first few minutes of dry milling. It was also observed that adding hexane as a process control agent enabled us to avoid rapid triggering of exothermic reaction and obtain uniform nanocomposite powders. For further experiments, four samples were prepared with aluminum concentrations of 4, 8, 12 and 16 moles per mole of MoO_3. Wet milling (with hexane as PCA) and a constant milling time of 30 min were used to achieve a similar degree of structural and compositional refinement for all samples. After milling the samples were collected and stored in an argon-filled glove box.

5.3 Sample Characterization

Morphology and composition of the nanocomposites were examined on a LEO 1530 Field Emission Scanning Electron Microscope (SEM) operated at 10 kV. The nanocomposite samples were embedded in epoxy and cross-sectioned for examination. The phase composition was determined for each nanocomposite by x-ray diffraction (XRD). The XRD was performed on a Phillips X'pert MRD powder diffractometer operated at 45 kV and 45 mA using Cu Kα radiation ($\lambda = 1.5438$ Å).

Temperature dependent structural transformations were determined by differential scanning calorimetry (DSC) using a Netzsch Simultaneous Thermal Analyzer STA409 PC. Alumina pans were used and the furnace was flushed with argon at approximately 50 ml/min. DSC traces were recorded with heating rates varying from 1 to 40 K/min. The samples were heated from room temperature to 1200 K, held at 1200 K for 30 min, and then cooled to room temperature. Without disturbing the experiment, the samples were then heated to 1200 K for the second time to record the baseline signal. The temperature was accurate within ±1 K.

5.4 Ignition and Constant Volume Explosion Experiments

Ignition of the prepared powders was studied at heating rates ranging approximately from 2,000 to 20,000 K/s. The reactive powder was coated on an electrically heated Nichrome® filament. The value of the DC voltage applied to the filament determined the experimental heating rate. The temperature of the uncoated portion of the filament was monitored with an infrared pyrometer. Light emission from the powder coating was detected by a separate photo-sensor. A sharp onset of the light emission was taken as

evidence of ignition and the temperature recorded for that instant was considered as the measured ignition temperature. The setup is described in detail elsewhere [24, 42].

Combustion of the prepared nanocomposite powders was studied using constant volume explosion (CVE) experiments. A 9.2 L explosion vessel was used. The vessel was initially evacuated. A short gas blast delivered from a high pressure reservoir through a nozzle with multiple small openings introduced powder into the vessel and simultaneously established the initial gas environment and pressure. After a short delay, aerosolized powder was ignited by a heated filament placed in the center of the vessel and the pressure was monitored using a pressure transducer. Experiments were performed in a mixture of 22.5 % O_2 and 77.5 % N_2. The ratio of the maximum explosion pressure to the initial pressure before ignition, and the maximum rate of pressure rise were used to assess the energy released in each explosion and the rate of combustion, respectively. Condensed combustion products were collected after each experiment for subsequent analysis. In addition to the nanocomposite powders, a spherical aluminum powder by Atlantic Equipment Engineers, 99.9 % pure, nominal size 1 – 5 μm was used in these experiments for reference. This reference sample was selected based on earlier experiments [65] where it was found to give the highest explosion pressures and rates of pressure rise among several different aluminum powders. A detailed description of the experimental setup and procedure is available elsewhere [28, 29]. The experimental methodology is based on a technique developed by the U.S Bureau of Mines for characterization of the explosibility of various dusts [66-67]. In the preliminary tests using the experimental conditions described in Ref. [29], it was found that some of the nanocomposite powders ignited upon entering the explosion vessel with

the gas blast. To avoid such uncontrolled ignition, the gas blast duration was increased, while the pressure in the reservoir was reduced. The final operating parameters were as follows: gas blast duration: 500 ms, reservoir pressure: 2.45 atm, initial pressure in the explosion vessel prior to ignition: 1 atm, delay between the gas blast and ignition: 300 ms.

5.5 Results and Discussion

5.5.1 Particle Sizes

Particle size distributions of the nanocomposite powders were determined by low angle laser light scattering using a Coulter LS 230 enhanced laser diffraction particle size analyzer. Measurements required suspension of small quantities of powder in de-ionized water. Figure 5.1 shows the particle size distribution (PSD) of the as-milled nanocomposite powders as well as for the spherical aluminum powder used for reference in the CVE experiments. It was observed that the particle size increased with increasing aluminum concentration. For the results of CVE experiments to be useful in terms of identifying the effect of material composition, the particle sizes for powders of different materials must be close. The PSD of the nanocomposite sample with bulk composition $4Al + MoO_3$ was found to be reasonably close to that of the reference aluminum powder. However for the nanocomposite samples with higher aluminum concentrations, the particles were noticeably coarser when compared to the reference aluminum. Therefore, the above nanocomposite powders were size-classified using a 450 mesh sieve. Figure 5.2 shows the PSD of the size-classified powders used in CVE experiments (along with as-prepared $4Al+MoO_3$ and spherical Al powders). The particle sizes for the sieved

powders were still noticeably coarser than for the reference aluminum, which should be considered while interpreting the results of the CVE experiments. In the future, if necessary particle sizes can be reduced using milling at cryogenic temperatures or other techniques.

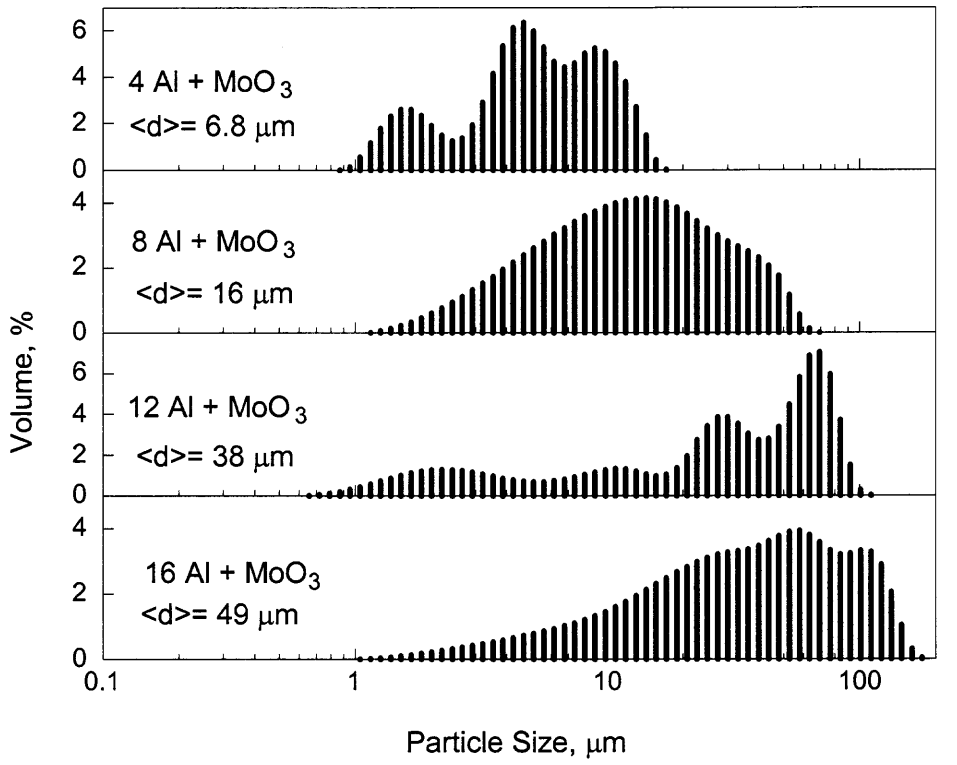

Figure 5.1 Particle size distribution of the as-milled nanocomposite powders.

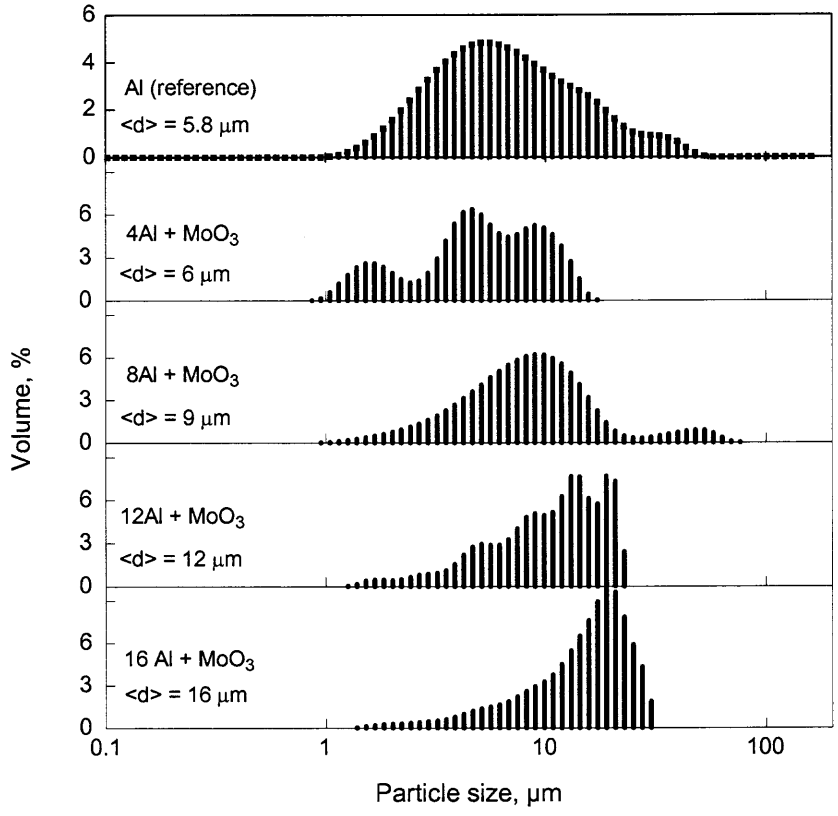

Figure 5.2 Particle size distribution of the nanocomposite powders after sieving. The size distribution is also shown for aluminum powder used for reference constant volume explosion experiments.

5.5.2 Morphology of Nanocomposite Powders

Back-scattered SEM images of cross-sectioned samples of the Al-MoO_3 nanocomposites with different bulk compositions are shown in Figure 5.3. The dark background is epoxy used for embedding the sample; the grey areas indicate aluminum matrix whereas the light inclusions indicate MoO_3. Al and MoO_3 are sandwiched together and form a fully dense material with a highly developed reactive interface. For all the prepared compositions, the elongated, nano-sized MoO_3 inclusions were uniformly distributed in the Al matrix. No significant change in the size of MoO_3 inclusions as a function of the bulk material composition was observed.

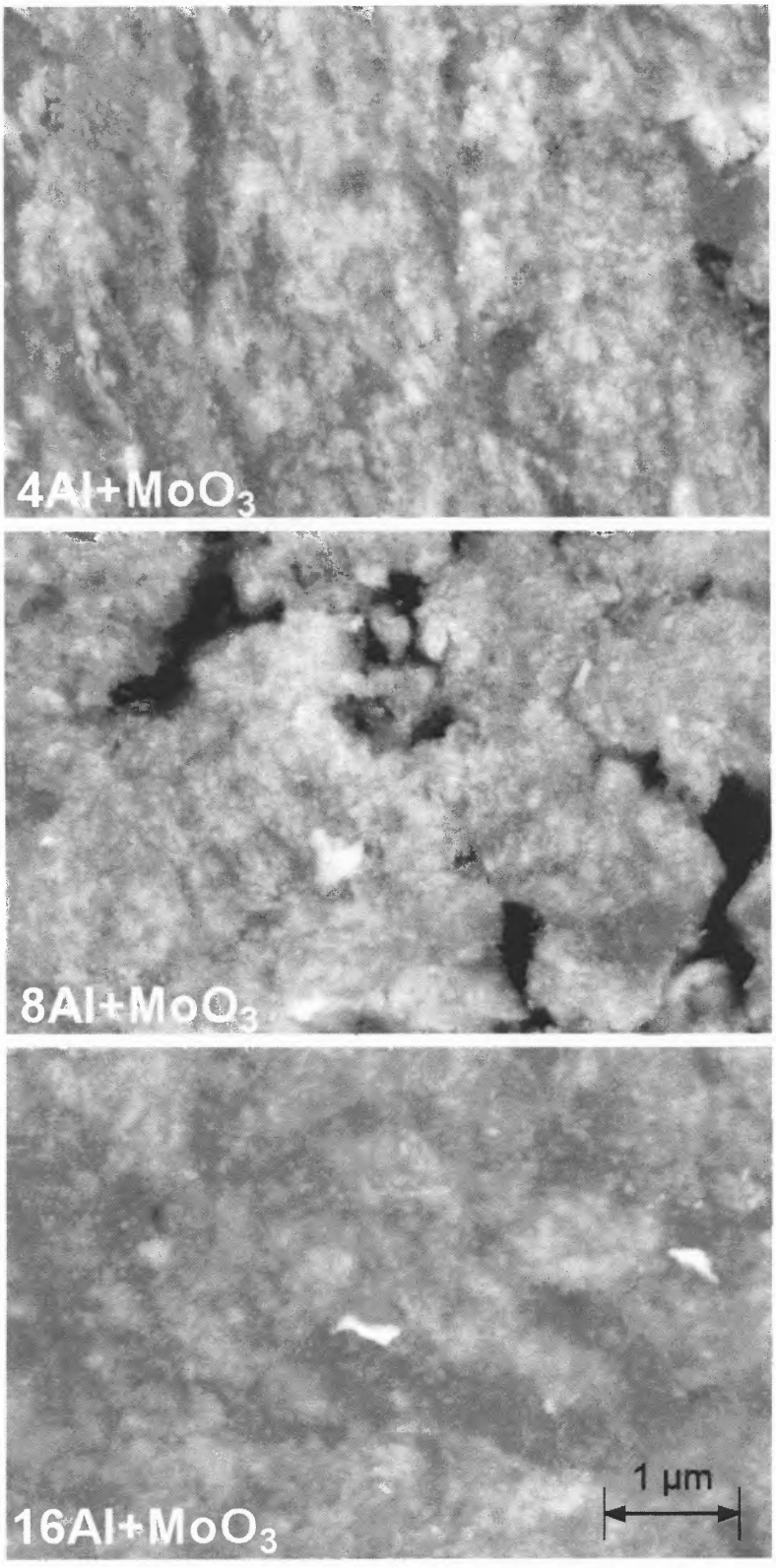

Figure 5.3 Backscattered electron SEM image of Al-MoO_3 nanocomposites with varying concentration of Al.

. In some samples, the presence of the fully reacted phases, e.g., Mo (very bright, white component) and Al_2O_3 (dark, uniform component) was detected indicating that during milling chemical reaction was initiated, although did not propagate over the entire sample. Most of the reacted phases were observed for the $4Al+MoO_3$ sample. This reaction is undesirable and should be avoided for optimized synthesis conditions.

5.5.3 Phase Compositions

Figure 5.4 shows the XRD patterns of the nanocomposites synthesized with different aluminum concentrations (note that SiO_2 peaks appear because quartz powder was added as an internal standard for the XRD measurements). As expected, the intensities of Al peaks decrease and of MoO_3 peaks increase with reduced aluminum concentration. The aluminum peak at around 45° is somewhat distorted because of an overlap with a peak of Fe occurring nearly at the same angle, Iron in the XRD patterns, indicates minor contamination of the sample by the milling media. Peaks of $MoO_3H_{0.5}$ are observed for all samples. The intensity of these peaks changes only slightly with sample composition. A possible source of hydrogen could be hexane used as a surface control agent. Presence of metallic Mo was also noticed in the XRD patterns. Metallic Mo indicates that reaction between Al and MoO_3 was mechanically triggered during milling, but was not self-sustained. To assess the extent of this undesirable partial reaction, the XRD patterns were processed using the GSAS whole pattern refinement software [45]. The relative amounts of Mo and MoO_3 phases were compared for all samples. The calculated mass ratio of Mo and MoO_3 as a function of bulk aluminum concentration is shown in Figure 5.5. It is clear that the reaction was most significant for the $4Al+MoO_3$ sample. The

crystallite size of aluminum was also evaluated from the refinement. It was estimated to vary in the range of 35 – 45 nm.

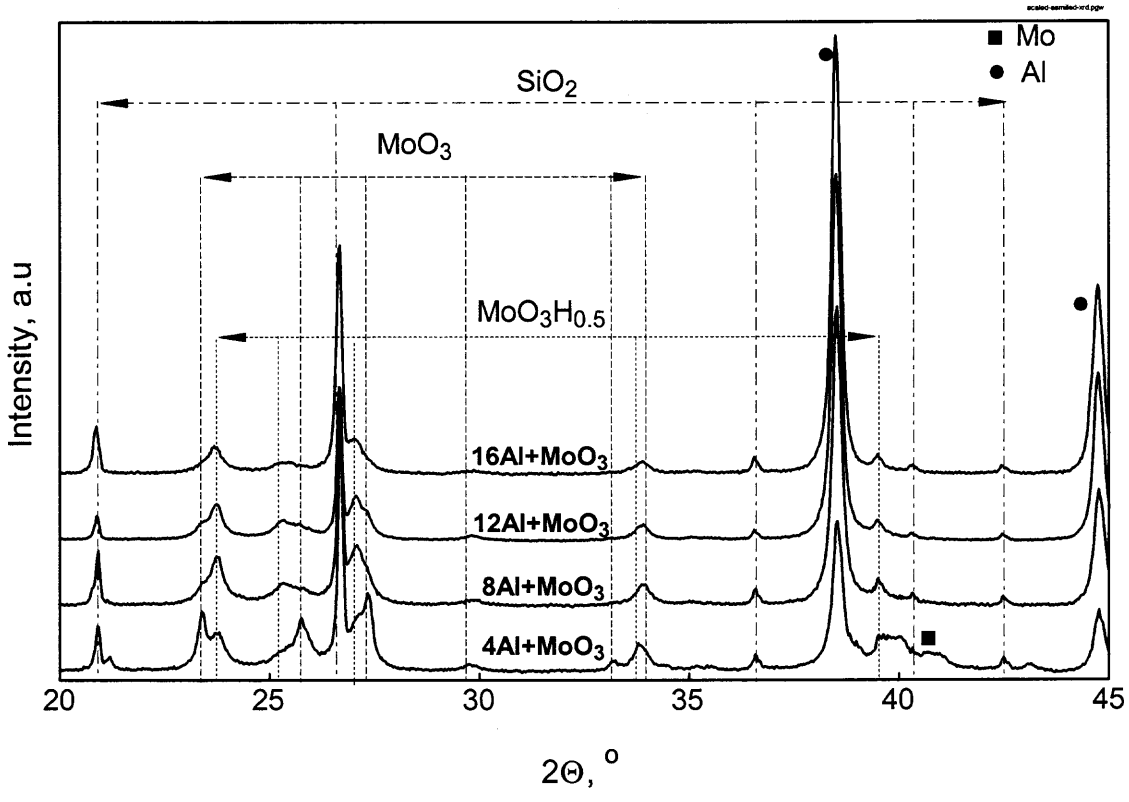

Figure 5.4 XRD patterns of samples with varying concentrations of Al.

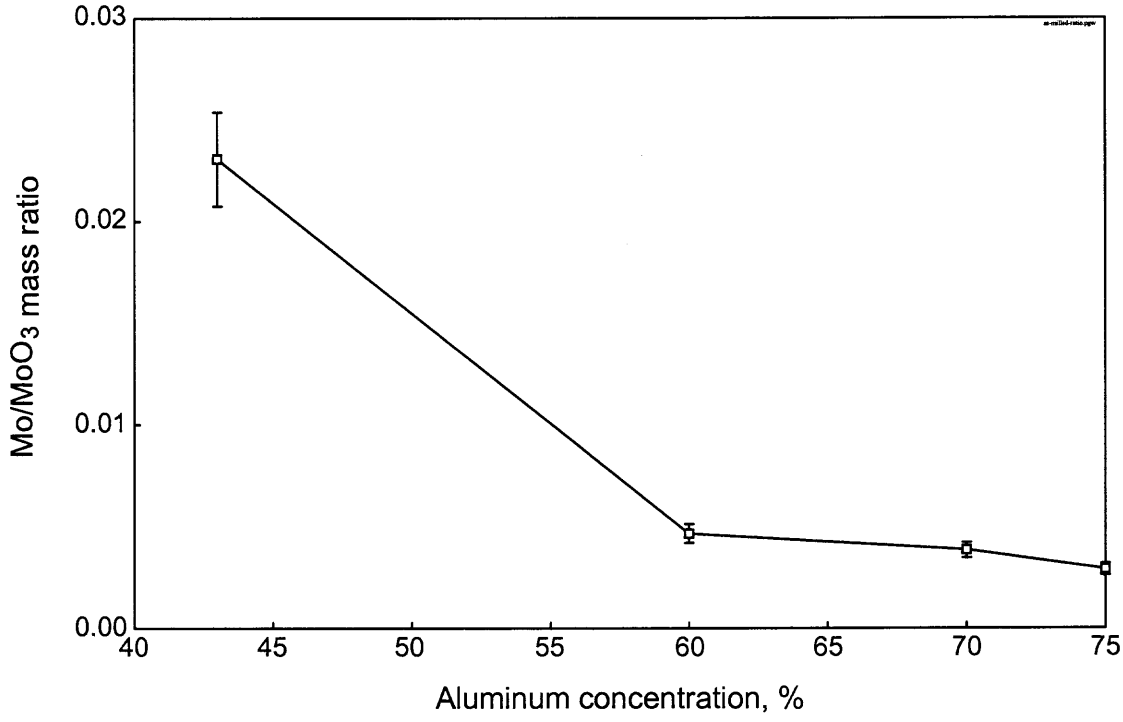

Figure 5.5 Mass ratio of Mo/MoO_3 phases calculated using experimental XRD traces and whole pattern refinement software [45] for samples with different aluminum concentrations.

5.5.4 Reactions upon Heating

Figure 5.6 shows baseline corrected DSC traces for the three nanocomposite samples with different bulk compositions heated to 1200 K at a rate of 2 K/min. The heating was accompanied by several overlapping exothermic peaks occurring before the aluminum melting point, which is indicated by a vertical dotted line. For all samples, the first exothermic process starts at a temperature below 400 K. A broad exothermic hump was reproducibly observed between 350 and 500 K. This hump was followed by a weak exothermic peak between 600 and 750 K. A strong exothermic peak was observed to occur between 800 and 900 K. Additional weak and poorly resolved exothermic features were observed, e.g., around 700 and 900 K. An exothermic peak was also observed in the vicinity of 1000 K, above the melting point of Al. An endothermic peak indicating

aluminum melting was not clearly detected for all samples, most likely because of overlap with exothermic features. A second strong endothermic peak was observed for the 16Al+MoO_3 sample at 1000 K. This peak appears to indicate melting of $Al_{12}Mo$ and peritectic formation of Al_5Mo reported to occur around 1000 K [68]. For samples with lower concentration of aluminum, this endothermic peak was masked by an exothermic peak.

The kinetics of the observed exothermic reactions is of interest for both modeling ignition and predicting stability of the prepared nanocomposite powders. However, the quantitative analysis of such kinetics is not straightforward. An initial attempt was made to analyze the obtained DSC traces using an isoconversion approach [69]. It was found, however, that such analysis is not meaningful and that a detailed kinetic model needs to be developed instead. Development of such a model is outside the scope of this paper and will be addressed in future work. Additional details describing isoconversion data processing from the DSC experiments with metal-rich Al-MoO_3 nanocomposite powders are available elsewhere [69].

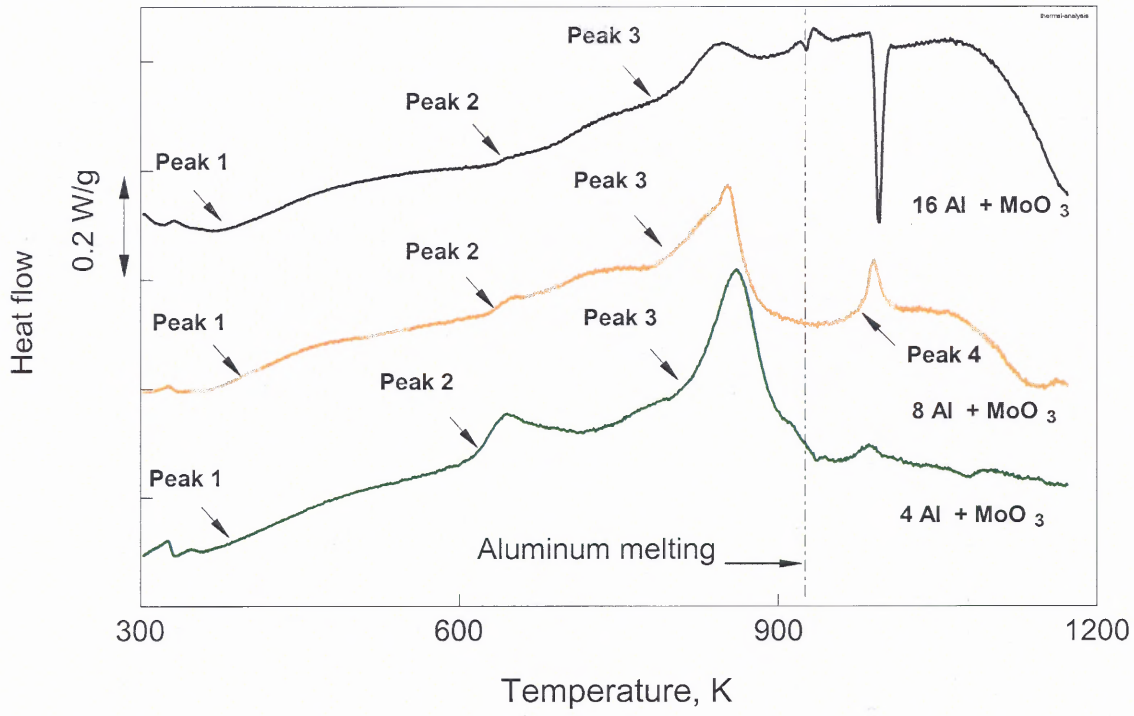

Figure 5.6 Baseline corrected DSC traces of nanocomposite powders recorded a 2 K/min.

5.5.5 Ignition Temperatures

Figure 5.7 shows the ignition temperatures of the Al-MoO_3 nanocomposites as a function of heating rate. Each point represents the average of at least seven measurements taken at the same experimental conditions. The error bars show the standard deviations obtained for each experimental data set. Aluminum melting point is shown for reference as a dotted line. Clearly, all samples ignited at temperatures well below the Al melting point. At the lowest heating rate used (around 2000 – 3000 K/s), ignition occurred in about the same temperature range of 720 – 750 K for all the samples.

For the sample with bulk composition 16Al+MoO_3, increased heating rates resulted in higher ignition temperatures, as expected for a thermally activated ignition process. For this specific composition, extrapolating the resulting trend line to a

practically interesting heating rate of 10^6 K/s results in an estimated ignition temperature of 1160 K.

For samples with lower concentrations of Al, an increase in the heating rate initially resulted in a small but reproducible decrease in the ignition temperature. Further increase in the heating rate resulted in the regular trend of increased ignition temperature. Note also that all three remaining samples ignited at very close temperatures for all heating rates. Following the trend line shown in Figure 5.7 based on the two higher heating rate experiments (and neglecting the point at the lowest heating rate) combined for all three of these samples, it is predicted that these powders would ignite at about 910 K at a heating rate of 10^6 K/s. The unusual decrease in the ignition temperature observed for the three samples between the heating rates of approximately 2000 and 7000 K/s can be interpreted assuming a change in the ignition mechanism occurring upon increase in the heating rate. In other words, it can be suggested that for these materials, different exothermic processes result in a thermal runaway when the samples are heated at different heating rates.

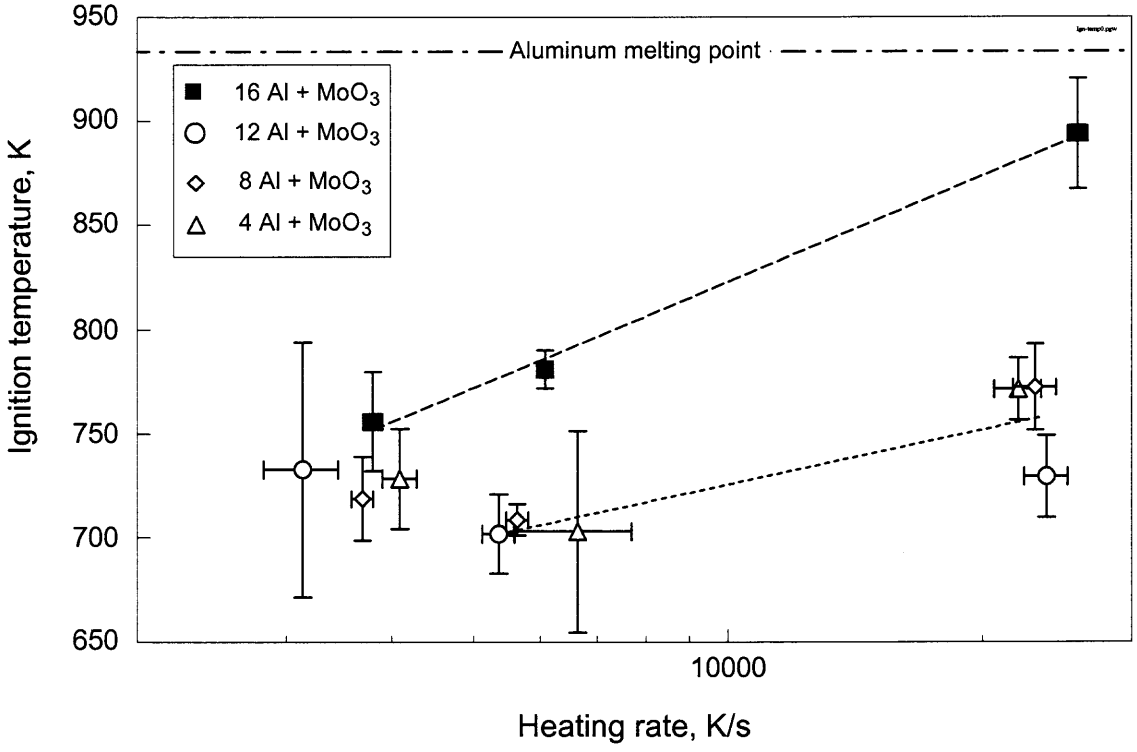

Figure 5.7 Ignition temperatures of the nanocomposites at different heating rates.

5.5.6 Combustion Experiments

The main goal of the CVE experiments was to compare the combustion performance of different reactive nanocomposite powders between one another as well as to compare their performance with that of a pure aluminum powder. Before the experiments, adiabatic flame temperatures and respective combustion product compositions were determined for different materials using the NASA CEA (Chemical Equilibrium with Application) code [70]. Calculations were performed for a constant volume case, with the volume of the combustion chamber filled with a gas mixture of 22.5 % O_2 and 77.5 % N_2, selected to match the volume of the experimental explosion vessel, 9.2. L. Predicted adiabatic flame temperatures for the varied mass loads for different fuels are shown in Figure 5.8. The nanocomposite powders were represented by their respective bulk

compositions of Al and MoO_3. Presence of small quantities of reaction products formed during milling was neglected.

For experiments with Al powder, the mass load was selected that resulted in the highest predicted adiabatic flame temperature, i.e. 2.89 g. This case corresponded closely to a stoichiometric Al-air mixture. A similar choice could not be made for all the nanocomposite powders because the increase of the mass of powder, which includes both fuel and oxidizer, can result in a continuous increase in the flame temperature, as clearly seen for $4Al+MoO_3$ (cf. Figure 5.8). For nanocomposite powders with smaller aluminum concentrations, the fuel loads corresponding to the maximum temperatures increase significantly compared to that of pure Al. Therefore, selection of the mass loads for nanocomposite fuels as matching the maximum predicted adiabatic flame temperatures was impractical. Instead, the mass loads of nanocomposite powders were selected to match the volume of the reference aluminum sample. In other words, the volume of the powdered fuel used in the CVE experiments remained constant for all the materials. The powder loads used in these experiments for different materials are shown in Table 5.1. Also shown in Table 5.1 are equivalent masses of pure Al per powder load for each material.

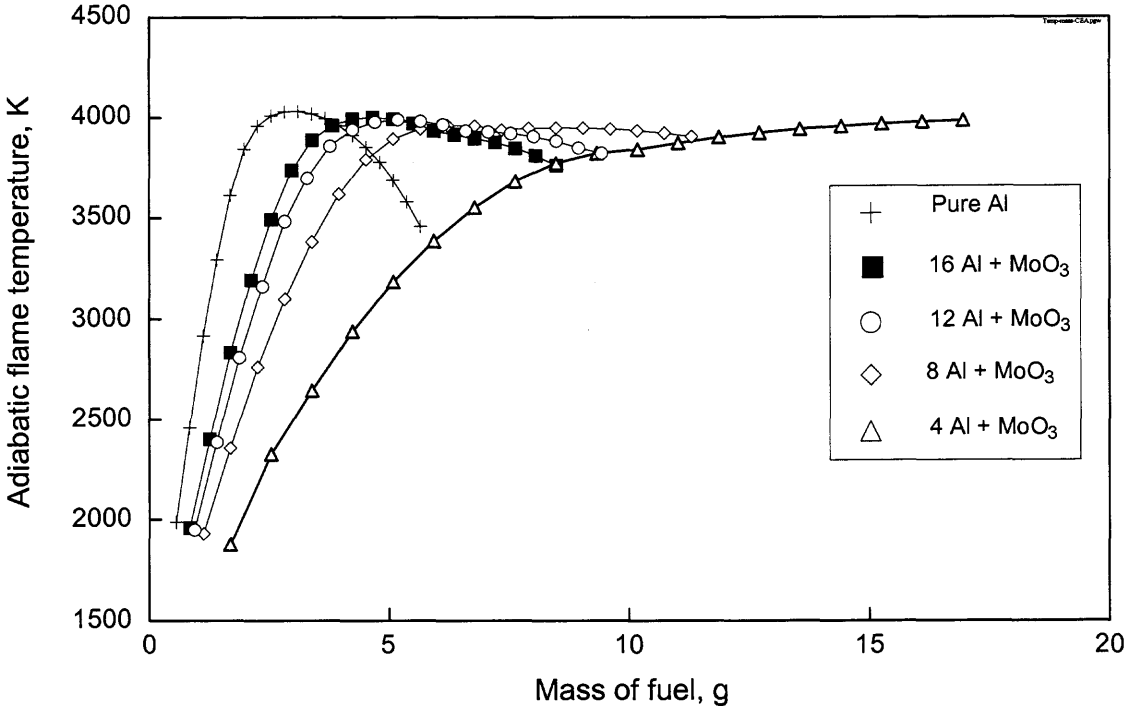

Figure 5.8 Calculated adiabatic flame temperatures for the N_2/O_2 gas mixtures with a fixed O_2 concentration of 22.5 % with Al and xAl+MoO_3 fuels.

Table 5.1 Mass Load of Al and Equivalent Mass of Metallic Fuel of the xAl + MoO_3 Nanocomposites

Fuel	Mass Load, g	Equivalent aluminum mass, g
4 Al + MoO_3	3.81	1.64
8 Al + MoO_3	3.48	2.09
12 Al + MoO_3	3.32	2.29
16 Al + MoO_3	3.23	2.42
Al	2.89	2.89

Characteristic CVE pressure traces for different materials are shown in Figure 5.9. The pressure trace recorded in an experiment with pure Al powder indicates a significant delay between the instant the igniter was triggered and the time when a substantial increase in pressure was observed. However all nanocomposite powders ignited without any noticeable delay, an indication of their higher reactivity as compared to aluminum.

In a first approximation, the ratio of the maximum CVE pressure, P_{max}, over initial pressure in the vessel can be considered proportional to the flame temperature. The maximum pressures are practically identical for pure Al and for the 8Al+MoO_3 nanocomposite powder. The maximum pressures are somewhat lower for other nanocomposite samples.

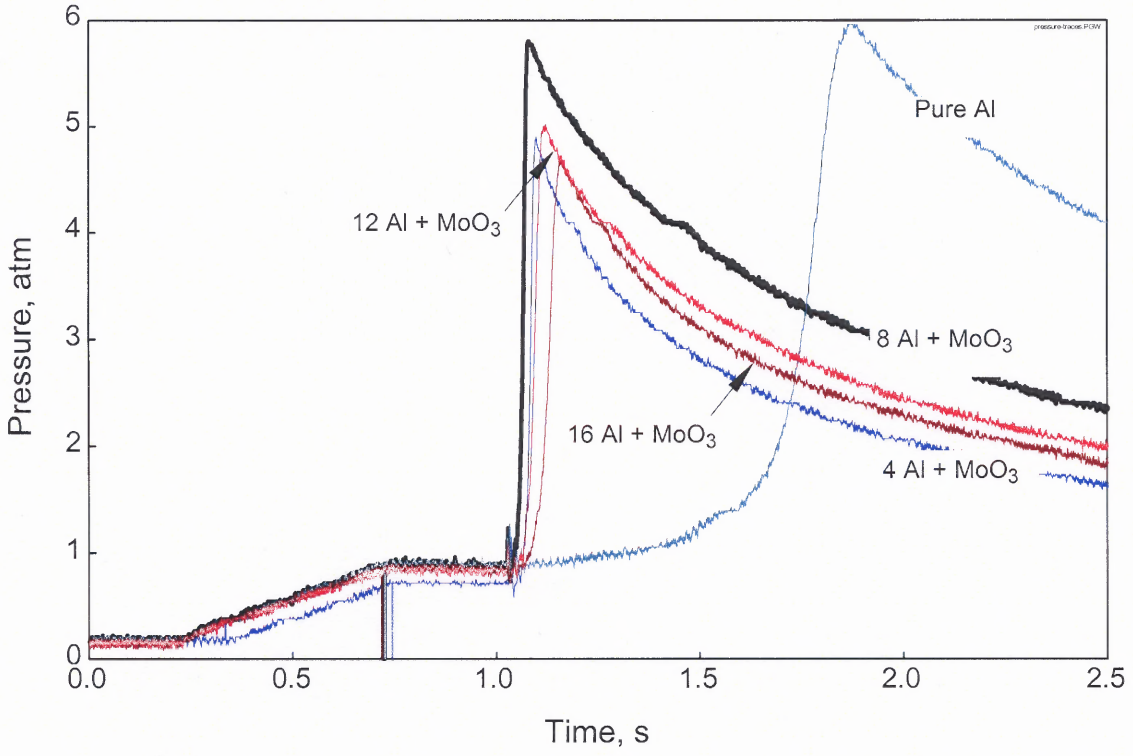

Figure 5.9 Pressure traces of the Al and Al-MoO_3 nanocomposites with varying Al concentration recorded during CVE.

A crude evaluation of the heat release produced in CVE experiments can be made assuming that the released heat, ΔQ is generally proportional to the temperature increase in the vessel:

$$\Delta Q \cong \rho v C_v \left(T_{\max} - T_{\text{ini}}\right) \qquad 5.1$$

where the ρ and v are respectively the density and volume of the mixture, C_v is its specific heat at constant volume, and T_{ini} is its initial temperature (i.e., room

temperature). Assuming further that the behavior of the heated combustion products is similar to that of an ideal gas, one can write that

$$T_{\max} \approx T_{\text{ini}} \frac{P_{\max}}{P_{\text{ini}}} \qquad 5.2$$

Therefore, the heat release per gram of aluminum in each of the tested powders can be compared based on the following estimate

$$\frac{\Delta Q}{m_{Al}} \sim \frac{T_{\text{ini}}}{m_{Al}} \left(\frac{P_{\max}}{P_{\text{ini}}} - 1 \right) \qquad 5.3$$

The left hand side of the latter equation is plotted in Figure 5.10 as a function of the material composition. Aluminum mass is taken from Table 5.1. Based on Figure 5.10, it appears that for both $4Al+MoO_3$ and $8Al+MoO_3$ nanocomposite powders the energy release per gram of aluminum was nearly the same and much higher than that for pure aluminum powder. However, with the increased aluminum concentration, the energy release quickly approaches that of pure aluminum, indicating reduced combustion efficiency. Most likely, the reduced combustion efficiency is associated with the larger particle size for the nanocomposite powders with higher aluminum concentrations. Thus, reducing particle sizes for such materials, e.g., by using milling at cryogenic temperatures, may prove to be a promising approach.

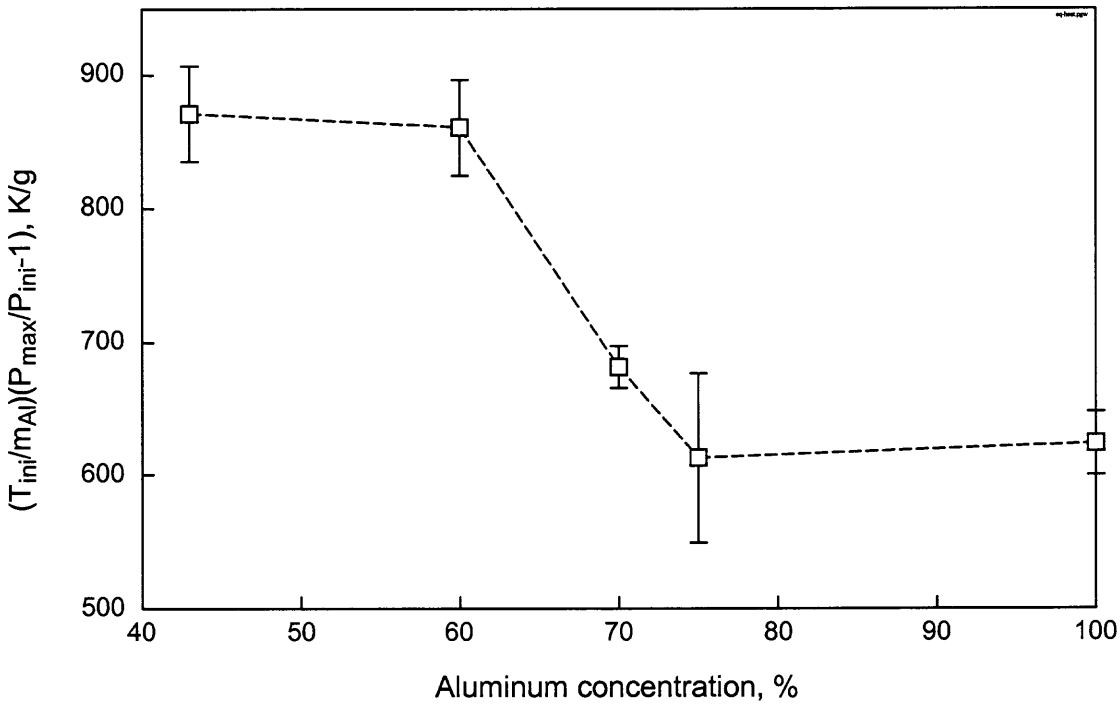

Figure 5.10 Equivalent heat of reaction normalized per mass of aluminum for different powder compositions.

The combustion rate of the powders is evaluated from the maximum rate of pressure rise, dp/dt_{max}, proportional to the burn rate for the CVE experiments [71]. The dp/dt_{max} was calculated by processing the recorded pressure traces. The results in terms of the maximum rates of pressure rise plotted as a function of the material composition are shown in Figure 5.11. The value of dp/dt_{max} and thus the burn rate of the sample containing 8 moles of Al was the highest. The burn rates for all prepared nanocomposite powders exceed that of pure aluminum.

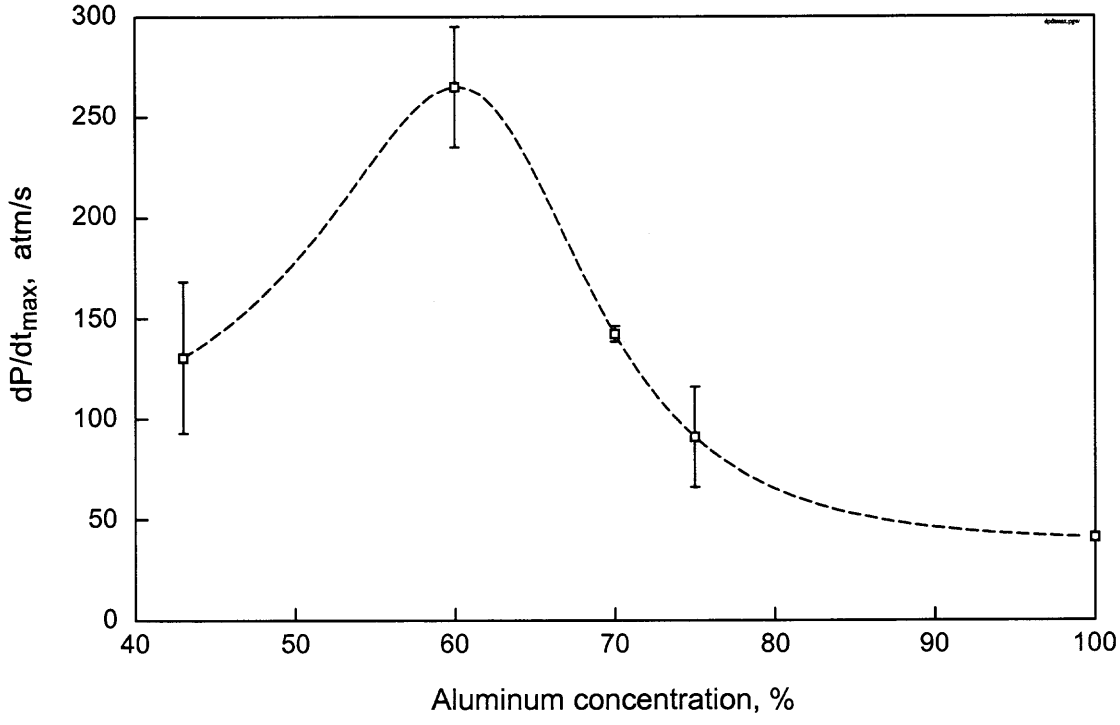

Figure 5.11 The maximum rates of pressure rise measured in CVE experiments, dp/dt_{max}, as a function of the powder composition. The dashed line indicates a polynomial interpolation to fit the data points.

The combustion products were collected and their composition was investigated using x-ray powder diffraction. The resulting XRD patterns are shown in Figure 5.12. Once again, quartz was added to the samples as an internal standard. In agreement with the combustion efficiency of aluminum discussed above (cf. Figure 5.10), the peaks of metallic Al indicating unburned metal are stronger for the products of powders with higher initial aluminum concentrations. The peaks of WO_3 are most likely due to the presence of burned fragments of the igniter wire made of tungsten.

A more quantitative estimate of the reaction completeness can be obtained by comparing the intensity ratio of a characteristic Al_2O_3 peak to that of a characteristic Al peak. This ratio as a function of the material composition (including the results for pure Al powder not presented in Figure 5.11), is shown in Figure 5.12. As expected, the

reaction is most complete (the highest ratio of Al_2O_3/Al peak intensity) for the lowest aluminum concentration in the nanocomposite powder. For the sample with bulk composition 16Al+MoO_3, the reaction completeness is less than that of pure Al powder. Again, this can be explained by a substantial difference in the particle sizes (cf. Figure 5.2). Even after sieving, the nanocomposite particles had an average particle size of 16 μm as compared to 6 μm for aluminum.

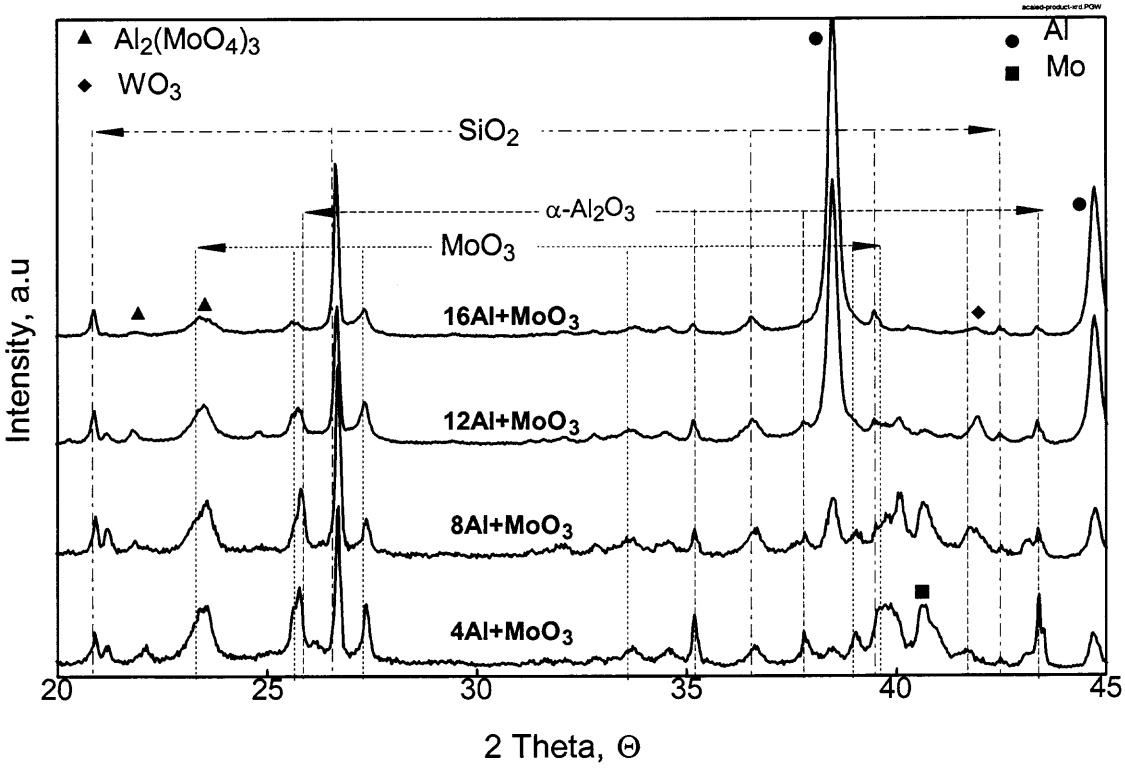

Figure 5.12 XRD patterns of CVE combustion products of different nanocomposite powders.

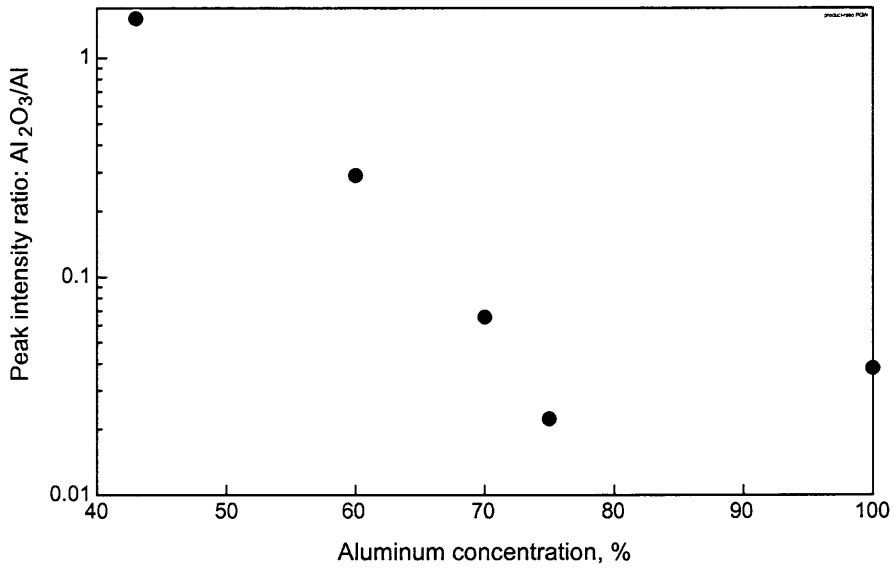

Figure 5.13 Results of XRD analysis of combustion products collected in CVE experiments: intensity ratios for peaks of Al_2O_3 and Al.

5.6 Conclusions

Fuel rich Al-MoO_3 nanocomposites with varying compositions have been synthesized. Uniform mixing of MoO_3 nano-domains in Al matrix is achieved for all samples. Particle size of the nanocomposite powders increases with increase in aluminum concentration. Thermal analysis showed that exothermic processes start when the nanocomposite powders are heated to only about 350 K. Multiple and overlapping exothermic processes are observed and further work is needed to understand the reaction mechanisms in these materials. At the heating rates varied in the range of 3000 – 30000 K/s, all nanocomposite powders ignite at temperatures well below the Al melting point. Ignition temperatures of samples containing 4, 8, and 12 moles of Al per mole of MoO_3 are similar and lower than those of the sample containing 16 moles of Al. It is noted that for the former set of samples, the ignition mechanism changes as the heating rate increases. Based on the current measurements, it is estimated that the nanocomposite

powder with the bulk composition $16Al+MoO_3$ will ignite at about 1160 K when heated at a rate of 10^6 K/s, typically occurring in fuel-air explosions. The nanocomposite powders with lower aluminum concentrations are expected to ignite at an even lower temperature, of about 910 K, when heated at 10^6 K/s. Constant volume explosion experiments indicate that the flames produced by nanocomposite thermite powders in air propagate much faster than those produced by pure Al powder. The maximum rate of pressure rise indicative of the highest burn rate was measured for the $8Al+MoO_3$ nanocomposite powder. Maximum reaction pressure indicative of the overall combustion energy is highest for pure Al, closely followed by that for $8Al+MoO_3$ and followed by those for the $12Al+MoO_3$ and $4Al+MoO_3$ nanocomposite powders. The reaction energy normalized per unit mass of aluminum is the highest for nanocomposite materials with bulk compositions $4Al+MoO_3$ and $8Al+MoO_3$ and lowest for pure Al and for the $16Al+MoO_3$ nanocomposite sample. This reduced efficiency of combustion inferred from the measured pressure traces correlates with the analyzed combustion products, containing respectively greater amounts of unreacted aluminum. It is suggested that a reduced efficiency of combustion for very aluminum-rich nanocomposite powders is explained by relatively coarse particle sizes obtained for these materials.

CHAPTER 6

KINETICS OF SOLID STATE REDUCTION-OXIDATION REACTIONS: FAILURE OF ISOCONVERSION APPROACH

6.1 Introduction

Thermal analysis became a ubiquitous tool for characterization of various solid state reactions. Most of the related scientific studies report results in terms of specific activation energies for specific transformations. An increasing number of practically motivated and engineering publications interpret the results with the goal to determine stability or aging characteristics of materials of interest. The most widely used approach to interpret thermal analysis results in both cases is based on model-free isoconversion methods. A number of variations to isoconversion analysis have been developed. A critical comparison was given by Starink (2003) [72]. Several software implementations are available commercially [73-74]. The activation energy is treated as a parameter of the degree of transformation, α, and the Arrhenius formalism is developed to match the differential thermal analysis (DTA/DSC) or thermo-gravimetric (TG) curves collected at several heating rates. Once the match is achieved, the same formalism is used to predict the material behavior under varying environmental conditions generally characterized by lower heating rates. Recently, with development of novel reactive nanomaterials, especially those employing thermite reactions [4 - 22], it became of significant interest to expand the kinetics information inferred from thermal analysis to much higher heating rates in order to quantify ignition kinetics for such materials. While the advantages of model-free processing appear to be significant for some practical implementations [55, 75 -77], the concept of variable activation energy has been seriously criticized [78]. It has

been suggested that development of true reaction models, i.e., including concurrent processes with specific activation energies offers more benefits in the long run and reduces errors resulting from the inappropriate applications of the model-free processing. Indeed, such processing, can only be adequately applied for independent, well-resolved reactions when the experimental baseline is unambiguously established. Unfortunately, such cases are rare in solid state reactions and the experimental results of thermal analysis need to be carefully examined before an isoconversion approach is used.

This paper presents an example of a solid-state reaction for which any of the generally used isoconversion approaches fail. The DSC measurements are reported and initially processed by the Kissinger peak method [51]. The resulting reaction kinetics and respective activation energies are of significant practical interest, but are determined with unacceptably low accuracy. An attempt to model the experimental DSC results by a series of independent processes is shown to fail. Additional experiments demonstrate clearly that the isoconversion approach represented by either simple calculation or advanced, software-based mathematical processing is unacceptable for this reaction. It is concluded that development of a reaction model is imperative for practical interpretation of the respective DSC results.

The specific solid state reaction of interest to this study is a reduction-oxidation reaction of Al with MoO_3. The reaction is studied for fully dense nanocomposite powders with a composition $4Al+MoO_3$ (with excess Al over the stoichiometric composition) produced by arrested reactive milling (ARM). Detailed description of synthesis of reactive nanocomposite powders by ARM is available elsewhere [18 - 22]. The material used in this study and other similar nanocomposite materials are being

currently developed for advanced reactive formulations to be used in propellants, explosives, and pyrotechnics [18-22].

6.2 Materials

Nanocomposite powders were prepared using a shaker mill (8000 series by Spex Certiprep) with flat-ended steel vials and 5 mm diameter steel milling balls. Powders of elemental aluminum (99% pure, -325 mesh by Alfa Aesar) and molybdenum trioxide MoO_3 (99.95% pure, by Alfa Aesar) were blended in the required proportion. Batches of 5 g were milled under argon and with 4 ml of hexane (C_6H_{14}) as process control agent (PCA) to inhibit cold welding and prevent reaction of Al with MoO_3 during milling. A constant milling time of 30 min was used. The product powders had particle sizes in the range of 1 – 200 μm. Each particle consisted of an aluminum matrix with embedded nano-inclusions of MoO_3. An example of a cross-section is shown in Figure 6.1.

Previous work [79] has shown that the general sequence of reactions in such material includes decomposition of MoO_3 into MoO_2 and O and diffusion of oxygen ions to Al through layers of different polymorphs of Al_2O_3 and possibly through MoO_2. At higher temperatures, formation of ternary oxides, Al_2MoO_6 was observed [79].

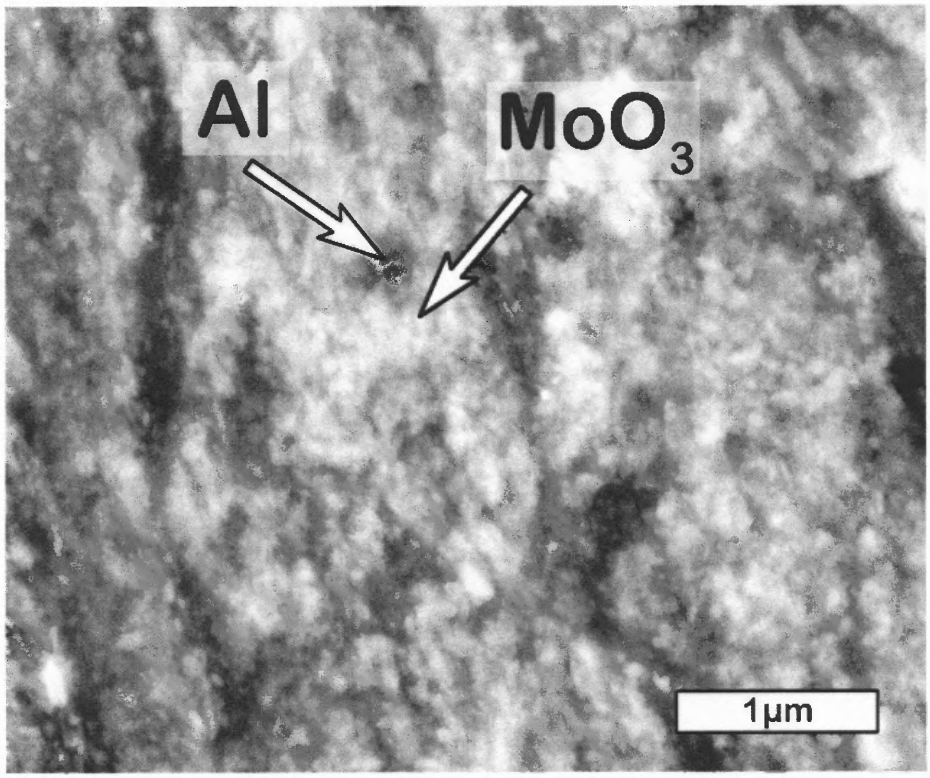

Figure 6.1 Backscattered electron image of the cross-section of an Al-MoO_3 nanocomposite. Brighter areas correspond to MoO_3, and darker areas are Al.

6.3 Thermal Analysis

Reactions in the nanocomposite powders at elevated temperatures were studied by differential scanning calorimetry (DSC) using a Netzsch Simultaneous Thermal Analyzer STA409 PC. Alumina pans were used and the furnace was flushed with argon at approximately 50 ml/min. DSC traces were recorded between room temperature and 1200 K with heating rates varying from 1 to 40 K/min. At 1200 K, the samples were held for 30 min, and then cooled to room temperature. In order to establish a useful baseline, the reacted samples were than heated again to 1200 K. The temperature sensor of the DSC was calibrated with a set of high-purity standards; the temperature measurements are estimated to be accurate within ±1 K.

The results of the DSC measurements for a set of heating rates are shown in Figure 6.2. The traces show a series of overlapping exothermic peaks. Initial exothermic events starting at ~400 K are difficult to separate. These features are followed by stronger and more easily identifiable peaks in the 800 – 950 K temperature range. In addition to the expected shift to higher temperatures at higher heating rates, the shapes of the observed peaks change substantially. For example, a relatively strong peak observed between 600 and 700 K at the lowest heating rates can hardly be detected when heating rates exceed 5 K/min.

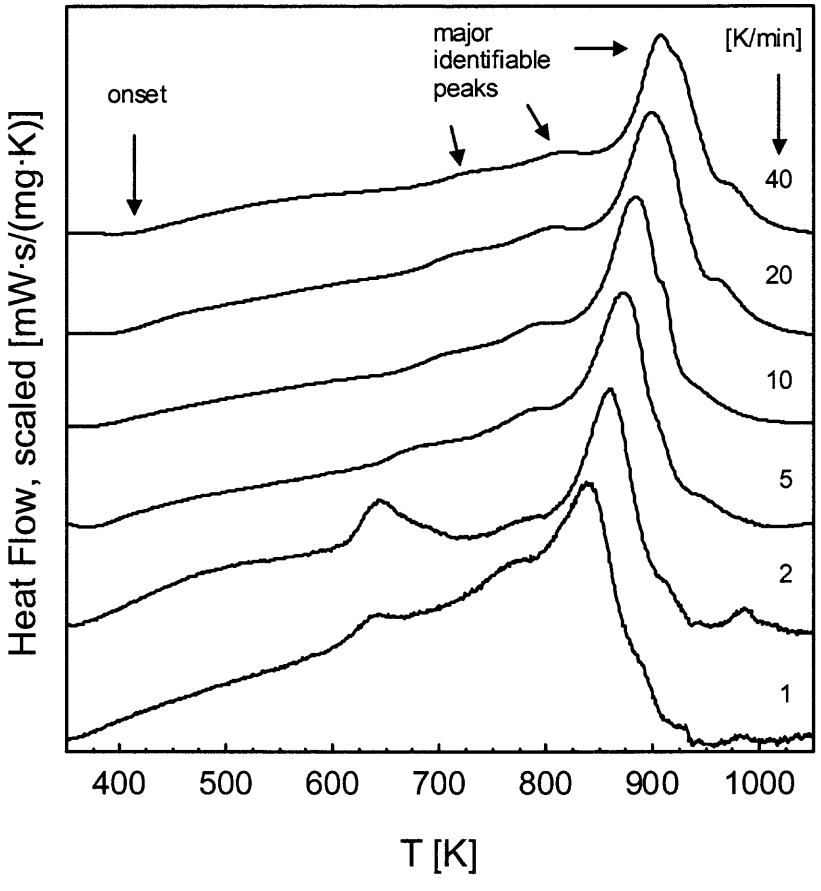

Figure 6.2 Baseline-corrected DSC traces collected for nanocomposite powder with bulk composition 4 Al + MoO_3 at heating rates ranging from 1 to 40 K/min.

6.4 Data Processing

In an initial attempt to separate DSC peaks, and to assign an individual activation energy to each process, apparent peak maxima were used to process the data according to Kissinger's method [51]. The Kissinger formalism states that

$$\ln\left(\frac{\beta}{T_p^2}\right) = -\frac{E}{RT_p} + C \tag{6.1}$$

where β is the heating rate, T_p the temperature of the peak maximum, E is the activation energy of the process, and R is the universal gas constant. A plot of the left hand side (LHS) of equation (1) vs. the reciprocal peak temperature should yield a straight line with the slope of E/R. The constant C is regarded as specific to the reaction mechanism, and need not be further specified. To apply this method, peak positions have to be identified. As can be seen in Figure 6.2, only the peak in the 800 – 900 K range can be tracked throughout all measurements. In order to be able to estimate the activation energy for the other identifiable features in the measurements, different reference points were used as approximations. The onset point of the overall heat effect was used, as well as the inflection point of the minor peak in the 600 – 700 K range. Figure 6.3 shows the results. It is evident that within these few measurements, some apparent outliers exist, and that the data points therefore can not be described by straight line fits. Results that are qualitatively similar have been reported in other publications on energetic composites [16, 80-82]. Additional experiments in smaller heating rate increments suggest that such outliers consistently form a trend, rather than represent the reproducibility of the experiment. These measurements should be regarded with caution, and more detailed measurements are needed.

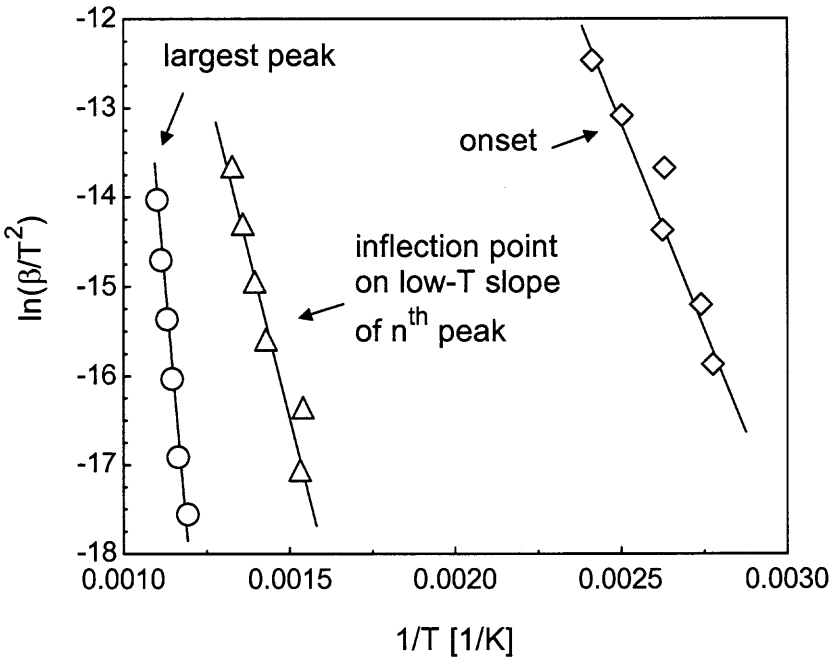

Figure 6.3 Data processed according to the Kissinger peak position method. Heating rates used were 1, 2, 5, 10, 20, and 40 K/min.

Since simple peak processing leads to the conclusion that individual peaks can not be assigned unique activation energy values, it was next attempted to determine the activation energy as a function of reaction progress according to various isoconversion formalisms [76]. In all these methods, the reaction progress, α, is determined at a number of different heating rates by integration of the heat flow Φ over time. This requires a reliable determination of the baseline of the measurements. Despite the experimental procedure outlined above, the signal at the end of the measurement ($T >$ 1000 K) did not always return to zero, indicating that the baseline correction was not complete. This is most likely due to slight changes in the physical parameters of the sample that affect heat transfer, such as shrinkage or decrease in porosity. A synthetic baseline Φ_{BL} was then constructed by taking the weighted average between the heat flow at the beginning (Φ_i) and the end (Φ_f) of the experiment with α as the weighing factor:

$$\Phi_{BL} = (1-\alpha)\cdot\Phi_i + \alpha\cdot\Phi_f \tag{6.2}$$

This baseline was subtracted from the measured heat flow, and finally a was calculated by integration:

$$\alpha(t) = \frac{1}{Q}\int_{t_0}^{t}\Phi(u) - \Phi_{BL}(u)du \tag{6.3}$$

Since the baseline depends on α while α depends on the baseline, α was calculated iteratively. The initial baseline was taken as a straight line between starting and end points; subsequently the value of α converged after 3-4 iterations.

Isoconversion methods can be classified in two main categories. The Ozawa-Flynn-Wall, Generalized Kissinger, and Starink's methods are examples of isoconversion methods that rely on the approximation of the so-called temperature integral [76, and references therein]. Of these examples, Starink's method is the most accurate [76]. It uses the following equation:

$$\ln\left(\frac{\beta}{T_\alpha^{1.92}}\right) = -1.008\frac{E}{RT_\alpha} + C \tag{6.4}$$

where T_α is the temperature corresponding to a specific degree of conversion. By plotting the LHS of equation 4 vs. 1/T for fixed values of α, the activation energy can be determined as a function of α.

Other methods do not rely on any approximation, but instead use the measured heat flow directly. An example is the Friedman method:

$$\ln\left(\frac{d\alpha}{dt}\right) = -\frac{E}{RT_\alpha} + C \tag{6.5}$$

where explicit knowledge of the heating rate β is not required. Figure 6.4 shows plots of the LHS of equations 4 and 5 vs. 1/T. In both plots, the contours of constant reaction progress can not reasonably be described by straight lines. In particular, the deviations at low heating rates are strong, reproducible, and form consistent trends over a range of heating rates. This strongly suggests that at least over the range of heating rates investigated, a single activation energy can not be assigned to a specific degree of reaction progress. Instead, overlapping reactions that likely depend on each other, must be considered in order to successfully model the observed DSC measurements. It is worth pointing out that mechanical application of these isoconversion methods gives apparently very similar and consistent results, as illustrated in Figure 6.5. This is clearly deceptive if the poor linear fit in Figure 6.4 is considered.

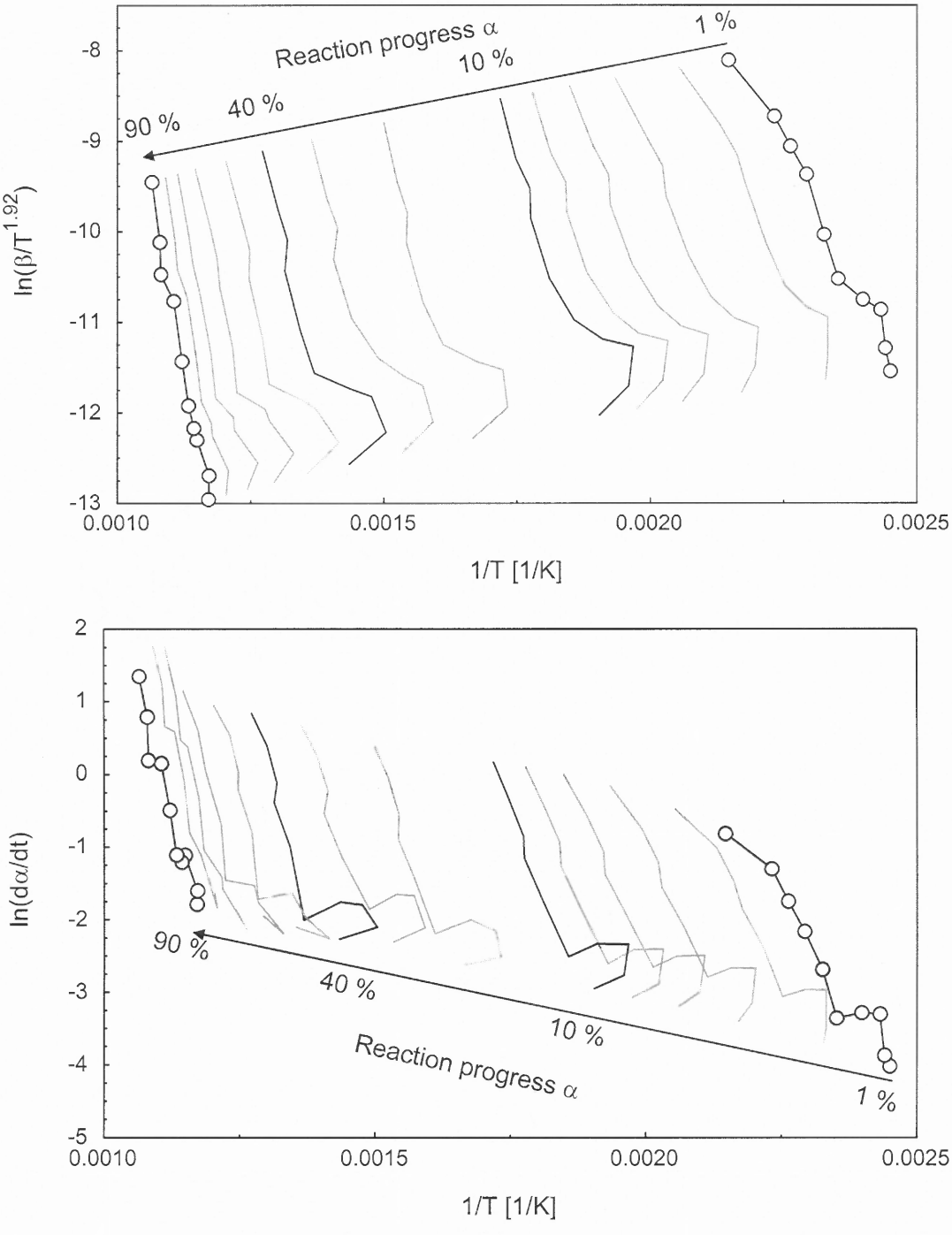

Figure 6.4 Isoconversion processing of DSC measurements to determine the activation energy as a function of the reaction completeness Top: Starink, Bottom: Friedman.

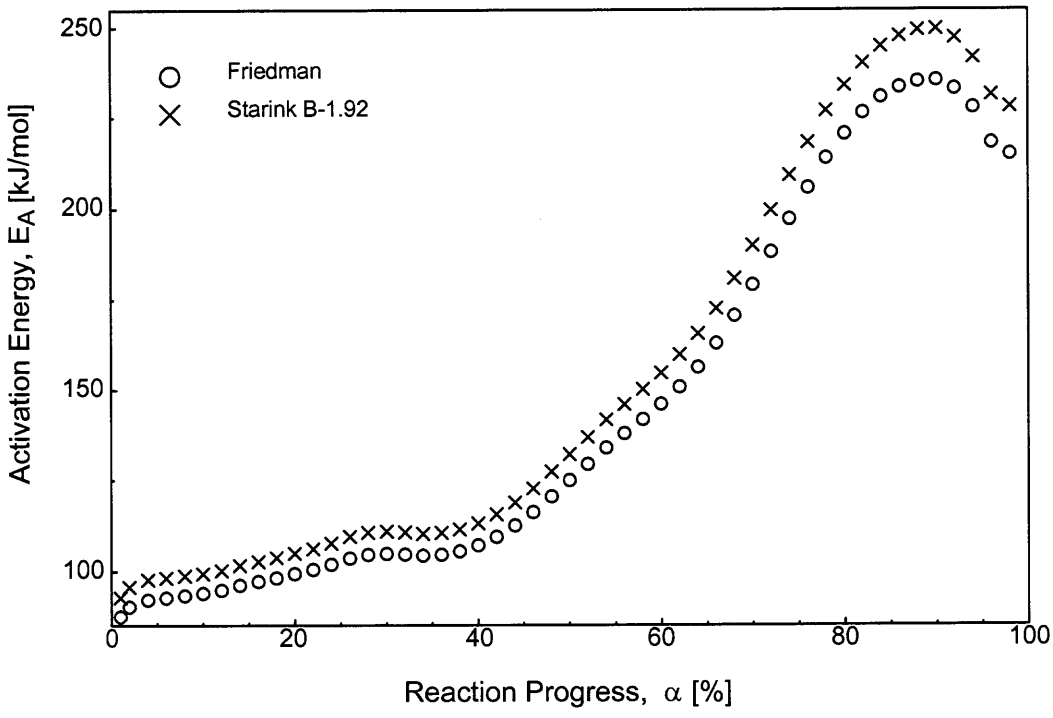

Figure 6.5 Activation energy as a function of reaction progress as determined by Friedman's and Starink's isoconversion methods.

6.5 Conclusions

Analysis of exothermic reactions in Al-MoO_3 system shows that kinetics of such reactions cannot be meaningfully determined by isoconversion processing. The data processing shows that activation energy cannot be meaningfully determined as a function of reaction progress, as would be required for any type of model-free processing. In this case, which is expected to represent a rather common situation, more measurements at different heating rates are needed to identify trends, and a detailed model development is necessary for meaningful description of the reaction kinetics.

CHAPTER 7

SYNTHESIS AND CHARACTERIZATION OF SODIUM-NITRATE BASED REACTIVE COMPOSITES

7.1 Introduction

Sodium nitrate is known as an active oxidizer for its ability to generate gas [83, 84], and optical emission properties useful for applications in pyrotechnic formulations [85, 86]. The reactions of this oxidizer with metallic fuels, e.g., Al and Mg [87, 88] are of particular interest. Mixing sodium nitrate with metallic fuel is typically associated with the risk of self-ignition, so that fairly large particle sizes are used in most practical applications [89, 90]. At the same time, improved combustion characteristics were reported when reduced size powders were used [91, 92]. Recently, several types of reactive nanocomposites were prepared using Arrested Reactive Milling (ARM), a technique based on high energy mechanical milling of starting components [18, 22]. This preparation technique enables fine mixing and produces highly developed reactive interfaces between the components, which result in enhanced reaction rates. ARM is a modification of reactive milling [38], in which a blend of powders capable of an exothermic reaction is ball-milled. If the reaction enthalpy is sufficiently high, a self-sustained reaction is triggered mechanically after a certain milling time. The products are no longer reactive. In ARM, highly reactive nanocomposite powders are formed as a result of arresting (or stopping) the milling process prior to the initiation of the self-sustained reaction. In this work, three metallic powders, including aluminum, magnesium, and mechanically alloyed $Al_{0.5}Mg_{0.5}$ [14, 15] have been used as fuels to prepare composites with $NaNO_3$ as an oxidizer using ARM. X-ray diffraction, electron

microscopy, and thermal analysis were used to characterize the prepared materials. In addition, ignition tests using an electrically heated filament were conducted to determine their ignition kinetics. Combustion tests in air were also performed and the emission spectra were measured. The results of this investigation are reported.

7.2 Materials

Starting blends were prepared from sodium nitrate (99%, Alfa Aesar), magnesium (99.8 %, 50 - 100 mesh, Atlantic Equipment Engineers), aluminum (99.9%, -325 mesh, Atlantic Equipment Engineers). Mechanically alloyed powder with the composition $Al_{0.5}Mg_{0.5}$ was prepared using a Retsch 400 PM planetary mill, according to methodology described in detail in Ref. [26]. The average particle size of the mechanically alloyed powder was 20-30 μm [26].

The bulk compositions of the prepared composite materials were stoichiometric, targeting the complete oxidation of the respective fuel component, and leaving nitrogen as the only gaseous reaction product. Compositions of the individual components are listed in Table 7.1.

Table 7.1 Bulk Compositions and Component Mass Fractions for Composite Powders

Composition	Mass fraction [%]	
	Metal	Sodium Nitrate
5 Mg + 2 $NaNO_3$	41.7	58.3
5 Al + 3 $NaNO_3$	34.6	65.4
2 $Al_{0.5}Mg_{0.5}$ + $NaNO_3$	38.1	61.8

7.3 Experimental

7.3.1 Synthesis of Reactive Composite Powders

Composite powders were synthesized by Arrested Reactive Milling using a Retsch 400 PM planetary mill. The rotation speed was set to 350 RPM. The mill was set to reverse the direction of rotation every 15 min. Powders were milled in custom made steel jars suitable for high pressure applications (ID Ø 64 mm × 52 mm, 18 mm wall thickness), using 9.53 mm balls made of AISI/SAE 1013 low-carbon steel. In addition, the mill was equipped with an air conditioner which maintained the ambient temperature at 10 ± 4 °C. To monitor the processing temperature, the milling jars were equipped with wireless temperature sensors (Point Temperature Sensors including 418 MHz transmitters by Point Six Wireless, Inc.). Thermistors were embedded in aluminum plates which were placed on top of each jar. The transmitters were mounted on the clamps holding the milling jars in place. Milling temperature was monitored using a receiver connected to a personal computer-based multi-channel data logger. Measured temperatures of the milling jars were in the range of 12- 20 °C.

Synthesis was carried out in argon environment. For each composite several 20 g batches were synthesized with a ball to powder ratio (BPR) of 5. Preliminary experiments were carried out to determine the time when self-sustained exothermic reaction is mechanically triggered. The composites were milled with no additives as follows: Al + $NaNO_3$ -145 min, Mg + $NaNO_3$ -124 min and $Al_{0.5}Mg_{0.5}$ + $NaNO_3$ - 26 min. For safety and ease of handling of the prepared reactive composites, 25 ml of hexane was added into each milling jar, also under argon. This was followed by a brief 5-min period of wet milling, which was intended to break loose agglomerates, and did not affect the

structure of the prepared composites. To prevent slow reaction of the respective metal component with atmospheric oxygen, the samples were stored under hexane as well.

7.3.2 Sample Characterization

Morphology and composition of the reactive composites were examined on a SEM (LEO 1530 Field Emission Scanning Electron Microscope) operated at 10 kV. The samples were cross-sectioned for examination. Powder samples were embedded in epoxy and polished using SiC paper and kerosene. Special care was taken not to overheat the samples during polishing to avoid inducing the reaction in the produced composite particles. The phase composition was verified for each composite by x-ray powder diffraction (XRD). The XRD was performed on a Phillips X'pert MRD powder diffractometer operated at 45 kV and 45 mA using Cu Kα radiation (λ = 1.5438 A).

Differential thermal analysis (DTA) was performed simultaneously with thermogravimetry (TG) using a Netzsch Simultaneous Thermal Analyzer STA409 PC. Alumina crucibles were used and the furnace was flushed with argon at approximately 10 ml/min. To avoid exposing the material to air during loading of the crucibles, the samples were introduced as a slurry in excess hexane, the thermal analyzer's furnace was closed and vigorously flushed with Argon until the hexane evaporated, and the analyzer's internal balance was used to determine the initial sample mass.

DTA and TG traces were recorded between room temperature and 973 K with heating rates of 1 and 5 K/min. Higher heating rates were avoided in order to prevent accidental ignition within the STA. At the same time, measurements at heating rates lower than 1 K/min were not feasible due to long-term stability issues of the measurement setup. The weight of the sample for DTA and TG measurements was

selected to be 10-15 mg. However, a smaller, 0.7-1 mg sample of $Al_{0.5}Mg_{0.5}$-$NaNO_3$ nanocomposite was also used to avoid ignition, as described below. The temperature of the DTA was calibrated using the known melting points of a set of metal standards. The temperature is accurate within ±1 K.

In addition to thermal analysis, a preliminary investigation of ignition at high heating rates in the range 10^2-10^4 K/s was conducted. The reactive powder was coated on an electrically heated Nichrome filament. The temperature of the filament was monitored with an infrared pyrometer. Light emission from the powder coating was detected by a photodiode. A sharp onset of the light emission was taken as evidence of ignition. The setup is illustrated in Figure 2.3; in Chapter 2 (Section 2.4.4). The relation of thermal analysis and filament ignition experiments will be discussed further below.

7.3.3 Spectral Emission of Combustion of the Composite Powders

Since the composites studied here are of interest as pyrotechnic materials, initial characterization of the spectral emission of the combustion of prepared composite powders has been performed as a point of reference. Spectra were collected using the experimental setup shown in Figure 7.1. The powder to be tested was placed on a 7.5×7.5×1.0 cm aluminum plate and formed a 50 mm-long rectangle with the height of 1 mm and width of 1.2 mm. The light was collected from a cylindrical volume of 10±0.3mm diameter, just above the powder surface. The axis of the cylindrical volume was horizontal, parallel to the rectangle's axis, and lifted approximately 5 mm above the aluminum plate. All spectra were taken with a spectrometer integration time of 4 ms. The exposure was adjusted by changing the opening of the iris aperture.

The intensity calibration of the spectrometer has been performed at the same integration time value as that used for the measurements. A NIST-traceable tungsten strip-lamp RSL2000 by the Pyrometer Instrument Co., Inc. was used as a light source. The lamp manufacturer's data on the brightness temperature of the tungsten ribbon versus DC current was used. The tungsten spectral emissivities at different temperatures from ref. [93] were used to calculate both the real temperatures of the tungsten ribbon based on its brightness temperatures and the respective normal spectral intensities $I_\lambda(\lambda, T)$ of the tungsten ribbon at the temperatures used for calibration.

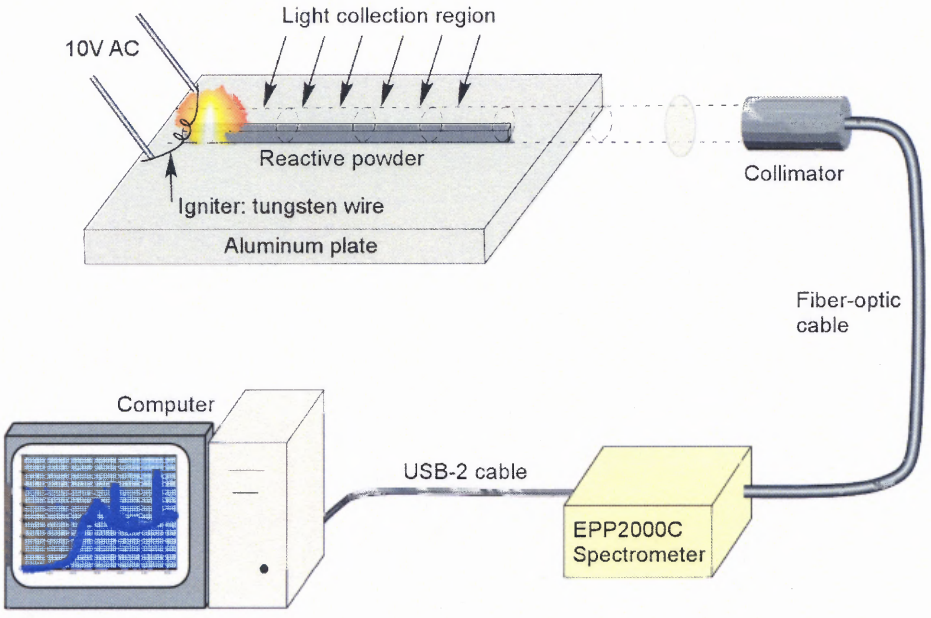

Figure 7.1 Experimental setup for the evaluation of light emission from combustion of the prepared composite powders.

7.4 Results and Discussion

7.4.1 Morphology and Structure

All produced powders examined under SEM showed the presence of composite particles as well as mixed powders of the starting materials. SEM images of the produced

composite powders are shown in Figure 7.2. Both Al and Mg powders form flakes sandwiched with particles of $NaNO_3$. The average thickness of Mg flakes is greater than that of Al, which could be explained by slightly higher hardness (Brinell) of Mg metal as compared to Al [94]. The composite particles made with the mechanically alloyed Al-Mg powder appear different. No flakes were formed; instead, three-dimensional composite particles were observed. It also appeared that the interface between metal and oxidizer was larger for the mechanically alloyed powder as compared to either of the pure metal powders.

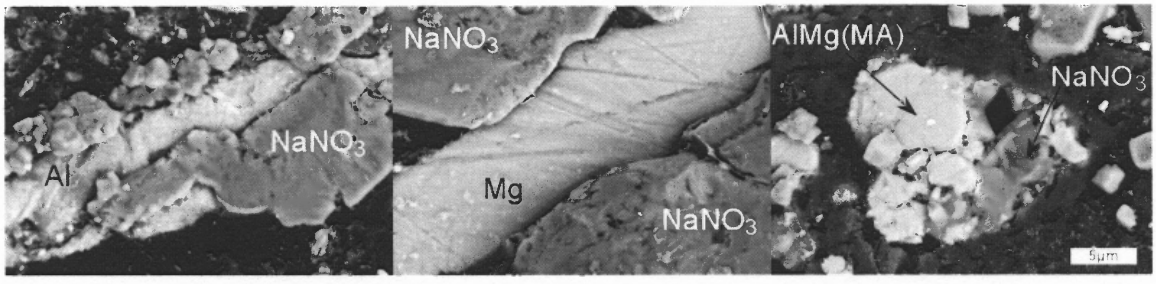

Figure 7.2 Backscattered SEM images of the Al-$NaNO_3$, Mg-$NaNO_3$, $Al_{0.5}Mg_{0.5}$-$NaNO_3$ composites.

X-ray diffraction patterns collected for all three prepared composites are shown in Figure 7.4. For both samples prepared with the pure metal powders, peaks corresponding to NaNO3 and respective metal component were clearly observed. For the sample prepared using mechanically alloyed powder, peaks of NaNO3 appear together with the characteristic XRD pattern of the mechanical alloy in which a broad peak of the Al-Mg γ phase ($Al_{12}Mg_{17}$) can be distinguished [25]. The specially marked broad peak between 36-38°, in the $Al_{0.5}Mg_{0.5}$-$NaNO_3$ XRD pattern belongs to the $Al_{12}Mg_{17}$ intermetallic.

For all three materials, the preparation of composites did not affect the XRD patterns of the starting components and, therefore, the crystal structures of the components.

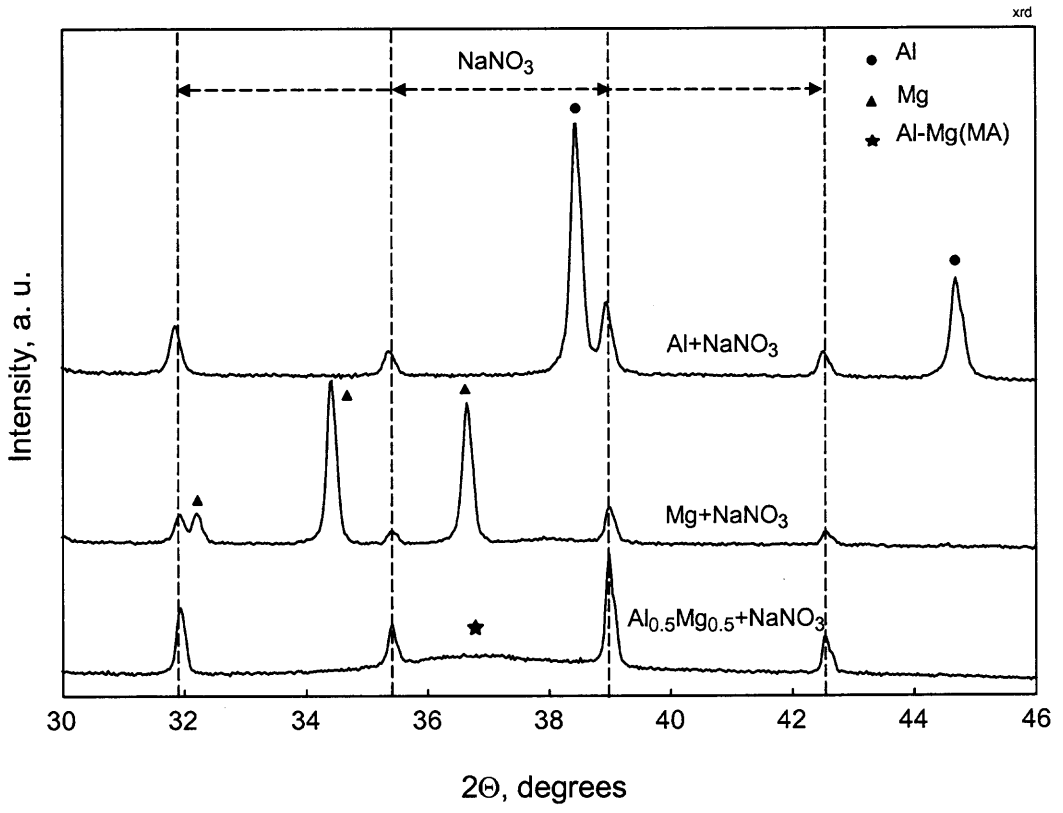

Figure 7.3 XRD patterns of the Al-$NaNO_3$, Mg-$NaNO_3$ and $Al_{0.5}Mg_{0.5}$-$NaNO_3$ nanocomposites.

7.4.2 Thermal Analysis

Differential thermal analysis and simultaneous thermogravimetric analysis was performed on all three prepared samples of composite powders. Figures 7.4 – 7.6 show DTA and TG traces recorded as each of the powders was heated in argon from room temperature to 973 K at 1 K/min and 5 K/min.

Sodium nitrate melts at 573 K (not shown), reasonably close to 580 K, the melting point reported in the literature [95, 96]. Melting can also be clearly seen in the DTA traces of Al-$NaNO_3$ (Figure 7.4) and $Al_{0.5}Mg_{0.5}$-$NaNO_3$ composites (Figure 7.6). However, it is barely distinguishable for the Mg-$NaNO_3$ composite powder (Figure 7.5), possibly due to overlap with simultaneous decomposition of the nitrate and oxidation of

Mg. The melting of sodium nitrate is observed to start at somewhat lower temperatures for the composite powders: melting onset is observed at 559 K and at 568 K for Al-$NaNO_3$ and Al-Mg-$NaNO_3$ composites, respectively.

The TG trace for pure $NaNO_3$ is nearly constant up to 845 K, while at higher temperatures a rapid weight decrease indicates decomposition of the material. This behavior is consistent with the decomposition temperature for sodium nitrate reported in the literature [96]. According to mass spectrometric measurements [96], the first decomposition step of $NaNO_3$ results in the evolution of oxygen gas and the formation of sodium nitrite, $NaNO_2$. Only at temperatures above 1050 K does the nitrite decompose accompanied by the release of NO_2 gas.

For the composite powders, the decomposition of sodium nitrate starts at significantly lower temperatures, as indicated by the respective TG traces in Figures. 7.4-7.6. For the purpose of evaluation of the observed weight changes, the following bulk reaction will be considered:

$$x\,M + 2y\,NaNO_3 \rightarrow M_xO_{5y} + y\,Na_2O + y\,N_2 \qquad (7.1)$$

where M indicates Al, Mg, or the mechanically alloyed material. This reaction assumes that the decomposition of the nitrite, resulting in the removal of NO_2 gas, is immediately followed by the quantitative reduction of NO_2 by the respective metal, although that may or may not actually occur in the experiments. With this assumption, the observed weight loss indicates the reaction progress directly, as nitrogen gas is the only volatile species. As a benchmark, all investigated compositions contain approximately 10 wt-% N_2 gas.

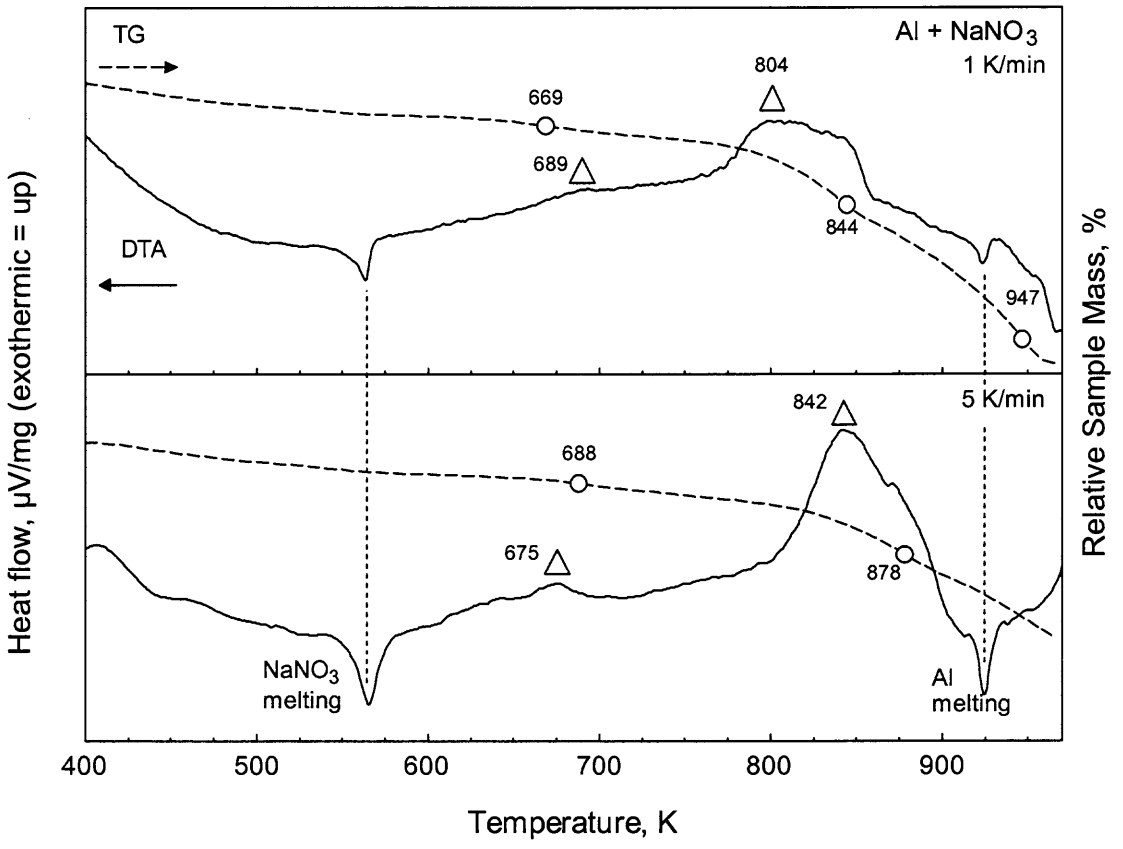

Figure 7.4 DTA and TG traces for an Al-$NaNO_3$, composite heated in argon at 1 K/min, and 5 K/min, respectively.

For the Al-$NaNO_3$ composite, the weight of the sample decreases gradually, starting at about 400 K (see Figure 7.4). Several inflection points are detected in the TG signal, indicating distinct reaction steps. At a heating rate of 5 K/min, a TG step occurs at ~690 K near a diffuse exothermic peak in the DTA signal. Although the observed steps overlap, and are difficult to rigorously separate, it can be stated that the weight has decreased by about 5 % as the temperature approaches 800 K. At ~810 K, the onset of an exothermic peak is observed in the DTA signal, accompanied by further, more rapid weight loss. After this peak, an endothermic peak indicates the melting of residual aluminum at 919 K, and the sample weight continues to decrease. At the highest temperature reached in the experiment, the weight has decreased by approximately 17 %.

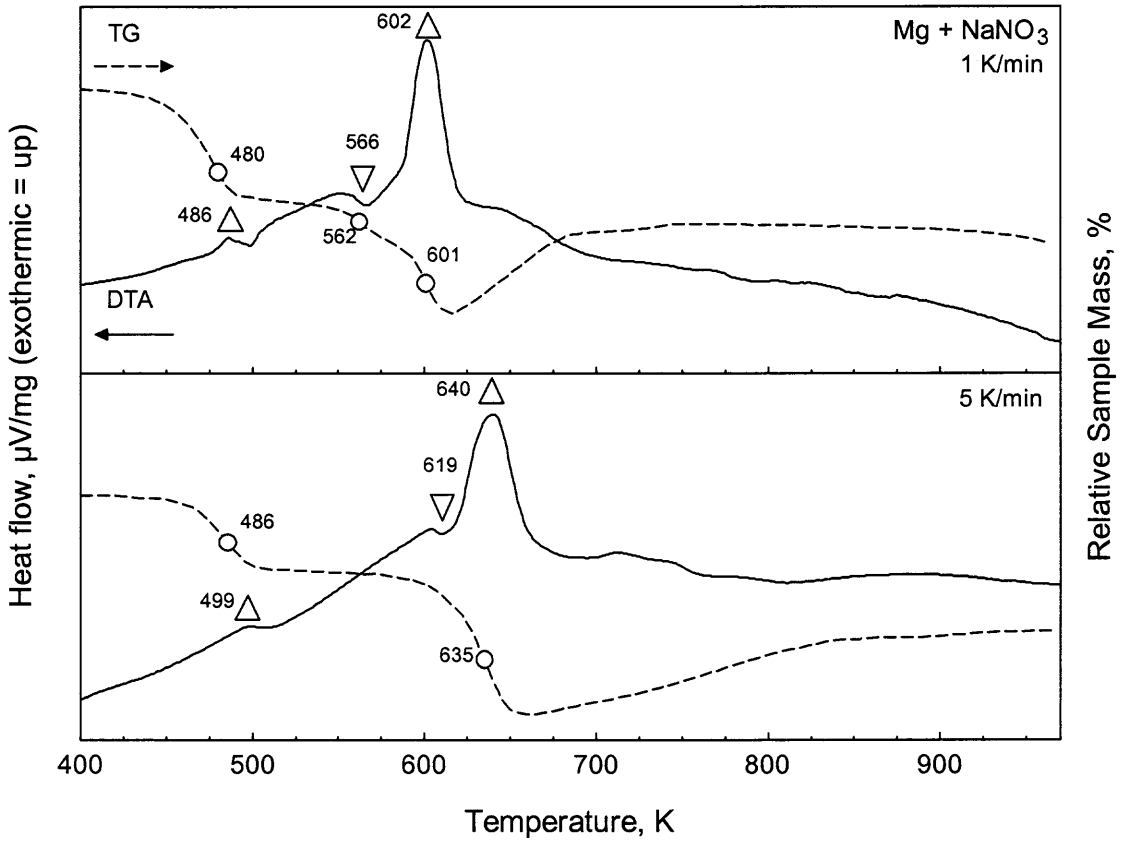

Figure 7.5 DTA and TG traces for an Mg-$NaNO_3$, composite heated in argon at 1 K/min, and 5 K/min, respectively.

The weight loss of the Mg-$NaNO_3$ composite occurs in several distinct steps, as shown in Figure 7.5. The first step starts at ~450 K, and the weight decreases by approximately 4.5 %. The highest rate of weight loss is observed at 480 K. While a complex feature is observed in the DTA signal between 480 and 500 K, its relation to the weight loss is not yet clear. After this initial weight loss, a second, complex step is observed over the temperature range 550 to 610 K. The presence of two distinct inflection points in the TG trace at 562 K and 601 K, distinguishable only for the heating rate of 1 K/min, indicates that at least two processes contribute to the feature. The DTA signal shows a weak endothermic peak with a peak temperature of 566 K and a stronger exothermic peak with a peak temperature of 602 K. This suggests that the reaction

started by decomposition of $NaNO_3$, and is followed by oxidation of the Mg component. By the end of the exothermic peak, the sample has lost approximately 9.0 % of its initial mass. This is however followed by a distinct mass increase over the temperature interval ~610 K – 690 K. It is suggested that the initial weight loss represents the evolution of NO_2 gas, part of which remains in the vicinity of the sample and subsequently oxidizes the Mg metal further, while producing N_2 gas. The final weight loss is approximately 5.5 %, which corresponds to a reaction progress of roughly 57 % according to Reaction (7.1).

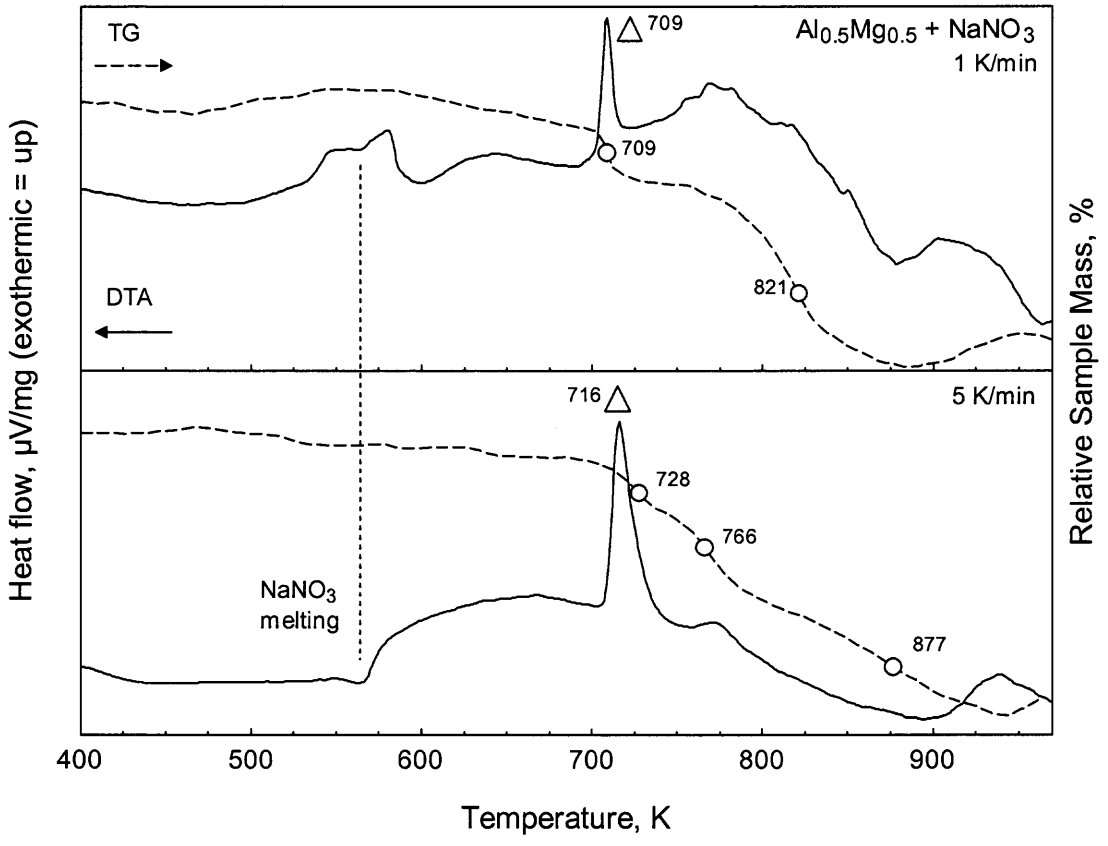

Figure 7.6 DTA and TG traces for an $Al_{0.5}Mg_{0.5}$-$NaNO_3$, composite heated in argon at 1 K/min, and 5 K/min, respectively.

The TG trace for the composite material with mechanically alloyed Al-Mg powder remains relatively constant up to approximately 704 K. Note that the noise level

of the measurement shown in Figure 7.6 is very high due to the small amounts that were used in order to avoid ignition at higher temperatures. The observed small weight loss has been confirmed in separate measurements with larger amounts of material that were heated to max. 700 K.

It can not be decided with certainty whether the apparent exothermic DTA feature between 550 and 600 K corresponds to a physical process, or is an artifact. However, $NaNO_3$ melting is expected to occur in that temperature range, as is clearly detected in the DTA traces at both heating rates. At 704 K, a relatively sharp weight loss is observed, accompanied by a sharp exothermic peak. The observed peak is significantly stronger than the strongest exothermic peaks observed in the DTA traces of the Al-$NaNO_3$ and the Mg-$NaNO_3$ composites. Note that the peak temperature coincides with the temperature of the eutectic between Mg and the Al-Mg γ phase ($Al_{12}Mg_{17}$) [97]. The mass change can be estimated to within 5 – 10 %. Further weight loss occurs up until ~890 K, with a cumulative mass change of 20 – 30 %. These values exceed the total amount of nitrogen present in the sample, and therefore clearly indicate that other components – most likely NO_2 – must have been expelled during the rapid reaction near 708 K.

The DTA and TG experiments conducted at two different heating rates were used to establish the kinetics of the observed metastable processes. Specifically, the kinetics characterizing the strongest exothermic event that could be causing ignition was of interest. The results of the thermal analysis are summarized in Table 2. When applicable, the results were processed using the isoconversion method according to Kissinger [51]. Peak temperatures were determined from the DTA signal as well as from

inflection points of the TG signal unless indicated otherwise. Apparent activation energies were estimated, and are shown in Table 2.

The strong exothermic peak observed for the composite powder with Al-Mg mechanical alloy does not seem to be noticeably affected by the change in the heating rate. As noted, the onset temperature of this peak coincides with a eutectic in the Al-Mg binary system [97]. This and the very high apparent activation energy suggest that the sharp exothermic reaction is triggered by melting processes in the mechanically alloyed component rather than by continuous reaction at the metal/nitrate interface. It is further significant that the simultaneous weight loss is characterized by a much smaller activation energy.

The thermal analysis data indicate that the composite material in which Al-Mg mechanical alloy was used is expected to be most stable during storage and low temperature handling. This conclusion is based on the highest temperature at which the weight loss is observed and on the fact that this temperature does not seem to be affected noticeably by the heating rate.

7.4.3 Ignition

Characteristic changes in the photodiode signal as a function of temperature of the heated wire are shown in Figure 7.7 for different composite powders undergoing ignition in air. The instant of ignition can be identified from the sudden increase in the photodiode signal. These instants are readily identified for both Mg-$NaNO_3$ and $Al_{0.5}Mg_{0.5}$-$NaNO_3$ composites; however, it is more difficult to point out the ignition instant for the case of Al-$NaNO_3$ composite powder, especially at lower heating rates. In such cases, ignition instants were then identified from time derivatives of the photodiode signal. As shown in

Figure 7.7, at the same heating rate, the ignition temperature of the Al+$NaNO_3$ composite is consistently the highest and that of the $Al_{0.5}Mg_{0.5}$+$NaNO_3$ sample is the lowest. This trend was observed for all three heating rates used in these experiments. Results of the ignition experiments performed at different heating rates are summarized in Table 7.3.

Table 7.2 Summary of the Thermal Analysis. Temperatures Correspond to a Heating Rate of 1 K/min

Material	Event	DTA Peak temperature [K]	TG Inflection point [K]	Cumulative weight loss [%]	Activation Energy [kJ/mol]
$NaNO_3$	Melting	574			–
	Decomposition		888 (onset)	28 (at 950 K)	–
Mg+$NaNO_3$	TG step 1		480	4.5	539
	TG step 2		562	–	–
	TG step 3		601	9.1	139
	DTA peak 1, endothermic	566			96
	DTA peak 2, exothermic	602			125
Al+$NaNO_3$	$NaNO_3$ melting	556			–
	TG step 1		668	≈ 5.6	306
	TG step 2		844	≈ 13	278
	TG step 3		947	≈ 24	–
	DTA peak, exothermic	771 (onset)			210
	Al melting	919			–
$Al_{0.5}Mg_{0.5}$+$NaNO_3$	$NaNO_3$ melting	≈ 560			–
	TG step 1		709	≈ 5 – 10	355
	TG step 2		821	≈ 20 – 30	160
	DTA peak, exothermic	709			≈ 1000

* based on the higher heating rates only

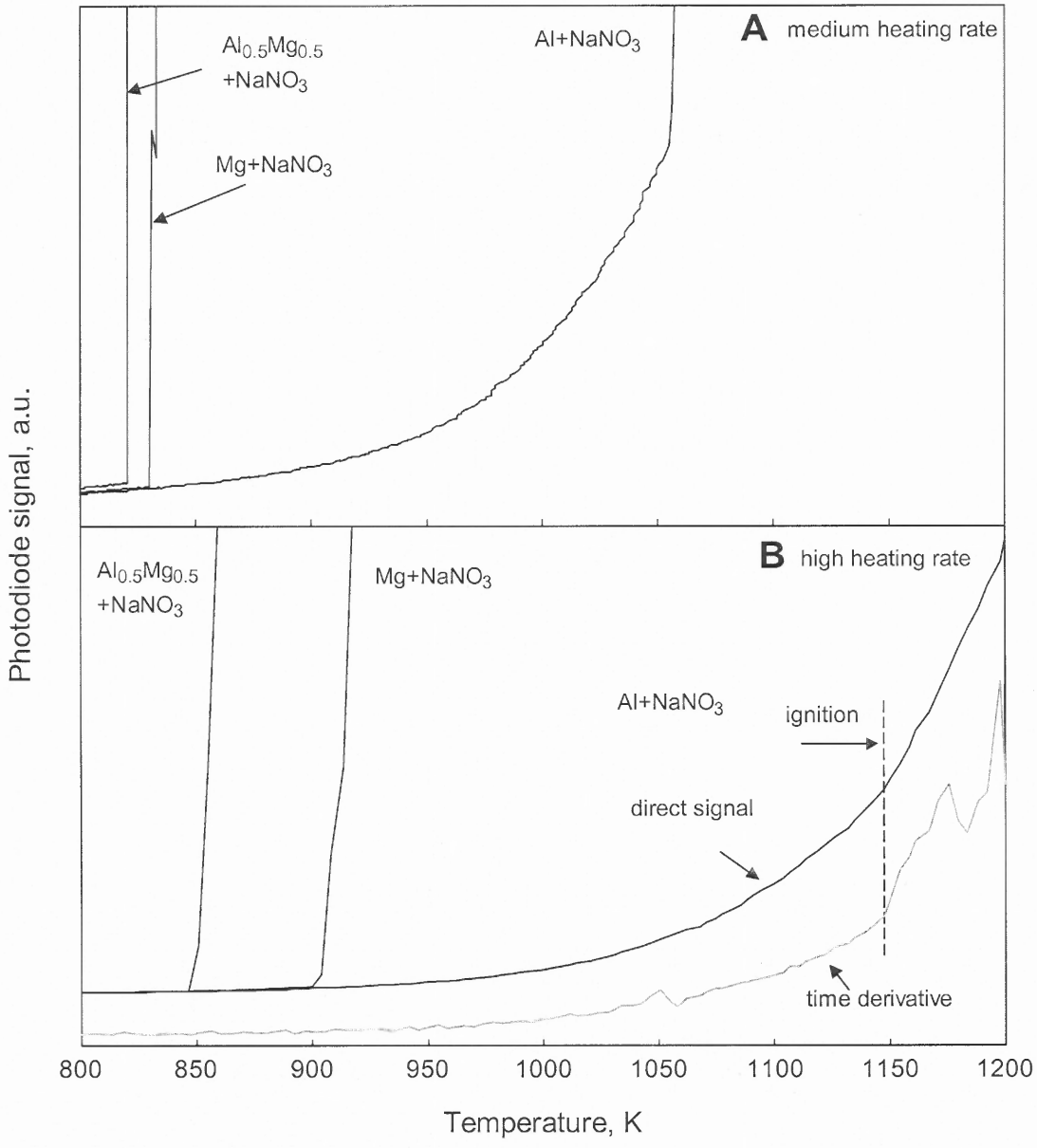

Figure 7.7 Recorded photodiode traces as a function of the simultaneously measured filament temperature for different composite powders undergoing ignition in air. Two heating rates are shown.

A set of measurements was performed in argon in order to determine whether ignition was caused by the reaction of metal fuel with ambient oxygen or with sodium nitrate. The ignition temperatures measured in argon were the same or even lower than those measured in air. Argon, a mono-atomic gas, has a lower thermal conductivity than

air [93], which results in lower heat losses by convection, and consequently in a smaller temperature difference between the powder coating on the heated filament. As a result, less "overheating" of the filament is needed to achieve the same temperature of the powder coating. Thus, the difference in thermal properties of the atmosphere may well explain the lower apparent ignition temperatures observed in argon. The fact that the temperatures measured in argon were never higher than those measured in air allows to conclude that the ignition was always caused by the reaction between metal and sodium nitrate. The ignition results are also plotted together with the results of the thermal analysis in Figure 7.8 in Arrhenius coordinates.

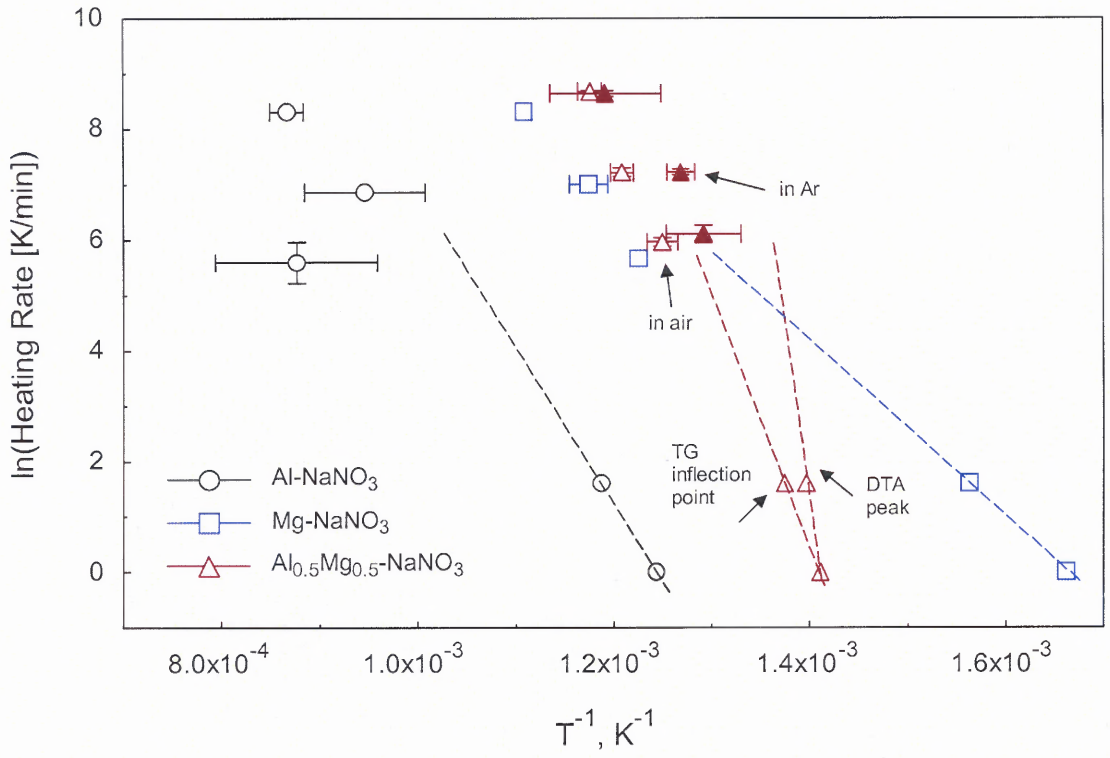

Figure 7.8 Arrhenius plot comparing the results of DTA (low heating rates) and ignition experiments for different $NaNO_3$ based nanocomposites.

The ignition of the Al-$NaNO_3$ composite does not appear to follow an expected trend. The ignition temperature initially decreases as the heating rate is varied from ~10^2

to ~10^3 K/min. In addition, the ignition event at the lower heating rate looks qualitatively different than at higher heating rates, as illustrated in Figure 7.8. The ignition temperatures at the higher heating rates approximately follow the trend projected from the thermal analysis experiments. This suggests that at lower heating rates ignition is caused by a process that has not been detected in the DTA measurements, possibly occurring outside the measurement range.

In the case of the Mg-$NaNO_3$ composite, the overall range of ignition temperatures implied by DTA is in agreement with the experiment. The slight mismatch between observed ignition temperatures and the extrapolation from the thermal analysis may be due to errors in determining the ignition temperatures; more detailed analysis is needed.

For both, the Al-based and the Mg-based composite, the change in heating rate causes the temperatures of the TG inflection points and the DTA peaks to change in a parallel fashion. Thus, both are equally suited to project ignition temperatures to higher heating rates. This is not the case for the $Al_{0.5}Mg_{0.5}$-$NaNO_3$ composite, however. The stepwise mass loss indicated by the 1st TG inflection point (see Table 2, TG step 1) is consistent with the observed ignition temperatures. The DTA peak that accompanies the mass loss does not change significantly with the heating rate. This is consistent with the idea that the reaction at this temperature and at low heating rates is triggered by melting in the alloy. The discrepancy between the released heat (DTA) and the mass loss (TG) indicates that the melting of the alloy is likely not the process triggering ignition at higher heating rates.

Table 7.3 reports activation energies determined independently from the ignition experiments, as opposed to the activation energies determined from thermal analysis, and shown in Table 7.2. The fact that the values determined from the wire ignition experiments are slightly different is likely due to thermal gradients between the heated filament and the powder coating. Indeed, the parallel measurement of ignition temperatures for the $Al_{0.5}Mg_{0.5}$-$NaNO_3$ composite in air and in argon shows that minimizing thermal gradients decreases the apparent activation energy.

Table 7.3 Experimental Heating Rates and Respective Ignition Temperatures for Different Composite Powders. The Shown Ranges Indicate the Experimental Standard Deviations for 6- 10 Measurements for Each Heating Rate Setting

Sample ID	Gas	Heating Rate (K/min)	Ignition Temperature (K)	Estimated activation energy (KJ/mol)
Al+$NaNO_3$	air	4090 ± 120	1154 ± 23	89 ± 36*
		960 ± 30	1057 ± 69	
		270 ± 100	1141 ± 107	
Mg+$NaNO_3$	air	4100 ± 150	902 ± 7	175 ± 19
		1100 ± 70	851 ± 14	
		290 ± 8	816 ± 6	
$Al_{0.5}Mg_{0.5}$+$NaNO_3$	air	5880 ± 70	850 ± 9	245 ± 38
		1360 ± 100	827 ± 8	
		390 ± 30	800 ± 10	
$Al_{0.5}Mg_{0.5}$+$NaNO_3$	argon	5680 ± 270	839 ± 40	128 ± 35
		1370 ± 70	788 ± 9	
		450 ± 70	774 ± 23	

* based on the higher heating rates only

It is interesting that despite the highest thermal stability indicated by the thermal analysis, the $Al_{0.5}Mg_{0.5}$+$NaNO_3$ composite has the lowest ignition temperature, and thus will have the lowest ignition delay as compared to the composites in which pure Mg or Al powders were used.

In a previous thermoanalytical study of pyrotechnic formulations using Al, Mg, and Al-Mg (cast) alloys as fuel and $NaNO_3$ as oxidizer, reaction temperatures were

generally higher [87]. The onset of reaction in the Mg-based formulation was not observed until 733 K, higher than either of the exothermic events observed in the present study at 566 K and 602 K (see Table 2). The bulk of the material did not react until above 800 K. In the case of the alloy, eutectic melting was observed, but no exothermic reaction was associated with it.

In the same study, burn rates of test flares were measured, and it was found that pyrotechnic formulations using Al-Mg (cast) alloys combust more slowly than formulations only using Mg as fuel [87]. This observation had also been explained by the earlier melt formation in the alloy, and the tendency of the partially molten particles to agglomerate. While rigorous combustion experiments with the composite powders of the present study remain to be conducted, it can be concluded that the melting of the mechanically alloyed powder is beneficial in enabling ignition, and that agglomeration at heating rates of $10^3 - 10^4$ K/s does not occur, at least not to the extent to impede the reaction.

Based on the rapid increase in the photodiode signal upon ignition for the composites with Mg and mechanically alloyed $Al_{0.5}Mg_{0.5}$ powders, it can be suggested that the ignition is caused by a vapor phase reaction between the volatilized Mg and products of decomposition of $NaNO_3$. Alternatively, for the composite with Al powder, the ignition can also be caused by heterogeneous reaction on surface of aluminum particles, with its rate limited by diffusion of reagents through the alumina layer. Results in Table 3, show that the activation energy of the composite of Mg is lower than that of Al and $Al_{0.5}Mg_{0.5}$ powders.

It is worth noting that ignition temperatures of the nitrate-based nanocomposites determined in the present study are generally higher than previously determined ignition temperatures of similar ARM nanocomposites that were based on metal-oxide/aluminum thermites [21, 22]. This may, however reflect differences in the nano-structure of the respective composites rather than chemistry-based differences in the reaction mechanisms. The nitrates investigated here are mechanically softer and at the same time more easily reduced than the previously studied oxides (Fe_2O_3, MoO_3), leading to generally coarser composite particles compared to oxides.

7.4.4 Flame Emission

The observed lines in the emission spectra can be compared to atomic emission lines as published in literature references [86, 98]. All spectra are dominated by the Na D emission line at ~589 nm. Further observed lines have been attributed to other sodium transitions, or to Na-N_2 interactions. A peak at 500.7 nm was identified in Ref. [86] as due to a MgO molecular transition. Here, it is also observed in the nominally Mg-free Al-$NaNO_3$ composite. A potassium emission doublet is observed near 767 nm, likely due to contamination introduced by sample handling. Similarly, the peak at 670.8 nm may be due to Li contamination. Further, a broad peak is observed near 800 nm, but has not been identified. There is little apparent difference in the emission spectra of the three samples. The peak near 800 nm appears to increase in intensity as the amount of Al in the sample increases. For the Mg-$NaNO_3$ composite, two additional weak peaks are observed at 373 and 384 nm, respectively.

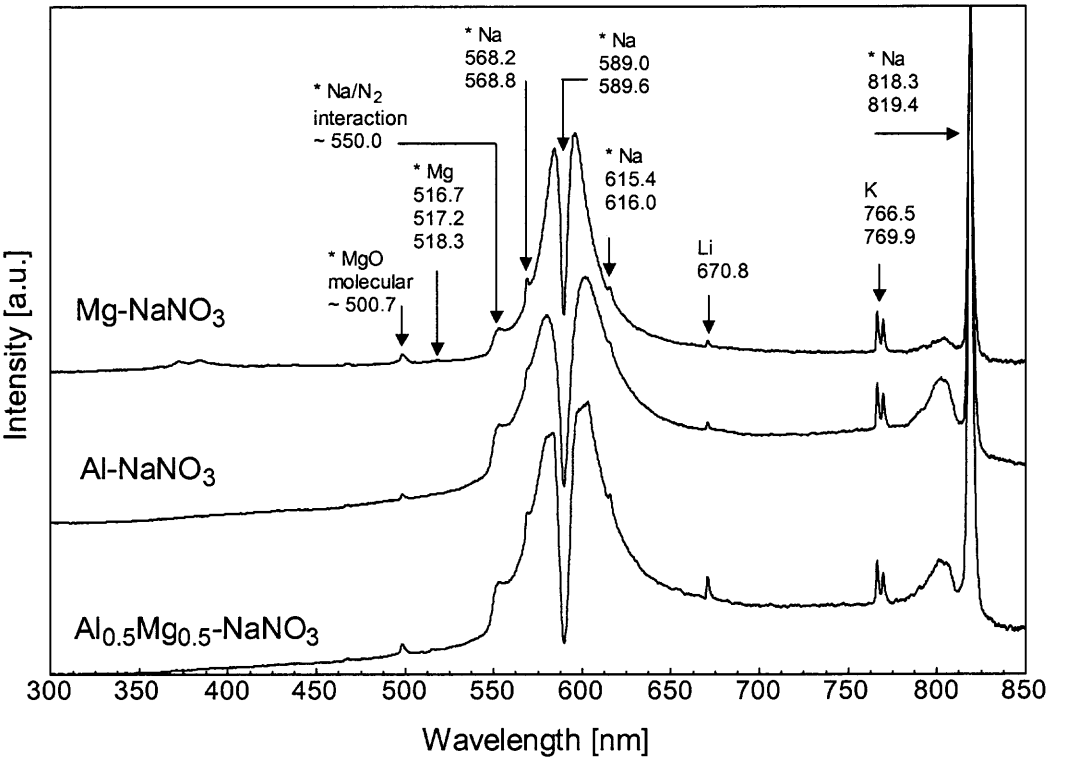

Figure 7.9 Flame emission spectra for the prepared composite materials. Emission lines marked by (*) correspond to lines reported in Ref. [86]. Other lines have been identified from Ref. [98]

7.5 Conclusions

Highly reactive composites have been synthesized from starting blends of sodium nitrate as oxidizer and Al, Mg, and Al-Mg mechanical alloys as fuels respectively, using arrested reactive milling. The materials have been characterized by XRD and SEM. Reaction characteristics were determined by thermal analysis (DTA, TG), and ignition characteristics have been determined by a coated-filament technique.

The scale of the composite powder varies from 100 nm to several μm, and further changes to the milling process may be required to refine the scale of mixing. Thermal analysis shows that the decomposition of $NaNO_3$ in these composites occurs earlier than pure $NaNO_3$ due to the presence of metals.

Comparison of the activation energies obtained from DTA and ignition experiments show that an ignition mechanism can be identified for Mg and Al based composites. Differences were observed for the $Al_{0.5}Mg_{0.5}$-$NaNO_3$ composite, indicating a different reaction mechanism at low and high heating rates, respectively. While at low heating rates the strong exothermic reaction is triggered by melting processes in the alloy, heterogeneous oxidation drives ignition for all composites at high heating rates. For thermal analysis experiments at low heating rates to be useful for extrapolation to high heating rates, the consistency of the reaction mechanism must therefore be confirmed.

Emission spectra in the visible and near UV range have been recorded for the combustion of the composites. Comparison to previously published results for coarse pyrotechnic blends shows that the spectra of the milled composites have largely the same features.

The lowest ignition temperature was observed for the $Al_{0.5}Mg_{0.5}$-$NaNO_3$ composite; together with the high apparent decomposition threshold at low heating rates, this suggests that this material is the most promising for practical applications, where handling and storage are concerns.

CHAPTER 8

CONCLUSIONS

Optimized milling conditions were determined for the synthesis of reactive Al-MoO_3 and Al-CuO nanocomposite powders by ARM. . Milling media with densities in the range of 5 to 8 g/cm^3 result in the highest structural refinement accompanied by the lowest degree of partial reaction. Powders produced with such milling media are most reactive as indicated by the lowest amounts of unoxidized aluminum remaining upon their slow heating to 935 K. The highest reactivity of these powders is also supported by the observed strongest exothermic feature in the DSC traces. Filament ignition tests showed that the same sample powders have the lowest ignition temperatures as compared to other powders with the same bulk compositions.

Highly reactive composites have also been synthesized from starting blends of sodium nitrate as oxidizer and Al, Mg, and Al-Mg mechanical alloys as fuels respectively, using arrested reactive milling. The materials have been characterized by XRD and SEM. Reaction characteristics were determined by thermal analysis (DTA, TG), and ignition characteristics have been determined by a coated-filament technique.

The scale of the composite powder varies from 100 nm to several μm, and further changes to the milling process may be required to refine the scale of mixing. Thermal analysis shows that the decomposition of $NaNO_3$ in these composites occurs earlier than pure $NaNO_3$ due to the presence of metals.

Comparison of the activation energies obtained from DTA and ignition experiments show that an ignition mechanism can be identified for Mg and Al based composites. Differences were observed for the $Al_{0.5}Mg_{0.5}$-$NaNO_3$ composite, indicating a

different reaction mechanism at low and high heating rates, respectively. While at low heating rates the strong exothermic reaction is triggered by melting processes in the alloy, heterogeneous oxidation drives ignition for all composites at high heating rates. For thermal analysis experiments at low heating rates to be useful for extrapolation to high heating rates, the consistency of the reaction mechanism must therefore be confirmed.

Emission spectra in the visible and near UV range have been recorded for the combustion of the composites. Comparison to previously published results for coarse pyrotechnic blends shows that the spectra of the milled composites have largely the same features.

The lowest ignition temperature was observed for the $Al_{0.5}Mg_{0.5}$-$NaNO_3$ composite; together with the high apparent decomposition threshold at low heating rates, this suggests that this material is the most promising for practical applications, where handling and storage are concerns.

Reactions in stoichiometric $2Al+MoO_3$ nanocomposite thermite powders have been investigated using thermal analysis and heated filament ignition experiments. A preliminary reaction model was fit to the experimental data. The reaction model is the superposition of four reaction steps assumed to be independent. The comparison of the activation energies determined for the reaction steps observed in this study with activation energies reported earlier for elementary reactions in the Al-MoO_3 system suggests that the first, low-activation energy reaction is associated with decomposition of MoO_3 while following reaction steps are controlled by the diffusion through growing layers of Al_2O_3. Preliminary comparison with ignition experiments suggest that a

relatively small heat release at the onset of the exothermic reaction causes ignition at high heating rates.

The highly exothermic heterogeneous reaction between Al and CuO was found to start at relatively low temperatures (~ 400 K) and can also be described by four parallel reaction steps. Earlier measurements did not resolve the low-temperature exothermic events and focused on the strongest, fourth reaction step. However, ignition of the nanocomposite Al-CuO materials was shown to be driven primarily by the lower-temperature oxidation processes.

Specific mechanisms and kinetic parameters were determined to describe the individual reaction steps for the prepared nanocomposite powders. These mechanisms include the frequency factors specific for the powders used in this study and activation energies that should remain valid for any Al-CuO composite materials. The identified reaction steps were tentatively assigned to specific processes of CuO decomposition followed by diffusion of reacting species through amorphous and then crystalline Al_2O_3 polymorphs. It was shown that ignition of Al-CuO nanocomposite powders can be described reasonably well using the proposed kinetics of Al-CuO heterogeneous reactions. Future work will focus on development of a complete, quantitative ignition model.

Fuel rich Al-MoO_3 nanocomposites with varying compositions have been synthesized. Uniform mixing of MoO_3 nano-domains in Al matrix is achieved for all samples. Particle size of the nanocomposite powders increases with increase in aluminum concentration. Thermal analysis showed that exothermic processes start when the nanocomposite powders are heated to only about 350 K. Multiple and overlapping

exothermic processes are observed and further work is needed to understand the reaction mechanisms in these materials. At the heating rates varied in the range of 3000 – 30000 K/s, all nanocomposite powders ignite at temperatures well below the Al melting point. Ignition temperatures of samples containing 4, 8, and 12 moles of Al per mole of MoO_3 are similar and lower than those of the sample containing 16 moles of Al. It is noted that for the former set of samples, the ignition mechanism changes as the heating rate increases. Constant volume explosion experiments indicate that the flames produced by nanocomposite thermite powders in air propagate much faster than those produced by pure Al powder. The maximum rate of pressure rise indicative of the highest burn rate was measured for the $8Al+MoO_3$ nanocomposite powder. Maximum reaction pressure indicative of the overall combustion energy is highest for pure Al, closely followed by that for $8Al+MoO_3$ and followed by those for the $12Al+MoO_3$ and $4Al+MoO_3$ nanocomposite powders. The reaction energy normalized per unit mass of aluminum is the highest for nanocomposite materials with bulk compositions $4Al+MoO_3$ and $8Al+MoO_3$ and lowest for pure Al and for the $16Al+MoO_3$ nanocomposite sample. This reduced efficiency of combustion inferred from the measured pressure traces correlates with the analyzed combustion products, containing respectively greater amounts of unreacted aluminum. It is suggested that a reduced efficiency of combustion for very aluminum-rich nanocomposite powders is explained by relatively coarse particle sizes obtained for these materials.

A more detailed analysis of exothermic reactions in Al-MoO_3 system shows that kinetics of such reactions cannot be meaningfully determined by isoconversion processing. The data processing shows that activation energy cannot be meaningfully

determined as a function of reaction progress, as would be required for any type of model-free processing. In this case, which is expected to represent a rather common situation, more measurements at different heating rates are needed to identify trends, and a detailed model development is necessary for meaningful description of the reaction kinetics.

REFERENCES

1. Dr Goldschmidt, Hans. (Germany). (1905), FR 361197 19051230.

2. Wang, L.L., Munir Z.A. & Maximov,Y.M. (1993). Thermite reactions: their utilization in the synthesis and processing of materials. J. Mater. Sci., 28, 3693-3708.

3. Chernenko, E.V., Afanas'eva, L.F., Lebedeva, V.A. & Rozenband, V.I. (Nov-Dec 1988). Inflammability of mixtures of metal oxides with aluminum. translated from Fizika Goreniya I Vzryva, 24(6), 3-11.

4. Son, S.F., Asay, B.W., Busse, J.R., Jorgensen, B.S., Bockmon, B., & Pantoya, M. (2001) Proc. Internat. Pyrotech. Soc., The Twenty-Eighth International Pyrotechnics Seminar, Adelaide, Austraila, November 4-9, 2001.

5. Son, S.F. (2004). Performance and characterization of nanoenergetic materials at Los Alamos. Mat. Res. Soc. Symp. Proc., 800, AA5.2.1- AA5.2.12.

6. Moore, D. S., Son, S. F., Asay, B.W. (2004). Time-resolved spectral emission of deflagrating nano-Al and nano-MoO_3 metastable interstitial composites. Propellants, Explos., Pyrotech. 29(2), 106-111.

7. Granier, J.J. &. Pantoya, M., L. (2004). Laser ignition of nanocomposite thermites. Combust Flame, 138(4), 373-383.

8. Wilson, D. E. & Kim, K. A simplified model for the combustion of Al/MoO3 nanocomposite thermites, 39th AIAA/ASME/SAE/ASEE Joint Propulsion Conference. Huntsville, AL, USA July 20-23, 2003 AIAA-2003-4536, American Institue of Aeronautics and Astronautics, Hunstville, AL, 2003.

9. Plantier, K. B., Pantoya, M.L. & Gash, A., E. (2005). Combustion wave speeds of nanocomposite Al/ Fe_2O_3: the effects of Fe_2O_3 particle synthesis technique Combust Flame, 140, 299-309.

10. Gash, A.E., Tillotson,T. M., Satcher, J.H., Hrubesh Jr L.W. & Simpson.R.L. (2001). New Sol-gel synthetic route to transition and main-group metal oxide aerogels using inorganic salt precursors. J. Non-Cryst Solids 285, 22-28.

11. Tillotson,T. M., Gash, A.E., Simpson,R.L., Hrubesh Jr L.W., Satcher, J.H. & Poco, J.F. (2001) Nanostructured energetic materials using Sol-gel methodologies. J. Non-Cryst Solids 285, 338-345.

12. Gash, A.E., Satcher Jr., J.H., Simpson, R.L. &Clapsaddle, B.J. (2003). Nanostructured energetic materials with Sol-gel methods. Mater. Res. Soc. Symp. Proc. 800, 55-66.

13. Prentice,D., Pantoya, M.L. & Clapsaddle.B.J. (2005). Effect of nanocomposite synthesis on the combustion performance of a ternary thermite. J. Phys Chem B, 109(43), 20180-20185.

14. Subramaniam, S., Hasan, S., Bhattacharya, S., Gao, Y., Apperson S., Hossain, M., Shende R.V., Gangopadhyay, S., Redner, P., Kapoor, D. & Nicolich, S. (2006). Self-assembled nanoenergetic composite. Mater. Res. Soc. Symp. Proc. 896, H01-05.1-05.6.

15. Blobaum, K.J., Reiss, M. E., Plitzko, Lawrence, J. M. & Weihs, T. P. (2003). Deposition and characterization of a self-propagating CuOx/Al thermite reaction in a multilayer foil geometry. J. Appl. Phys. 94(5), 2915-2922.

16. Blobaum, K.J., Wagner, A. J., Plitzko,J. M., Van Heerden, D., Fairbrother,D. H. & Weihs, T. P. (2003). Investigating the reaction path and growth kinetics in CuOx/Al multilayer foils. J. Appl. Phys. 94(5), 2923-2928.

17. Wang, J., Besnoin, E., Duckham, A., Spey, S. J., Reiss, M. E., Knio, O. M. & Weihs, T. P. (2004). Joining of stainless-steel specimens with nanostructured Al-Ni foils J. Appl. Phys. 95(1), 248-256.

18. Schoenitz, M., Ward, T. & Dreizin, E.L. (2004). Fully Dense Nano-Composite Energetic Powders Prepared By Arrested Reactive Milling. Mater. Res. Soc. Symp. Proc. 800, AA2.6.1-AA2.6.6.

19. Dreizin, E.L. & Schoenitz, M., "Nano-composite energetic powders prepared by Arrested Reactive Milling," Application for Letter Patent in the U.S. Patent and Trademark Office on November 12, 2004 , No. 10/988,183.

20. Schoenitz, M., Ward, T. & Dreizin, E.L. (2005). Fully Dense Nano-Composite Energetic Powders Prepared By Arrested Reactive Milling. Proc Combust Inst, 30 2071-2078.

21. Umbrajkar, S.M., Zhu, X., Schoenitz, M. & Dreizin, E.L. (2005) Effect of compositional and structural refinement on the ignition and combustion of reactive nanocomposite powders. Fourth Joint Meeting of the U.S. Sections of the Combustion Institute. Philadelphia, PA 23-25 March 2005, Combustion Institute, Pittsburg, PA, D37/1- D37/6 2005.

22. Umbrajkar, S.M., Schoenitz, M. & Dreizin, E.L. (2006). Control of structural refinement and composition in Al-MoO3 nanocomposites prepared by arrested reactive milling. Propellants. Explos. Pyrotech, 13 (5), 382-389.

23. Clarkson, J., Smith,W.E., Batchelder, D. N., Alastair Smith, D.A. & Coats, A.M. (2003). A theoretical study of the structure and vibrations of 2,4,6-trinitotolune. J. Molecular Structure, 648, 203-214.

24. Shoshin, Y.L., Trunov, M.A., Zhu, X., Schoenitz, M. & Dreizin, E.L. (2006). Ignition of aluminum-rich Al–Ti mechanical alloys in air. Combust. Flame, 144 (4), 688-697.

25. Schoenitz, M. & Dreizin, E.L. (2003). Structure and properties of Al–Mg mechanical alloys. J Mater. Res. 18(8), 1827-1836.

26. Umbrajkar, S.M., Jones, S.R., Schoenitz, M. & Dreizin, E.L (2005). Effect of temperature on the synthesis and properties of aluminum-magnesium mechanical alloys. J. Alloys Compds 40(1-2), 70-77.

27. Trunov, M.A., Schoenitz, M. & Dreizin, E.L. Ignition of Al-Mg Mechanical Alloys, in: L. DeLuca, L. Galfetti, R.A. Pesce-Rodriguez (Eds) Novel Energetic Materials and Application, Edited Book of Proceedings of the Ninth International Workshop on Combustion and Propulsion Arzago d'Adda, BG, Italy 2004, 9.1 - 9.13.

28. Schoenitz, M., Dreizin, E.L. & Shtessel, E. (2003). Constant volume explosions of metallic mechanical alloys and powder blends. J. Propul. Power, 19 (3), 405-412.

29. Trunov, M.A., Hoffmann, V.K., Schoenitz, M. & Dreizin, E.L (2006) Combustion of boron-titanium nanocomposite powders in different environments. Proccedings of 42nd AIAA/ASME/SAE/ASEE Joint Propulsion Conference and Exhibit, Sacramento CA, 6-12 July 2006.

30. Prakash. A., McCormick. A. & Zachariah. M (2005). Synthesis and reactivity of a super-reactive metastable intermolecular composite formulation of Al/$KMnO_4$ Adv Mater., 17 (7), 900-903.

31. Tepper F., Ivanov G., Lerner M. & Davidovich V. (1998) Energetic formulations from nanosize metal powders. Proc. Int. Pyrotech. Semin, 24, 519-530.

32. Cliff M., Tepper F., Lisetsky V. (2001). Ageing Characteristics of Alexr Nanosize Aluminum. 37th AIAA/ASME/SAE/ASEE Joint Propulsion Conference and Exhibit, Salt Lake City, UT, July 8-11, 2001. pp 3287.

33. Sarathi, R., Sindhu, T. K. & Chakravarthy, S. R. (2007). Generation of nano aluminum powder through wire explosion process and its characterization. Materials Characterization 58, 148-155.

34. Miziolek A.W. (2002). Nanoenergetics: An emerging technology area of national importance. *The AMPTIAC Newsletter,* 6(1), 43-48.

35. Eliezer, S., Eliaz, N., Grossman, E., Fisher, D., Gouzman, I., Henis,Z., Pecker, S., Horovitz, Y., Fraenkel, M., Maman, S., & Lereah,Y. (2004). Synthesis of nanoparticles with femtosecond laser pulses. Phys Rev B, 69, 144119, 1-6.

36. Kuo, K.K., Risha, G.A., Evans B.J., & Boyer, E. (2004). Potential Usage of Energetic Nano-sized Powders for Combustion and Rocket Propulsion, Mat Res. Soc. Symp. Proc. Vol. 800, AA1.1.1-1.1.11.

37. Takacs, L. (2002). Self sustaining reactions induced by ball milling. Prog. Mater. Sci., 47, 355-414.

38. Balaz, P., Takacs, L., Boldizarova, E. & Godocokova, E. (2003). Mechanochemical transformations and reactivity in copper sulphides. J. Phys. Chem. Solids., 64(8), 1413-1417.

39. Ward, T.S., Chen, W., Schoenitz, M., Dave, R.N. & Dreizin, E.L. (2005). A study of mechanical alloying processes using reactive milling and discrete element modeling. Acta Mater, 53, 2909-2918.

40. Ramaswamy, A.L. & Kaste, P. (2005). A Nanovision of the Physicochemical Phenomena Occurring in Nanoparticles of Aluminum. J Energetic Materials. 23(1), 1-25.

41. Sanchez-Lopez, J.C., Gozale-Elipe, A.R. & Fernandez, A. (1998). Passivation of Nanocrystalline Al Prepared by Gas-Phase Condensation Method: An X-ray Photoelectron Spectroscopy Study. J. Mater Res, 13 (3), 703-710.

42. Ward, T.S., Trunov, M.A., Schoenitz, M. & Dreizin, E.L. (2005). Experimental methodology and heat transfer model for identification of ignition kinetics of powdered fuels. Fourth Joint Meeting of the U.S. Sections of the Combustion Institute. Philadelphia March 23-25 2005.

43. Table of emissivity of various surfaces by Micron Instrument Company, Inc., www.transmetra.ch/pdf/publikationen/emissivity.pdf, Retrieved on April 1st 2006.

44. Sitepu, H., O'Connor B.H., & Li, D. (2005) Comparative evaluation of the march generalized spherical harmonic preferred orientation models using X-ray diffraction data for molybdite and calcite powders. J. Appl. Crystallogr. 38, 158-167.

45. Larson, A.C. & Von Dreele R.B. (2000). General Structure Analysis System (GSAS). Los Alamos National Laboratory Report LAUR 86-748.

46. Trunov, M.A., Umbrajkar, S.M., Schoenitz, M., Mang, J.T. & Dreizin (2006). Oxidation and melting of aluminum nanopowders. J Phys Chem B, 110(26) 13094-13099.

47. Afeefy, H.Y., Liebman,J.F. & Stein, S.E. "Neutral Thermochemical Data" in NIST Chemistry WebBook, NIST Standard Reference Database Number 69, Eds. P.J. Linstrom and W.G. Mallard, June 2005, National Institute of Standards and Technology, Gaithersburg MD, 20899 (http://webbook.nist.gov).

48. Roduit, B., Borgeat, C., Berger, B., Folly,P., Aebischer, J-N., Andres, H., & U. Schaedeli. (2005). Thermal risk and safety margin for energetic materials: Assessment of scale-up capabilities from milli-(dsc) to kilograms (cook-off). Proceedings of the 36th International Annual Conference of the ICT. 24/1-24/11.

49. Ward, T.S., Trunov, M.A., Schoenitz, M. & Dreizin, E.L. (2006). Experimental methodology and heat transfer model for identification of ignition kinetics of powdered fuels. International Journal of Heat and Mass Transfer, 49, 4943-4954.

50. Sun, J., Pantoya, M.L. & Simon, S.L. (2006). Dependence of Size and Size Distribution on Reactivity of Aluminum Nanoparticles in Reactions with Oxygen and MoO_3. Thermochim Acta 444(2), 117-127.

51. Kissinger, H.E. (1957). Reaction kinetics in differential thermal analysis, Anal Chem 29, 1702-1706.

52. Opfermann, J. (2000). Kinetic analysis using multivariate non-linear regression. I. Basic concepts. J Therm Anal Calorim, 60(2), 641-658.

53. Opfermann, J. NETZSCH Thermokinetics 2, Version 2005.04 NETZSCH Gerätebau GmbH.

54. Maciejewski, M. (2000). Computational aspects of kinetic analysis. Part B: The ICTAC Kinetics Project — the decomposition kinetics of calcium carbonate revisited, or some tips on survival in the kinetic minefield. Thermochim Acta, 355, 145-154.

55. Vyazovkin, S. (2001). Modification of the integral isoconversional method to account for variation in the activation energy. J Comput Chem, 22(2), 178-183.

56. Ressler, T., Jentoft,R. E., Wienold, J. M., Günter, M. & Timpe, O. (2000). In Situ XAS and XRD Studies on the Formation of Mo Suboxides during Reduction of MoO_3, J Phys. Chem. B 104, 6360-6370.

57. Trunov, M.A., Schoenitz, M., Zhu, X. & Dreizin, E.L. (2005). Effect of Polymorphic Phase Transformations in Al_2O_3 Film on Oxidation Kinetics of Aluminum Powders. Combust Flame 140(4), 310-318.

58. Mitin, B.S., & Samoteikin,V.V.(1971). Oxidation of molten aluminum. Zhurnal Fizicheskoi Khimii (J. Phys. Chem.) 45(3), 730.

59. Allison Butts, Copper: The Science and Technology of the Metal, its Alloys and Compounds, Hafner Publishing Company, INC. 1970, 460-462.

60. Ozawa, T. (1965). A new method of analyzing thermogravimetric data. Bull. Chem. Soc. Jpn. 38, 1881-1886.

61. Flynn, J.H. & Wall, L.A. (1966). General Treatment of the Thermogravimetry of Polymers. J. Res. Natl. Bur. Stand. Sect. A 70, 487-523.

62. Kim, J.Y., Rodriguez, J.A., Hanson, J.C., Frankel,A.I. & Lee, P.L. (2003). Reduction of CuO and Cu_2O with H_2: H Embedding and Kinetic Effects in the Formation of Suboxides. J. Am. Chem. Soc. 125, 10684-10692.

63. Li, J., Wang, S.Q., Mayer J.W. & Tu, K.N. (1989). Oxygen diffusion induced phase boundary migration in copper oxide thin films. Phys Rev B, 39(16), 12367-12372.

64. Levin, I. & Brandon, D. (1998). Metastable alumina polymorphs: crystal structures and transition sequences. J. Am. Ceram. Soc. 81, 1995-2012.

65. Eapen B. Z., Hoffmann V. K., Schoenitz M., & Dreizin E. L. (2004). Combustion Of Aerosolized Spherical Aluminum Powders And Flakes In Air. Combust Sci and Techol, 176 (7), 1055-1069.

66. Hertzberg, M., Zlochower, I. A., & Cashdollar, K. L., (1992). Metal Dust Combustion: Explosion Limits, Pressures, and Temperatures, Symposium (International) on Combustion, pp. 1827-1835.

67. Cashdollar, K. L., & Chatrathi, K. (1993). Minimum explosible dust concentrations measured in 20-L and 1-M3 chambers. Combust Sci and Techol, 87,1-6,157-171.

68. Schuster J.C. & Ipser H., (1991). The Al-Al_8MoO_3 Section of the Binary System Aluminum-Molybdenum. Metall Trans A, Vol 22 A, 1729-1736.

69. Umbrajkar, S.M., Schoenitz, M. & Dreizin, E.L. (2007). Solid State Reduction-Oxidation Reactions: An Example When the Isoconversion Approach Fails, Submmitted to Thermochimica Acta

70. NASA CEA code, http://www.grc.nasa.gov/WWW/CEAWeb, Retrieved June 1st 2006.

71. Glassman I., Combustion, 3rd ed., Academic Press, San Diego, 1996.

72. Starink, M.J. (2003). The determination of activation energy from linear heating rate experiments: a comparison of the accuracy of isoconversion methods. Thermochim. Acta. 404(1), 163-176.

73. Opfermann, J. NETZSCH Thermokinetics 2, Version 2005.04 NETZSCH Gerätebau GmbH

74. Roduit, B. AKTS, Advanced Kinetics and Technology Solutions, Thermokinetics Software

75. Vyazovkin, S. (1997). Advanced isoconversional method. J. Therm Anal, 49(3), 1493-1499.

76. Starink, M.J. (1997). On the applicability of isoconversional methods for obtaining activation energy of reactions within a temperature-dependent equilibrium state. J. Mater Sci, 32(24), 6505-6512.

77. Li, C-R. & Tang, T.B., (1999). Isoconversion method for kinetic analysis of solid-state reactions from dynamic thermoanalytical data. J. Mater Sci, 34, 3467-3470.

78. Gawley, A.K., (2003). What is meant by the term 'variable activation energy' when applied in the kinetic analyses of solid state decompositions (crystolysis reactions)? Thermochim. Acta 397, 249-268.

79. Umbrajkar, S.M., Schoenitz, M. & Dreizin, E.L. (2007). Kinetic Analysis of thermite reactions in Al-MoO_3 nanocomposites, J. Propul. Power accepted in press.

80. Hunt, E., & Pantoya, M.L. (2005). Ignition dynamics and activation energies of metallic thermites: From nano to micron scale particulate composites. J App. Phy. 98, 034909-1 - 9.

81. Blobaum, K.J., Van Heerden,D., Gavens,A.J., & Weihs,T.P., (2003). Al/Ni formation reactions: characterization of the metastable Al_9Ni_2 phase and analysis of its formation. Acta Mater, 51, 3871-3884.

82. Fan,R-H, Lu,H-L, Sun,K-N, Wang, Wan-Xia, & Yi, X-B, (2006). Kinetics of thermite reaction in Al-Fe_2O_3 system, Thermochim Acta 440, 129-131.

83. Griffiths, T.T., Charsley, E.L. & Hider, J.A., (1988). A study of pyrotechnic performance of the magnesium-oxidant-binder system, Proceedings of the 13th International Pyrotechnics Seminar, 393-410.

84. Benoit, M., Perotto, C., Duvacquier, D. & Kozyreff, M., : FR2730965, (1996) "Pyrotechnique gas generators for airbags," Fr. Demande.

85. Shuo, Y., Li, Y. & Youwen, X. (1998). Flame spectra of pyrotechnic mixtures, Beijing Ligong Daxue Xuebao, 18(5), 651-655.

86. Douda, B.E., Blunt, R.M. & Blair, E.J. (1970). Visible radiation from illuminating-flare flames: strong emission features, J. of the Optical Society of America, 60(8),1116-19

87. Singh, H., & Rao,R.B., (1995). Influence of aluminum on combustion of magnesium-sodium nitrate pyrotechnic mixture, 26th International Annual Conference of ICT, 57/1-57/11

88. Jackson, B., Taylor Jr., F.R., Motto,R., & Kaye, S.M. (1975). Substitution of aluminum for magnesium as a fuel in flares, U. S. NTIS, AD Rep (AD-A013360), 44

89. Bash, C.W., & Lane, G.A. (1969). Flare composition containing alkali metal nitrate, magnesium, and a copolymer reaction product binder, U.S. Patent 3432370, Dow Chemical Company, USA

90. Laswell, J.E., & Souder,G., (1982). High-efficiency illuminating compositions, Proceedings of the 8th International Pyrotechnics Seminar, 422-434.

91. Singh H. & Rao, R.B. (1992). Effect of particle size on combustion of magnesium-sodium nitrate propellants, Combust Sci and Technol, 81(4-6), 233-42.

92. Rao, R.B., Rao, P.S. & Singh, H. (1995). Prediction of burn rate of magnesium-sodium nitrate propellant, Combust Sci and Technol, 108(1-3), 133-147.

93. Lide, D. R., (Ed) (1993). CRC Handbook of Physics and Chemistry, 74th ed., CRC Press, Boca Raton, FL.

94. Winter, M., WebElementsTM, http://www.webelements.com/. Retrieved November 1st 2005.

95. Kalekar, B.B., Rajagopalan, K.V., Pillai, C.G.S. Ravindran, P.V., & Mathur, P.K., (2000). Thermal and X-ray diffraction studies on the phase equilibria in the system $UO_2(NO_3)_2 .6H_2O$-$NaNO_3$, J of Nuclear Mtls, 279, 245-252.

96. Freeman, E.S., (1956). The kinetics of the thermal decomposition of sodium nitrate and of the reaction between sodium nitrite and oxygen, J Phys Chem, 60, 1487-1493.

97. Murray, J.L., (1982). The Al-Mg (Aluminum-Magnesium) system. Bull. Alloy Phase Diagrams, 3(1), 60-74.

98. Sansonetti, J.E., Martin, W.C. & Young, S.L. (2005). Handbook of Basic Atomic Spectroscopic Data, version 1.1.2, National Institute of Standards and Technology, Gaithersburg, MD.